Atomic Scale Disorder in Fluorite and Fluorite Related Oxides

A dissertation submitted to the University of London
for the degree of Doctor of Philosophy
and the Diploma of Imperial College

by
Christopher R. Stanek

Department of Materials
Imperial College of Science, Technology and Medicine

August 2003

Abstract

Atomistic simulation techniques have been used to calculate a variety of disorder properties in oxides with the fluorite structure and the pyrochlore structure (which is fluorite related).

Chapter 1 introduces pertinent concepts such as crystallography, point defect equilibria, surface types and transport theory. Chapter 2 discusses the methodology of bulk, surface, perfect and defective lattice calculations.

Chapter 3 and 4 are concerned with UO_2. Chapter 3 presents results of fission product solubility calculations in UO_2. In particular, the solution of Kr, here calculated classically, is compared to similar *ab initio* calculations of other researchers. Chapter 4 builds upon these results by discussing the segregation of fission products to the stable, low index (111), (110) and (100) surfaces of UO_2. It is shown that the segregation behaviour depends on fission product chemistry, charge, size as well as surface.

In Chapters 5 and 6, aspects of the defect behaviour of pyrochlore oxides are investigated. Chapter 5 discusses mechanisms to generate non-stoichiometry in a broad range of pyrochlore compounds. Calculations are presented in the form of a contour map, in order to convey the large amount of information. These results are compared with experimental phase diagrams. Chapter 6 predicts the existence of heretofore unobserved pyrochlore compounds, $Dy_2Hf_2O_7$, $Ho_2Hf_2O_7$ and $Er_2Hf_2O_7$.

This prediction is made by comparing calculated local order-disorder energies with the corresponding order-disorder temperatures obtained from phase diagrams.

The concluding chapter summarizes the results of this thesis and offers ideas and details for potential future work. Projects involving both bulk and surface simulations are proposed.

Appendix A describes the segregation of Y_2O_3 to surfaces of t-ZrO_2.

Acknowledgements

In a classic oversight, I arrived in London without a pillow, blanket, utensils, etc., and immediately learned that I would need to rely on a fairly sturdy support network if I was to make it through this process. During the said process, as important as the science I have learned has been the reiteration of the importance of family and friends. It is therefore inappropriate to continue without thanking a few of these people.

It would also be inappropriate not to start by thanking my advisor, Prof. Robin W. Grimes. Exemplifying the ideal advisor from the student perspective (the only one I can speak on), Robin went and continues to go far beyond the call of duty for all of his students, of which I was fortunate enough to have been one.

The Atomistic Simulation Group at Imperial College was a wonderful place to work. Thanks to Michael Abramowski for taking time (a non-negligible amount) in order to show me the ropes, to Kurt Atkinson for not only keeping us up and running, but for being a good friend, to Mark Levy for filling kjwa's void, to Licia Minervini for not only introducing me to the group, but also serving as an advisor of all sorts, and to Mohsin Pirzada for teaching an American a thing or two about cricket.

Many thanks to the friends I made in London, especially: the entire 14 Bramber Rd. contingent (Ben, Donna, Kimiko, *et al.*), for the use of a comfy (if not rather

dingy) chair, for humouring my preference of Tandoori Garden over North End Tandoori and for providing a place I looked forward coming home to; and Brad Carmady for augmenting my collection of near death stories.

Los Alamos National Laboratory was a worthwhile hiatus from London, and the people there made my visit more so enjoyable. I believe this thesis has greatly benefitted from my stay (most of Chapters 5 and 6 were written on the lifts at Pajarito Mt. or at the Tesuque Village Market). However, it would not have been as fruitful if it weren't for the interaction I was able to have with the Los Alamos scientists. I appreciate their openness and willingness to work with a visiting Ph.D. student.

The University of Colorado at Boulder unknowingly provided invaluable library resources. I am not certain who to thank, but feel it in my karmic interests to do so. Also, thanks are in order to my Physics 112 and 211 students, for helping me to learn physics.

Each member of the Henwood family contributed to the completion of this thesis. Their kindness and generosity is without parallel.

The entirety of my family did not let a lack of geographic proximity interfere. For allowing me to explore, I am indebted to you Mom, Kate, Dan and especially my Dad, to whom I dedicate this thesis.

And finally, my utmost gratitude to CH, for believing in the promise of better times.

Copyright

Contents

List of Tables

List of Figures

Chapter 1

Introduction

"The branch of physics we call 'the physics of the solid state' is, in large measure, the study of defects in crystalline solids and the effects that they have on the properties of these solids. In this it has to be contrasted with the parallel science of crystallography, which studies the arrangements of the atoms themselves."

- N.F. Mott

The Page - Barber Lectures, 1956

The aim of this thesis is to describe work done investigating disorder in fluorite based oxides. There exist many compounds whose crystal structure is either that of fluorite or closely resembles this structure. This introduction begins with a description of the crystal structure of the compounds considered and then continues with a discussion of disorder and disorder processes. Indeed, there are many ways in which the order in crystalline solids can be disturbed, such as imperfections in position, composition and electronic state [1]. Since this thesis will be concerned with modelling the predictions of disorder, the introduction therefore provides a rudimentary discussion of the means by which disorder is introduced into a lattice.

1.1 Fluorite Based Oxides

1.1.1 MeO_2 Oxides

The term "fluorite" originates with the mineral CaF_2, which is generally known by the same name. Oxides which adopt the fluorite structure or structures related to fluorite have great and varied technological importance. Of those compounds considered in this thesis, applications range from nuclear fuel for UO_2 to thermal barrier coatings and solid oxide fuel cell components for pyrochlores. Despite the vast difference in applications, the crystal structures of fluorite and pyrochlore compounds are very similar. This thesis then begins with a description of structure.

Pauling formulated a set of rules governing the stability of ionic crystal structures [2, 3] (also see [4] for a particularly informative discussion of these rules). The first of these states:

> *A coordinated polyhedron of anions is formed about each cation, the cation - anion distance being determined by the radius sum and ligancy of the cation by the radius ratio.*

This is easier to visualize if ions are thought of as spheres, anions surrounding a single cation. The preferential coordination of anions is dependent on the size of the cation with respect the anionic radius. For example, the minimum radius for a cation coordinated by an octahedron is easily calculated to be 0.414 times the radius of the anion, see Figure 1.1. At this distance ratio, the anions just touch and can therefore move no closer. If the cation is any smaller than this, the Coulomb energy becomes defined by the anion-anion distance (assuming the cation remains in the centre). However, by selecting a structure with a lower coordination number, the minimum possible anion-cation distance is smaller and the Coulomb interaction can be greater. Another way of visualizing this destabilization, is that once the

The general formula of the oxide pyrochlore structure can be written as $A_2B_2O_6O'$. There are four crystallographically unique atom positions and the space group is $Fd\bar{3}m$ [10]. A common way of describing the structure is by fixing its origin on the B site, with atoms located at the following positions (using Wyckoff notation): A at $16d$, B at $16c$, O at $48f$ and O' at $8b$ [10]. The only internal positional variable of the pyrochlore structure is the oxygen x parameter, which characterizes the $48f$ oxygen atoms. To better visualize the pyrochlore structure, the convenient, fluorite type description is used [11, 12], see Figure 1.3. The pyrochlore structure can thereby be considered as an ordered, defective fluorite solid solution. In CaF_2, the fluorine anions are located in the tetrahedral sites of a Ca face centered cubic array. In this description of pyrochlore, the A and B cations form the face centered cubic array, but are additionally ordered in the <110> directions such that the A cations are eight coordinate and the B cations are six coordinate with respect to oxygen. This cation ordering means that the tetrahedral anion sites are no longer crystallographically identical. In fact, there are now three distinct tetrahedral sites: the $48f$, which has two A and two B nearest neighbours, the $8a$, which has four B nearest neighbours and the $8b$, which has four A nearest neighbours. In pyrochlore, the $8a$ positions are vacant. Figure 1.3 depicts one eighth of the pyrochlore unit cell, which is analogous to a single fluorite unit cell. Figure 1.4 depicts a full unit cell of a pyrochlore, with the anions removed in order to better view the two cationic sublattices and the ordering along <110> directions.

1.2.1 Intrinsic Disorder

Intrinsic disorder is so termed because it requires only thermal activation, rather than the addition of impurities or solutes. As temperature is raised, contributions to the free energy due to the entropy term (increasing the magnitude of lattice vibrations and configurational terms) increase the number of atoms that are displaced from regular lattice positions. However, the concentration of defects is able to remain finite. This is because an increase in thermal energy also gives rise to an increase in entropy, thus reducing the free energy, which is evident in the following equation:

$$G = G^o + n \cdot \Delta g - T \cdot \Delta S_c \tag{1.1}$$

where ΔS_c is the configurational entropy due to the solution of defects, $n \cdot \Delta g$ is the free energy change necessary to create n interstitials and G^o is the free energy of a perfect crystal. The two most common types of crystalline defects in ionic materials are Frenkel [15] and Schottky defects [16, 17]. (It should be noted that thermodynamic equilibrium is not always reached, and therefore real materials contain a variety of defects due to slow kinetics of removal [18]).

Frenkel disorder results when an atom is displaced from its regular site to an interstitial site, thus forming a defect pair (see Figure 1.5). For a binary metal oxide MeO, the corresponding defect formation reaction is:

$$Me^x_{Me} + V^x_I \leftrightarrows Me^{\cdot\cdot}_I + V''_{Me} \tag{1.2}$$

where Ω_v is the number of ways to arrange vacancies, N is the number of regular sites, and n_v is the number of vacancies. Similarly for interstitials:

$$\Omega_i = \frac{N!}{(N-n_i)! \cdot n_i!} \tag{1.5}$$

These equations can then be inserted into Equation 1.3, leading to:

$$\Delta S_c = k \cdot \ln \left\{ \left[\frac{N!}{(N-n_i)! \cdot n_i!} \right] \cdot \left[\frac{N!}{(N-n_v)! \cdot n_v!} \right] \right\} \tag{1.6}$$

Using the equality $n_i = n_v$ (for ceramics, this is the electroneutrality equation):

$$\Delta S_c = k \cdot \{ \ 2\ln N! - 2\ln \left[(N-n)! \cdot n! \right] \} \tag{1.7}$$

If Stirling's approximation for large numbers [19] is employed:

$$\ln n! \approx n \ln n - n \tag{1.8}$$

then the expression for ΔS_c can be rewritten as:

$$\Delta S_c = 2k \cdot \{ \ N\ln N - (N-n) \cdot \ln (N-n) - n \cdot \ln n \} \tag{1.9}$$

Equation 1.9 can be substituted into the equation for the free energy:

$$G = G^o + n \cdot \Delta g - 2kT \cdot \left\{ \ N\ln \left[\frac{N}{N-n} \right] + n \cdot \ln \cdot \left[\frac{N-n}{n} \right] \right\} \tag{1.10}$$

At thermodynamic equilibrium, the free energy has a minimum with respect to n, i.e. $\left(\frac{\partial G}{\partial n}\right)_{T,P} = 0$. The expression for $\left(\frac{\partial G}{\partial n}\right)_{T,P}$ is obtained by differentiating Equation 1.10. If this is subject to the approximations for large N and small (i.e. dilute) concentration of defects, $N \gg n$, such that $N - n \approx N$, it is then possible to obtain [5]:

$$\frac{n}{N} = \exp\left(-\frac{\Delta g}{2kT}\right) = \exp\left(\frac{\Delta s}{2k}\right) \cdot \exp\left(-\frac{\Delta h}{2kT}\right) \tag{1.11}$$

It should also be noted that Δs is the entropic term which results from lattice strains and vibration frequencies altered by the presence of the defect. It is often the case that this term is assumed to be zero, despite the fact that values between 10^{-4} to 10^{4} have been reported [5]. It is clear then that absolute defect concentrations are difficult to obtain with any degree of accuracy. Much more useful are the *relative* differences in defect concentrations (and indeed most defect related properties) between compounds.

The other type of intrinsic disorder previously mentioned is that of Schottky disorder [16, 17]. Schottky disorder is the simultaneous occurrence of cation and anion vacancies in thermal equilibrium, see Figure 1.5. In this case, vacancy defects must be formed in a number which maintains the electroneutrality of the lattice. For example, MgO forms both one magnesium and one oxygen vacancy (a Schottky pair) while TiO_2 forms a titanium vacancy and *two* oxygen vacancies:

$$Mg_{Mg}^{x} + O_{O}^{x} \leftrightarrows V_{Mg}'' + V_{O}^{\cdot\cdot} + MgO \tag{1.12}$$

and:

$$Ti_{Ti}^{x} + O_{O}^{x} \leftrightarrows V_{Ti}'''' + 2\ V_{O}^{\cdot\cdot} + TiO_2 \tag{1.13}$$

The thermodynamics are analogous to that of Frenkel disorder, see Equation 1.11, and the concentration of defects increases exponentially with temperature (i.e. $e^{-1/T}$).

Another type of intrinsic disorder that may exist is that of ionic interchange known as antisite disorder, where ions swap sites. This may seem unlikely, especially in particularly strong ionic, binary crystals [20], but as will be seen later, in materials with more than one cationic sublattice, swapping of cations is quite common indeed. It is also usual for all of these disorder processes to be present simultaneously, though one type of disorder typically predominates. In general terms, Frenkel disorder is more likely when the anion and cation differ substantially in size and when the lattice

polarization is pronounced, e.g. AgBr [20, 21]. When the anions and cations are of similar size (as is the case for NaCl) Schottky disorder is favoured. Crystallography also plays a critical role. In close packed materials, there is little lattice space to accommodate an interstitial ion. It follows that Frenkel disorder is not favoured in these materials. Conversely, in open structures, Frenkel disorder is more easily accommodated.

1.2.2 Extrinsic Disorder

For the purpose of this thesis, intrinsic disorder is differentiated from extrinsic disorder as follows: intrinsic disorder only encompasses thermally activated defect processes which occur within an otherwise perfect lattice where there is no reaction with the environment. This is certainly a topic for debate, but inevitably it is only a matter of semantics (as elucidated by Chiang *et al.* [5]). Therefore, according to this definition, extrinsic disorder includes defects resulting from oxidation or reduction, i.e. non-stoichiometry. Essentially, extrinsic disorder includes reaction with gaseous species from the environment that are constituents of the lattice in question and reaction with species from the environment that are not native to the lattice. In cases of large formation energies or low concentrations of intrinsic defects, extrinsic behaviour can play the determinant role.

The concept of *stoichiometry* (i.e. the constant and fixed ratio of elemental constituents of a chemical compound) dates back to Dalton's atomic hypothesis [22], and more so the Law of Definite Proportions, which was a product of this hypothesis. This law states that the constituent elements of any compound exist in distinct proportions. This law was the topic for heated debate between Proust, a proponent of the law, and his fellow Frenchman Berthollet, who suggested that the composition of solid compounds is by no means constant. Berthollet lost that debate (in as much

as the theory of Definite Proportions became a law), but was vindicated many years later in a paper by Kurnakov, where it was found that the constituents of various intermetallics varied in composition [23]. Schottky and Wagner went on to suggest that all inorganic solids are inherently non-stoichiometric [16].

The non-stoichiometry of metal oxides can be subdivided into two categories with respect to exact stoichiometry: metal deficient or oxygen deficient. Non-stoichiometry is a direct result of point defects and the extent of non-stoichiometry is measured by the net concentration of these defects [21]. Just as the reactions for Frenkel and Schottky disorder were electronically neutral, the reactions for non-stoichiometry must also be kept neutral through the formation of complimentary point defects. In metal deficient oxides, if metal vacancies are formed, they are complimented by electronic defects on either remaining metal sites (increasing the valence state), on the oxygen site (lowering the charge) or by a delocalized charge. If the metal sublattice remains intact, the non-stoichiometry is facilitated by oxygen interstitial defects compensated by the electronic defects mentioned above. It follows that for the oxygen deficient analogue, metal interstitials or oxygen vacancies will be the predominant structural defects.

A perhaps more clear example of extrinsic disorder, but still technologically significant, is the presence of impurity defects which are non-native to the compound. For example, doping a material (thus generating defects) can have pronounced effects on a variety of properties: doping Si with group V atoms Sb, As, P or group III atoms In, Al or B creates charge carriers for n- and p- type semiconductors respectively [24]. In addition, the solution of $CaCl_2$ lowers the density of KCl with the production of K vacancies [25]. Finally, the cubic fluorite structure of ZrO_2 can be stabilized with a variety of oxides such as Y_2O_3 or CaO. The latter example is particularly important in electrochemical applications due to the generation of anion vacancies.

For example:

$$CaO_{(g)} + (Zr_{Zr})^{x} + (O_O)^{x} \leftrightarrows (Ca_{Zr})'' + (V_O)^{\cdot\cdot} + ZrO_2 \tag{1.14}$$

1.2.3 Fission Produced Defects

The impurity defects considered in this thesis are generated by the fission process (a term borrowed by Otto Frisch [26, 27] after learning from a biologist colleague, William Arnold, of the word for cell division [28]) and not through doping. Although the discovery of nuclear fission is relatively recent, because of its complexity and implications, much research has been done to further the understanding of this phenomenon. By 1936, Fermi and others [29–31] were able to show that slow neutrons were able to disintegrate nuclei. However, it was the strange manner in which uranium disintegrated which made it so exciting. Uranium is naturally radioactive and disintegrates via the emission of alpha particles. The fact that slow neutron irradiation was leading to beta ray emission meant that a different process was taking place. In 1939, Hahn and Strassman [32] found at least three radioactive bodies when bombarding uranium with neutrons, one of which was barium. Initially it had been believed that radium was being produced. This misconception was on account of the limitations of atomic theory at the time. After many thorough chemical experiments it became clear that the substance Hahn and Strassman obtained was barium, and thereby it was deduced that the uranium nucleus, after capturing a neutron is able to split into two nuclei (Niels Bohr stated after this discovery, "Oh, what fools we have been. We should have seen that before!" [28]). Although a detailed account of the fission process mechanism is not justifiable (and can be found elsewhere: see Fission, Chapter 10, by J.A. Wheeler and I.G. Schröder in [33]), a few points are relevant. The following reaction describes a typical example of the fission of U^{235} [34]:

there are some slight differences. However, in both plots, there is a very pronounced double peak for the statistical distribution of fission products. This double peak is strongly dependent on what has induced the fission event. The slower the neutrons, the more pronounced the peaks. Higher energy neutrons give rise to a more symmetrical curve. Another important fact that can be observed in Figure 1.6 is that there are a significant number of decay atoms present, each of which will behave in a different chemical and physical manner.

1.2.4 Association of Point Defects

As previously mentioned, it is possible, and in fact likely that different types of defects will exist. However, a model based upon the assumption that point defects form an ideal solution is too simple. An important behaviour to consider is the interaction between defects, especially those exhibiting Coulombic attraction due to their opposite charges. The interaction between defects is, among other things, a function of their concentration. At low concentrations, ideal solution defect models are useful, but as the concentration of defects increases, activity coefficients must be introduced. The first attempt to correct activity dependent defect interactions was the Debye - Hückel theory [38, 39], which was initially developed for aqueous, electrolytic solutions. The basis of this theory is that all deviations from ideal behaviour can be accounted for by electrostatic interaction between charged species. If one ion is considered, it can be thought of as attracting a cloud of oppositely charged ions, which screen it from all other defects, thereby decreasing the chemical potential. Chemical potential in this case can be expressed as an activity coefficient. The end result of the Debye - Hückel treatment is that the activity coefficient for any defect is less than its concentration. The mean activity coefficient, $f_{\pm}$, is expressed as:

$$f_{\pm} = exp\left\{ -\frac{e_o^2}{8\pi \cdot \epsilon_o \cdot \epsilon \cdot kT} \cdot \frac{b}{1 + b \cdot a} \cdot |z_+ \cdot z_-| \right\} \tag{1.17}$$

where e_o is the charge of an electron, ϵ is the relative dielectric constant (permittivity), ϵ_o is the absolute dielectric constant, k is Boltzmann's constant, a is the smallest distance after which associates will not form and z_+, z_- are the charges of the point defects considered. The distance, $\frac{1}{b}$, is known as the Debye length and can be expressed as:

$$b = \sqrt{\frac{e_o^2}{\epsilon_o \cdot \epsilon \cdot kT} \cdot \sum_i n_i \cdot z_i^2} \tag{1.18}$$

where n_i is the number of defect species per cm^3. From this equation, it is clear that the Debye length (the screening length) increases with a decrease in the defect concentration or an increase in the dielectric constant. Unfortunately, the Debye-Hückel correction is not necessarily realistic physically when applied to defective solids (after all, it was developed for liquids). Firstly, ϵ is a function of temperature and is generally unknown. What's more, the dielectric constant is a bulk value which is meaningless when applied to atomic distances. Thus, the Debye-Hückel theory is only valid at low defect concentrations.

The work described in this thesis is concerned with fluorite compounds which display very high defect concentrations such that close defect association is practically imposed. As such, a Debye-Hückel correction is not appropriate.[1] Rather, it is sufficient to simply consider defect associations explicitly at an atomic level (and therefore *defect clustering*). This relates our results to low temperatures but high defect concentrations; conditions which are generally satisfied by the compounds investigated in this study.

[1] More complex models have been developed to account for defect interactions (e.g. [40,41]), but these are not practical for this study.

not possible to form a surface free of a dipole moment. Chapter 4 is concerned with results for the segregation of fission products to low index surfaces of UO_2 and will discuss the structure of each of these surface types that form in fluorite in detail. As will be shown, each of these Tasker surface types is represented by the three low index surfaces of UO_2.

The stability of a surface is controlled by its *surface energy* which is defined as: [42]

$$\gamma = \frac{(E_{crystal\ with\ surface}) - (E_{bulk})}{(surface\ area)} \tag{1.19}$$

Surface energies are capable of being calculated (the details of which will be discussed in Section 2.3) providing information on surface stability [44] and thus for equilibrium crystal morphology [45–48]. It has been shown that if there exists a dipole perpendicular to the surface, the surface energy is infinite and such surfaces do not occur [49]. Recalling that Type 3 surfaces have such a dipole moment, it follows that they will not form unless the dipole is neutralized by defects. Typically, a number of ions must be removed from the surface and placed on the bottom of the crystal. This generates a dipole across the crystal that is in opposition to the surface dipole.

1.4 Transport

1.4.1 Diffusion Equations

Transport in ceramics, both mass and electrical, is an important and complicated phenomenon. For example, mass transport governs the densification process during sintering while electrical transport is necessary for fuel cells. Diffusion is the transport of matter, in the form of atoms, ions or molecules and is responsible for most

structural changes. The common way of describing diffusion is through Fick's first law [50]:

$$J = -D\left(\frac{dC}{dx}\right) \tag{1.20}$$

where J is the flux of a species in moles per unit area time unit (e.g. mol/(cm$^2\cdot$ sec)), D is the *diffusion coefficient* and dC/dx is a concentration gradient. D is a useful property of materials, since it describes the rate of diffusion of a species, or its *diffusivity* and usually appears in units of cm^2/sec. Fick's first law is analogous to both Ohm's law for electrical conduction and Fourier's law of heat conduction [51] (though it should be pointed out that these are not actually "laws," but rather mathematical descriptions of phenomena). Fick's first law is applicable in steady state situations, when J is independent of time. However, if the concentration, C, varies with time (i.e. non-steady state), then Fick's first law becomes more difficult to use. The increase in concentration with time must equal the negative flux:

$$\frac{\partial C}{\partial t} = -\frac{\partial J}{\partial x} \tag{1.21}$$

and then substituting Fick's first law, to obtain:

$$\frac{\partial C}{\partial t} = -D\frac{\partial^2 C}{\partial x^2} \tag{1.22}$$

which is commonly known as Fick's second law. Solutions to Fick's second law become very complicated, often involving error functions, infinite trigonometric series as well as Bessel functions (common in cylindrical geometries). In depth discussions of Fick's second law and its solutions can be found elsewhere [52, 53].

1.4.2 Atomistic Theory of Diffusion

This account of diffusion has thus far been strictly phenomenological, and has not yet addressed the atomistic theory of diffusion. Diffusion on the microscopic scale

was first documented by Robert Brown after having observed the seemingly random movement of pollen particles immersed in water [54]:

> *These motions were such as to satisfy me, after frequently repeated observation, that they arose neither from currents in the fluid, nor from its gradual evaporation, but belonged to the particle itself.*

Initially, Brown thought this "movement" to be a characteristic of only organic substances, referring to them as "*elementary active particles*," but eventually included inorganic material as well after further experimentation (even having tested powder obtained from a fragment of the Sphinx). Such was the lack of understanding, that Brown cautiously warned:

> *The dust or soot deposited on all bodies in such quantity, especially in London, is entirely composed of these molecules.*

Despite continuous research on so called Brownian motion, it was not until the early 20^{th} century that Smoluchowski [55] and Einstein [56, 57] provided a precise explanation. This problem, commonly referred to as "random-walk," attempts to determine the final position of particles by using jump frequencies and average jump distances. If a block of material is considered as having a concentration gradient along its x axis (see Figure 1.8), an equation can be derived which relates D to the jump frequency and jump distance.

1.4.3 Segregation

The *segregation* of fission products to surfaces of UO_2 is discussed in Chapter 4, where segregation is the movement of a species toward (or away from) a surface, boundary or interface. Theoretical explanations for surface segregation date back to Gibbs [62], and his description of a *dividing surface* between two bulk phases. Despite the fairly long time of qualitative understanding, it is only recently that analytical instruments have been developed to feasibly investigate this phenomenon (e.g. Auger electron spectroscopy [63]). Nevertheless, segregation trends are difficult to extract from experimental data. This can be attributed to the complexity of segregation. Factors such as ionic space charge, the compensation of surface charge beneath the surface, and surface strain effects further complicate the segregation phenomenon. Chapter 4 discusses yet more complications encountered during this work.

Chapter 2

Atomistic Simulation: Bulk and Surface Methods

"It is only after having failed at many attempts that one succeeds in preventing the mutually attractive balls from touching."

- Charles Augustin Coulomb

The Second Electricity and Magnetism Memoir, 1785

As the number of transistors per integrated circuit persistently adheres to the exponential growth pronounced in Moore's Law [64], computers will continue to become more powerful. It is therefore now possible to model systems which were unthinkable ten years ago. For example, atomistic simulations have recently been used in the biological realm to determine complex protein structures [65]. Atomistic forces can be determined in two ways: classically (based on Newtonian mechanics) and quantum mechanically. Although this thesis predominantly deals with classical simulations, one should not disregard quantum mechanical studies which are inherently more accurate. The undesirability of quantum mechanical calculations arises when confronted with limited computing resources. Per ion modelled, classical cal-

culations are far more efficient and less computationally taxing, allowing for a larger number of atoms to be considered. Eventually, when processing power has substantially increased, quantum mechanical simulations will be much more amenable to larger systems.

The first classical atomistic simulations carried out, were those of Boswara and Lidiard who attempted to determine Schottky defect formation energies in NaCl structured alkali halides and cesium halides [66, 67]. In fact, most of the early calculations considered highly ionic and rather simple compounds. Transition metal oxides were investigated in the 1970's, using a similar methodology [68, 69]. The Harwell Laboratory was a major driving force for the continuation and progression of atomistic simulation, focusing on the calculation of basic UO_2 defect energies [70,71] as well as fission product behaviour [36, 72]. Many of the techniques pioneered in those studies are utilized in this work.

Initial atomistic simulations were limited to the calculation of bulk defect properties. Not until Tasker's code MIDAS [73], were surface properties able to be calculated. The MIDAS code, though allowing for many more types of simulation, was limited to charge neutral surfaces. The code CHAOS [74] was developed to calculate defective surface properties. As with the initial bulk calculations, initial surface calculations considered simple ionic systems, which were predominantly cubic, e.g. MgO, CaO and NiO [75, 76]. MARVIN (Minimization And Relaxation of Vacancies and Interstitials for Neutral Surfaces Program) is a more recent surface code [77], based on the fundamentals used by MIDAS and CHAOS, but updated for new potential models (to be discussed later in this chapter) and low symmetry salts such as carbonates, sulfates and phosphates. Also updated is the ability to simply introduce ions and molecules onto the surface, which was previously difficult with MIDAS.

2.1 Perfect Lattice

Ionic crystal theory can be traced back to the work of Madelung [78] and Born [79, 80]. All of the compounds considered in this thesis form ionic crystals, which is to say that they have a regular arrangement of positively charged metal atoms and negatively charged (in this case) oxygen atoms. The lattice of these materials can be described in the classical manner, which assumes all ions are formally charged and spherical and interactions between these ions obey simple central force laws. The lattice energy is therefore:

$$\mathrm{E_{lattice}} = \frac{1}{8\pi\epsilon_\circ}\left(\sum_i \sum_{j\neq i} \frac{q_i q_j}{r_{ij}}\right) + \frac{1}{2}\Phi_{\mathrm{s-r}} \tag{2.1}$$

where q_i and q_j are the charges of the ions i and j, r_{ij} is the ionic separation and ϵ_o is the permittivity of free space. The first term of Equation 2.1, the Coulombic energy, is the main interaction between ions and attracts the unlike charged ions, accounting for the major portion of the cohesive energy of ionic materials. The second term in Equation 2.1, Φ_{s-r} is the total short range interaction energy. Short range forces serve to keep the unlike charged ions from collapsing upon one another and like charged ions from becoming unbound.

The calculations carried out in this work are referred to as "static," which is to say that they do not account for lattice vibration explicitly or configurational entropy at all. Rather, the lattice energy as it appears in Equation 2.1, is calculated with the Coulombic interactions summed using a mathematical construction and the short range interactions initially summed but then neglected after a few lattice spacings. The minimum energy atomic configuration is achieved using energy minimization techniques, discussed in Section 2.1.4. This accounts for a perfect lattice. The calculation of point defect and surface energies involve further considerations,

discussed in Sections 2.2 and 2.3 respectively.

2.1.1 Ewald Summation

Despite the apparent simplicity of the Coulomb term in the equation for lattice energy, it is actually very difficult to compute, as it is a long range force. The spatial interaction of long range forces typically falls off no faster than r^{-d}, where d is the dimensionality of the system [81]. Long range interactions give rise to rather serious problems in regard to atomistic simulations, as they can span half the distance of the simulation cell. Therefore, a method to handle this problem must be introduced. The simulations used in this work make use of the Ewald summation [82].

Ewald devised a technique which sums the interactions between an ion and its periodic images. The original derivation is rather mathematically intensive. Therefore, the following treatment is a simplification which focuses on the significant aspects of the method, after an unpublished paper of Shockley and Ewald (which can be found in [83]). The lattice assumed in this description consists of spherical, non-overlapping ions, with charge of the same magnitude whether positive or negative. The total potential at a specific lattice point can be partitioned into two sub-potentials as:

$$\Psi = \Psi_1 + \Psi_2 \tag{2.2}$$

where Ψ_1 is in reciprocal space and Ψ_2 is in real space. The potential Ψ_1 is of a lattice of point charges, with a Gaussian charge distribution of equal magnitude but opposite sign superimposed on the lattice. The potential Ψ_2 is that of a lattice with a Gaussian distribution of charge fixed at each lattice point, with the same sign as the lattice. When this potential is added to Ψ_1, the overall potential is reduced to the original set of point charges. The point of splitting the overall potential Ψ into

Ψ_a and the charge density associated with it, ρ, can be expressed in terms of a Fourier series:

$$\Psi_a = \sum_k c_k e^{i(\mathbf{k}\cdot\mathbf{r})} \tag{2.5}$$

and

$$\rho = \sum_k \rho_k e^{i(\mathbf{k}\cdot\mathbf{r})} \tag{2.6}$$

where c_k and ρ_k are coefficients and $\mathbf{k}$ is 2π times the reciprocal lattice vectors. The series converges as $\mathbf{k}$ increases and c_k and ρ_k decrease. The charge density can be related to the electrostatic potential by Poisson's equation:

$$\nabla^2 \Psi_a = -4\pi\rho \tag{2.7}$$

This relation can be used to determine an expression for Ψ_a:

$$\Psi_a = q_i \sum_j \left[q_j \frac{4\pi}{V_C} \sum_k \left(\frac{1}{k^2}\ e^{-\frac{k^2}{4\eta}} e^{i(\mathbf{k}\cdot\mathbf{r})} \right) \right] \tag{2.8}$$

where V_C is the unit cell volume. (A complete derivation of Equation 2.8 appears in Equations B.5 - 5.9 in the 1954 edition of Kittel's Introduction to Solid State Physics [83], though not in later editions, e.g. [25]).

When $\mathbf{k} = 0$, the potential Ψ_a tends to infinity. However, as it is assumed that the overall charge of a neutral unit cell is zero, the term $\mathbf{k} = 0$ can be ignored. The other constituent of Ψ_1, is the potential at the reference point due to the central Gaussian distribution:

$$\Psi_b = \int_0^\infty 4\pi r\rho\ dr = \sqrt{\frac{2q_i^2}{\epsilon_o}\left(\frac{\eta}{\pi}\right)} \tag{2.9}$$

Therefore, the difference of Equations 2.8 and 2.9 results in:

$$\Psi_1 = q_i \sum_j \left[q_j \frac{4\pi}{V_C} \sum_k \left(\frac{1}{k^2}\ e^{-\frac{k^2}{4\eta}} e^{-i(\mathbf{G}\cdot\mathbf{r})} \right) \right] - \frac{2q_i^2}{\epsilon_o}\sqrt{\frac{\eta}{\pi}} \tag{2.10}$$

At small internuclear distances (but larger than required for the aforementioned repulsion) there also exists an attractive force, the van der Waals - London interaction. This is a relatively weak force which arises from the generation of a spontaneously induced dipole on each of the interacting species, as was postulated by Debye [87]. With the aid of quantum mechanics, London was able to determine a general expression for this attraction, where the dipole arises due to the correlated motion of electrons [88–90]. In the case of two identical atoms, this force varies proportionally to r^{-6}. Although this is a quantum mechanical effect, the r^{-6} dependency can be derived from classical electrostatics. A complete derivation for the van der Waals - London force between two hydrogen atoms can be found elsewhere [91, 92]. However, it should be noted that this force is related to the polarizability of ions. As such, it is generally not considered for cation - cation interactions, where the cations tend to be small and unpolarizable [93].

Given this broad description of the short range repulsive energy, the functional forms which can be used to describe various terms can now be explained. Equation 2.1 denotes the short range interaction as Φ_{s-r}. This term can be expanded and expressed as:

$$\Phi_{s-r} = \sum_{ij} \Phi_{ij} + \sum_{ijk} \Phi_{ijk} + \sum_{ijkl} \Phi_{ijkl} + ... \tag{2.13}$$

where ij refers to all pair interactions, ijk refers to all three body interactions, and so on. Fortunately, the work in this thesis considers only cubic, strongly ionic materials. These types of materials are relatively isotropic, thereby warranting the consideration of only pair interactions (i.e. the first term of Equation 2.13). With that established, it is now useful to discuss the various forms of the pair short range potential that have been used in other studies.

The combination of a Coulomb term with a short range repulsive term, Φ_{ij}, was

first introduced by Born and Landé [94]:

$$\Phi_{ij} = \frac{b}{r^n} \tag{2.14}$$

where b and n are constants chosen to reproduce the equilibrium interionic distance and r is the nearest distance between unlike ions. Early work using this model took $n \approx 9$. This model was later expanded when it was discovered through quantum mechanical calculations that it could not be rigorously correct (though a surprisingly good approximation, especially for very ionic materials such as the alkali halides). In an attempt to update Equation 2.14 such that it accounted for the new quantum mechanical revelations, Born and Mayer [95] introduced a short range repulsive potential of the form:

$$\Phi_{ij} = Ae^{-\frac{r}{\rho}} \tag{2.15}$$

where A and ρ are adjustable parameters. Equation 2.14 now differed from 2.15 in that Equation 2.15 contains an exponential repulsive term. At this point, Born and Mayer also added an attractive term to account for the van der Waals interaction, which, as previously mentioned, had recently been calculated [88–91]. This term took the form of C/r^6, in accord with the work by van der Waals, London and Margenau, where C is an adjustable parameter. Mayer [96] later altered this attractive term for dipole quadropole interactions, such that it took the form of D/r^8.

A combination of the repulsive term in Equation 2.14 and the C/r^6 attractive van der Waals term results in the so called Lennard-Jones potential [97–99]:

$$\Phi_{ij} = -\frac{C}{r^6} + \frac{b}{r^n} \tag{2.16}$$

where the first term represents the attractive van der Waals potential. Lennard-Jones solved for b and C for several different values for n, ranging from 9 to 14. In modern calculations, the value for n is usually 12, though the Lennard-Jones

A is related the hardness of the ions, ρ describes the size of the ions while C is used to model the van der Waals interactions. This latter term can be calculated using the Slater-Kirkwood formulae [101]. The C term for identical interacting ions can be written as:

$$C_{ii} = \frac{3}{4}\alpha_i^{\frac{3}{2}} \cdot K_i^{\frac{1}{2}} \tag{2.18}$$

and for non-identical ions:

$$C_{ij} = \frac{3\alpha_i\alpha_j}{2[(\alpha_i/K_i)^{\frac{1}{2}} + (\alpha_j/K_j)^{\frac{1}{2}}]} \tag{2.19}$$

where α represents the static dipole polarizability and K is the effective electron number (i.e. the number of electrons which contribute to the polarizability). Values for α and K can be found elsewhere [102].

Short Range Potential Derivation

The success of the calculations described in this thesis depend critically upon the quality of the short range potentials. Therefore, it is essential that these terms are derived carefully in order to create an accurate description. There are essentially two principal methods of deriving potentials: empirically or by direct calculation. In this work, a combination of both methods was employed.

The empirical fitting of potentials has historically involved a reversed working of the methods described in previous sections, namely varying the short range parameters until the structural and lattice properties agree with experimental observation (as was done by Born and Landé [94]). Potentials are now chosen to reproduce a variety of properties, such as: elastic constants, high frequency and static dielectric constants and lattice energies. Any of these properties can be used in conjunction with the crystal structure for fitting. Initial values for the parameters are selected

and adjusted systematically via a least squares procedure:

$$F = \sum [f_{observed} - f_{calculated}]^2 \tag{2.20}$$

This adjustment is continued until the difference in Equation 2.20 is below a specified value. Advantages of this method include its relative simplicity as well as the ability to describe the full behaviour of a collection of atoms, including any partial covalency. However, there are several limitations of this method which need to be considered. Firstly, the crystal structure of complex oxides studied here (e.g. pyrochlores) has been determined via powder X-ray or neutron diffraction, whereas the other properties used for potential derivation (e.g elastic constants) are determined from large single crystals. Ideally, all data would come from the same crystal. If the same crystal was used, differences due to issues of chemistry (e.g. stoichiometry) would not occur. Structural data may also have inherent unreliability due to defects in the material. Furthermore, the lattice energies of these crystals are also subject to question due to the uncertainty in the second electron affinity of oxygen [103]. Harding *et al.* have closely examined the variation of the second electron affinity of oxygen with chemical composition and nuclear structure [104]. They found that assuming a single value of $\approx$ 8eV (as is usually the case) is erroneous due to this value varying with nuclear geometry and crystal structure.

A second limitation of empirical potential derivation is that only one point of the potential surface is calculated; namely, the equilibrium interionic separation. This becomes increasingly problematic when considering defective systems, as the interionic separation will shift away from the equilibrium position. To overcome the limitation of a single point interionic separation potential, parameters can be fit to a range of structures simultaneously (e.g. [105]). The resulting potentials relate to the ionic separations of several different structures, see Figure 2.5, and are therefore more *transferable* then if they were fit to a single structure.

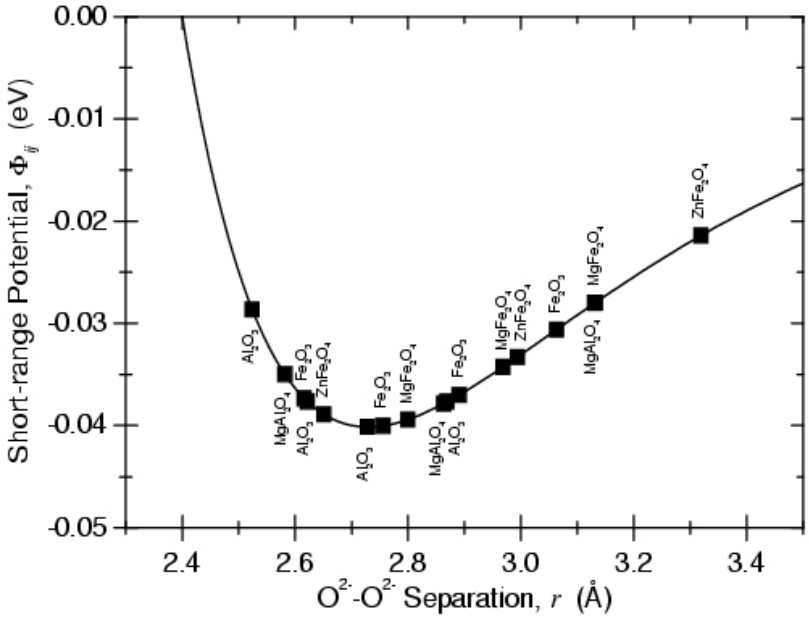

Figure 2.5: The series of compounds that the O^{2-} O^{2-} potential was fit to in order to derive this potential, reproduced from [105].

Potentials which are fit through direct calculation are derived through a number of methods, though all are based on quantum mechanics. Using techniques such as electron gas methods [106] or *ab initio* calculations [107], ionic positions are varied systematically to produce a potential energy surface that is a function of ion position. The inter ionic potential parameters are then fit to best reproduce this potential energy hyper surface.

An important point is that the potentials need to be derived in a consistent manner if they are to be used together. For example, cation - oxygen potentials describing different cations are not necessary compatible in the same simulation if they were derived with respect to different oxygen potentials. Although it may be useful to use empirical derivation and direct calculation in a concerted effort to

derive a set of potentials, it has been found that potentials obtained from different sources are generally not compatible [108].

2.1.3 Electronic Polarizability

The dielectric constant, ϵ, of a material is a measure of how effective an electric field, E, is in polarizing that material and can be expressed as:

$$\epsilon = 1 + 4\pi\frac{P}{E} = 1 + 4\pi\chi \tag{2.21}$$

where P is the polarization as defined as the dipole moment per unit volume and χ is the electric susceptibility. All of the terms in Equation 2.21 are macroscopic and easily measurable. In order to investigate microscopic phenomenon, a different property must be introduced. The *polarizability* is expressed as:

$$\alpha = \frac{p}{E_{local}} \tag{2.22}$$

where p is the dipole moment and E_{local} is the local electric field which produces the dipole. The polarizability can be thought of as a reciprocal force constant, if Equation 2.22 is rewritten as:

$$\alpha = \frac{e \cdot x}{F/e} = e^2\frac{x}{F} = e^2\frac{1}{\beta} \tag{2.23}$$

where β is the force constant of Hooke's law. As expressed in Equation 2.23, α has dimensions of volume.

In the model employed in this work, polarization is taken into account in two ways. In the first manner, ions are shifted slightly from their equilibrium positions subject to the restoring forces from adjacent ions. This is called displacement polarization. The second process involves the displacement of electrons around a fixed ion core or nucleus.

It is important to include this electronic polarizability in the methodology, especially when considering large ions and charged defects. However, including electronic polarizability increases the degrees of freedom and therefore the computational intensity. As a consequence, in this work, only anions and larger cations (e.g. Zr and Xe) are considered as polarizable in the second manner described.

To account for electronic polarizability, the shell model devised by Dick and Overhauser is employed [109]. This model describes each ion as consisting of a core of charge $X \cdot e$ and a corresponding shell of charge $Y \cdot e$, such that the total charge of the ion is $(X + Y) \cdot e$. The massless shell is coupled to the massive core by a spring of force constant k (see Figure 2.6), such that the polarizability of the free ion, α_e, can be expressed as:

$$\begin{aligned} \alpha_e &= \frac{1}{4\pi\epsilon_o}\left(\frac{Y^2}{k}\right) \\ &= 14.3994\left(\frac{Y^2}{k}\right) \end{aligned} \tag{2.24}$$

where ϵ_o is the permittivity of free space and the numerical constant applies if Y is in electron charge units and k is in units of ev·Å^2. This expression is similar to Equation 2.23, where α is in units of Å^3.

model does not appropriately account for the Cauchy violation [111]. If the three components of the stress tensor are given as X_1, X_2 and X_3, and the three shear components are given as X_4, X_5 and X_6, then the Hooke stress - strain relation can be expressed as:

$$X_i = \sum_{j=1}^{6} c_{ij} x_j \tag{2.25}$$

where c_{ij} are the thirty-six elastic constants. For cubic crystals, there are certain equalities:

$$c_{11} = c_{22} = c_{33}; \qquad c_{12} = c_{23} = c_{31}; \qquad c_{44} = c_{55} = c_{66}; \tag{2.26}$$

The rest of the matrix is zero if the coordinate axes and the cube axes are parallel, thus leaving only three independent components. Equivalent relations can be derived for hexagonal crystals. Even more relations can be derived if the atoms of the crystal interact with central forces (as they do in the shell model). These are the so called Cauchy-Poisson relations, for which there exist expressions for cubic and hexagonal structures. The cubic relation is as follows:

$$c_{12} = c_{44} \tag{2.27}$$

(A more thorough derivation of the Cauchy-Poisson relations can be found in Chapter II, Section 15 of Seitz's Modern Theory of Solids [112]). Unfortunately, real materials often violate Equation 2.27. For example, Table 2.1, where E is the principal Young's modulus, demonstrates that for common materials such as rocksalt and KCl, the Cauchy relation is considerably violated [113].

Material	E	c_{11}	c_{12}	c_{44}
Fluor Spar	1470	1670	457	345
Rock-salt	418	477	132	129
Potassium Chloride	372	375	198	65.5

Table 2.1: Experimental values for elastic constants demonstrating the violation of the Cauchy relation, reproduced from [113].

However, because the shell model is limited by perfect spherical symmetry, it is unable to account for this violation. Certain modifications can be made to the shell model so it is able to model the Cauchy violation. Schroder has introduced a *breathing shell*, which allows the shell to distort spherically, thus adding another degree of freedom [114]. However, this model only works for cases when $c_{12} < c_{44}$. When $c_{12} > c_{44}$, Sangster has developed a modification which allows for ellipsoidal modifications to the shell [115]. In this work, neither of these modifications have been used, but they are acknowledged as potentially useful.

2.1.4 Energy Minimization

In order for the aforementioned model to be useful in predicting perfect lattice properties, it must be combined with an energy minimization technique in order to bring the system to a state of mechanical equilibrium [116]. In this work, all ionic interactions are calculated and each ion subsequently moves a distance proportional to the force acting on the particle in the direction of the overall field. There are two procedures to minimize the lattice energy: either at constant volume or constant pressure. Constant volume minimization determines the minimum energy via ionic coordinates, where only the strains on individual ions are considered. For

constant pressure techniques, it is necessary to determine the minimum energy not only through the adjustment of ionic coordinates, but also unit cell dimensions, accounting for the strains both on individual ions as well as the unit cell.

Under constant volume conditions the lattice energy U_L can be expanded to the second order about a point r, and for the new set of coordinates r' can be expressed as:

$$U_L(r') = U_L(r) + g^T \cdot \delta + \frac{1}{2}(\delta^T \cdot \mathbf{W} \cdot \delta) \tag{2.28}$$

In Equation 2.28, g is the first derivative of the lattice energy with respect to ionic positions:

$$g = \frac{\partial U_L}{\partial r} \tag{2.29}$$

δ is the displacement (or strain) of a given ion:

$$\delta = r' - r \tag{2.30}$$

and $\mathbf{W}$ is the second derivative of the lattice energy with respect to r:

$$\mathbf{W} = \frac{\partial^2 U_L}{\partial r^2} \tag{2.31}$$

At equilibrium, the change in energy with respect to strain is zero. Therefore:

$$\frac{\partial U_L(r')}{\partial \delta} = 0 = g + \mathbf{W} \cdot \delta \tag{2.32}$$

The optimum ion displacement to give rise to the minimum lattice energy is:

$$\delta = -\mathbf{W}^{-1} \cdot g \tag{2.33}$$

or:

$$\delta = -\mathbf{H} \cdot g \tag{2.34}$$

where **H** is the Hessian matrix is the inverse of the second derivative of the lattice energy with respect to ionic displacement.

The energy of the systems considered in this work are not harmonic, thus the energy minimum can not be arrived at in a single step. Rather, subsequent displacements, in general, result in lower energy configurations. Thus, the ionic coordinates are adjusted iteratively until the forces on the atoms are zero. There are two methods of energy minimization employed in this work: Newton-Raphson and Conjugate Gradient.

All Newton-Raphson type formulae (e.g. the Borgden, Fletcher, Goldfard, Shanno formula [117]) serve to iteratively update the Hessian matrix, **H**, from Equation 2.34:

$$r_{n+1} = r_n - H_i \cdot g_i \tag{2.35}$$

This however requires the storage of the Hessian matrix of second derivatives, which is computationally intensive. Furthermore, solving for the second derivative matrix at each step would result in a less than expeditious overall calculation. For this reason, Conjugate Gradient type minimizations are also employed. These only require the calculations of the first derivatives of the lattice energy:

$$\beta = \frac{g_{i-1}^T \cdot g_{i-1}}{g_{i-2}^T \cdot g_{i-2}} \tag{2.36}$$

Conjugate Gradient calculations are computationally less expensive than those of the Newton-Raphson variety and converge quickly when far from the lattice energy minimum. However, when near the minimum, the Conjugate Gradient technique becomes less efficient due to the small gradients. Thus, a combination of these two techniques is used during the minimization process, beginning with Conjugate Gradient as a coarse refinement until a certain small gradient is met and then switching to Newton-Raphson type methods in order to finalize the minimization.

In depth mathematical discussions of energy minimization (including constant pressure minimization) can be found elsewhere [118, 119].

2.2 Defective Lattice

To paraphrase F.C. Frank, "materials are like people, it is their defects that make them interesting." Certainly the importance of defects controlling and modifying materials is clear and is the central theme of this thesis. Therefore, the model developed in the previous section to describe the perfect lattice will be expanded to account for defective systems. In this work, the method accounting for the defective lattice is based on a minimization of the total energy of a system by relaxing ions around a defect. The effect is confined to a short distance from the defect, which is facilitated by the use of a *two region* approach when calculating defect energies, see Figure 2.7. The response of the ions in the inner Region I is evaluated explicitly while the response of the ions in the outer Region II is treated as a continuum and is therefore more approximate.

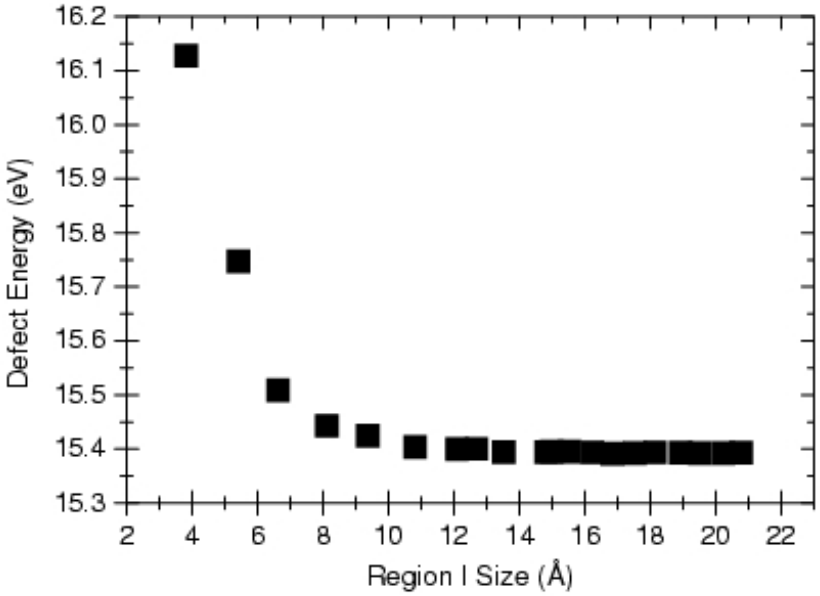

Figure 2.8: The effect of Region 1 size on defect energy, for the case of an $(V_O)^{\cdot\cdot}$ in CeO_2, reproduced from [105].

System	Region I (Å)	Region IIa (Å)
UO_2	13.67	24.06
Pyrochlores	≈10.0	≈30.0

Table 2.2: Region I and IIa radii.

Region II is subdivided into Region IIa and Region IIb. Region IIa serves as an interface between Region I and Region IIb (which extends to infinity). The changes in energy of the ions in Region IIa due to the defect and the relaxation of ions in

Region I are calculated explicitly. However, the displacements of Region IIa ions are determined in a single step by calculating the forces on these ions using the Mott-Littleton approximation [120]. This approximation is applicable since the defect is assumed to have only a small effect on the ions in Region IIb. Therefore, the entire response of Region IIb is approximated by the Mott-Littleton method.

The complication the Mott-Littleton method addresses is that the forces on any ion are not only due to the charged defect, but also to the dipoles which have been induced in the region of the lattice around the defect. This polarization can be approximately given by:

$$P = \frac{q}{4\pi r^2}\left(1 - \frac{1}{\epsilon}\right) \tag{2.37}$$

where P is the polarization, q is the charge of the defect, r is the distance from that defect and $\epsilon = \epsilon_s \epsilon_o$.

According to the conventional treatment of the defective lattice (as developed by Lidiard and Norgett [121] and Norgett [122]), the total energy of the solid containing a defect can be expressed as:

$$E = E_1(\underline{x}) + E_2(\underline{x}, \underline{\zeta}) + E_3(\underline{\zeta}) \tag{2.38}$$

where $E_1(\underline{x})$ is the energy of Region I, $E_2(\underline{x}, \underline{\zeta})$ is the energy of the interfacial Region IIa and $E_3(\underline{\zeta})$ is the energy of Region IIb. The two independent vectors $(\underline{x})$ and $(\underline{\zeta})$ are the coordinates of ions in Region I and Region II, respectively. As $E_3(\underline{\zeta})$ involves an infinite number of displacements, it can not be solved explicitly. However, if the displacements are assumed to be quasi-harmonic, it can then be defined as:

$$E_3(\underline{\zeta}) = \frac{1}{2}\underline{\zeta} \cdot \mathbf{A} \cdot \underline{\zeta} \tag{2.39}$$

where $\mathbf{A}$ is the force constant matrix. This expression can substituted into Equation 2.38 and at the equilibrium condition:

$$\frac{\partial E}{\partial \underline{\zeta}} = \left.\frac{\partial E_2(\underline{x}, \underline{\zeta})}{\partial \underline{\zeta}}\right|_{\underline{\zeta}=\overline{\underline{\zeta}}} + \mathbf{A} \cdot \overline{\underline{\zeta}} = 0 \tag{2.40}$$

thus leading to an alternate expression for $E_3(\underline{\zeta})$:

$$E_3(\underline{\zeta}) = \frac{1}{2} \left.\frac{\partial E_2(\underline{x}, \underline{\zeta})}{\partial \underline{\zeta}}\right|_{\underline{\zeta}=\overline{\underline{\zeta}}} \cdot \overline{\underline{\zeta}} \tag{2.41}$$

which also leads to an alternate expression for the total energy:

$$E = E_1(\underline{x}) + E_2(\underline{x}, \underline{\zeta}) - \frac{1}{2} \left.\frac{\partial E_2(\underline{x}, \underline{\zeta})}{\partial \underline{\zeta}}\right|_{\underline{\zeta}=\overline{\underline{\zeta}}} \cdot \overline{\underline{\zeta}} \tag{2.42}$$

where $\overline{\underline{\zeta}}$ are the equilibrium coordinates of $\underline{\zeta}$. The total defect energy can then be calculated by minimizing with respect to $\underline{x}$ and $\underline{\zeta}$.

2.3 Surface Energy Calculation

As mentioned in Chapter 1, a surface can be thought of as a large defect. Therefore, many of the previously mentioned methods can be employed when modelling surfaces. In the case of surface calculations, a unit cell is defined, cut in a specified orientation and duplicated via periodic boundary conditions in 2D, see Figure 2.9. In the third dimension the repeat block of material including the surface extending approximately 30Å in the bulk constitutes Region I. Beneath that is an additional 30Å of material, Region II, in which the ions retain their perfect lattice position. This Region II is not able to polarize in response to the surface, which, as will be seen, places an important limitation on our calculations. The interactions between ions are treated the same as when considering bulk defects, namely a long range Coulomb interaction and a short range potential. Again, the Buckingham potential has been employed when considering surfaces, as it has been for bulk materials.

2.4 Computational Codes

2.4.1 CASCADE

CASCADE (**C**ray **A**utomatic **S**ystem for the **Ca**lculation of **D**efect **E**nergies) was written in Fortran at the Daresbury Laboratory [127], specifically for the CRAY-1 computer. In this study, CASCADE is exclusively used for perfect lattice calculations and for defect energy calculations.

2.4.2 GULP

GULP (**G**eneral **U**tility **L**attice **P**rogram) is an improvement from earlier codes in that it has an automated empirical fitting of potential parameters feature. This feature subsequently allows for a simultaneous multi-structural fit routine.

2.4.3 MARVIN

MARVIN'S (**M**inimization **A**nd **R**elaxation of **V**acancies and **I**nterstitals for **N**eutral **S**urfaces) Program was developed at the Royal Institution of Great Britain for studying surfaces and interfaces [77]. MARVIN is based upon a similar code, MIDAS, developed by Tasker in the late 1970's [73]. MARVIN improves upon the MIDAS code by utilizing the increase in computer capability to calculate the surface energies of not only simple cubic crystals, but also more complex carbonates, sulfates, phosphates, etc. MARVIN also allows for the introduction of ions and molecules to the surface, which is important in modelling crystal growth and catalysis.

MARVIN considers a simulation cell of a finite number of atoms, which are repeated in 2D (as previously described). The cell consists of a Region I and II. In this regard, MARVIN is similar to CASCADE, in that it relaxes Region I atoms explicitly whereas those in Region II remain fixed. The total energy of the system is

defined as the energy of all the Region I structural units, all the Region II structural units and the periodic images of both regions. Since only two body terms are considered, the total energy can be expressed as:

$$E_{\text{total}} = \sum_{a}^{N_I} \left[\frac{1}{2} \sum_{l \neq 0} V_{aa}(|l|) + \frac{1}{2} \sum_{b \neq a}^{N_I} \sum_{l} V_{ab}(|r_{ab} + l|) + \sum_{b}^{N_{II}} \sum_{l} V_{ab}(|r_{ab} + l|) \right] \tag{2.43}$$

where N_I is the total number of particles in all Region I, N_{II} is the total number of all particles in Region II, l are the 2D lattice vectors and r_{ab} is the vector between particle a and particle b. The first term inside the brackets describes the interactions between a particle and its periodic images. The second term describes the interactions between all Region I particles and their images. The third terms describes the interaction between Region I and Region II.

Perfect lattice energies calculated with CASCADE can be used to determine total energies, which are subsequently used in MARVIN because both codes use energy minimization techniques and identical forces. Therefore, the energies calculated are comparable.

The MARVIN code has been used in the past to predict atomistic interaction between atomic force microscope tips and ionic surfaces [128] as well as to predict the morphology of UO_2 [45].

2.5 Listing of Short Range Potentials

Table 2.5 lists the short range Buckingham potentials used throughout this work. Shell parameters are given in Table 2.5. In each of these tables, the origination of the potential is referenced, though it should be noted that there is consistency between them as they were all derived within the Atomistic Simulation Group of

Imperial College and with respect to the same O^{2-}-O^{2-} potential.

Species	A (eV)	ρ (Å)	C (eV·Å^6)	Reference
O^{2-}-O^{2-}	9547.96	0.2192	32.0	[129–134]
Lu^{3+}-O^{2-}	1618.80	0.33849	16.27	[133, 135]
Yb^{3+}-O^{2-}	1649.80	0.3386	16.57	[105]
Er^{3+}-O^{2-}	1739.91	0.3389	17.55	[105]
Dy^{3+}-O^{2-}	1807.84	0.3393	18.77	[135]
Pr^{3+}-O^{2-}	2055.35	0.3438	23.95	[105]
Y^{3+}-O^{2-}	1766.40	0.33849	19.43	[134]
Gd^{3+}-O^{2-}	1885.75	0.3399	20.34	[105]
Eu^{3+}-O^{2-}	1925.71	0.3403	20.59	[105]
Sm^{3+}-O^{2-}	1944.44	0.3414	21.49	[105]
Nd^{3+}-O^{2-}	1995.20	0.3430	22.59	[105]
La^{3+}-O^{2-}	2088.89	0.3460	23.25	[105]
Ti^{4+}-O^{2-}	2131.04	0.3038	0.0	[136]
Ru^{4+}-O^{2-}	1215.78	0.3441	0.0	[105]
Mo^{4+}-O^{2-}	1223.97	0.3470	0.0	[105]
Sn^{4+}-O^{2-}	1414.32	0.3479	13.66	[105]
Pb^{4+}-O^{2-}	1640.34	0.3507	19.50	[105]
Zr^{4+}-O^{2-}	1502.11	0.3477	5.10	[105]
Ce^{4+}-O^{2-}	1809.68	0.3547	20.40	[137]
U^{4+}-O^{2-}	1761.78	0.3564	0.0	[138]
Ba^{2+}-O^{2-}	905.70	0.3976	0.0	[139]
Sr^{2+}-O^{2-}	682.17	0.3945	0.0	[138]
Kr^{0}-O^{2-}	800.38	0.3888	52.48	[154]
Xe^{0}-O^{2-}	598.00	0.4257	76.96	[154]
Kr^{0}-U^{4+}	5912.78	0.3191	50.34	[36]
Xe^{0}-U^{4+}	6139.16	0.3395	71.84	[36]

Table 2.3: Short-range pair potential parameters.

Species	Y (e)	k (eVÅ^{-2})	Reference
O^{2-}	-2.04	6.3	[129–134]
U^{4+}	-0.10	160.0	[129]
Zr^{4+}	-0.05	189.7	[105]
Pb^{4+}	-0.05	205.0	[105]
Ce^{4+}	-0.20	177.84	[105]
Kr^{0}	-9.90	573.7	[36]
Xe^{0}	-11.3	460.8	[36]

Table 2.4: Shell parameters.

Chapter 3

Solution of Fission Products in UO_2

"As things stand, I find it very difficult to assume such a degree of 'bursting,' but we've had so many surprises in nuclear physics that one can't very well say it's impossible."

Lise Meitner

Letter to Otto Hahn, Dec. 21 1938

3.1 Introduction

UO_2 is the standard nuclear fuel used in modern, conventional power reactors (e.g. PWR, BWR and AGR). The oxide phase of fissile uranium provides the necessary thermodynamic stability required in operating conditions. It then follows that an extensive knowledge of the properties of this material is necessary. Unfortunately, experimental research is costly, especially if fission products are considered. Therefore, computer simulation is a desirable alternative. In this chapter, an attempt is

made to clarify the situation of the existing, but conflicting sets of data concerning the solution of defects corresponding to fission products.

3.2 Previous Work

3.2.1 The Chemical State of Fission Products

As mentioned previously in Chapter 1, fission products will vary chemically and physically, such that absolute yield is not the only important consideration. Several attempts have been made to classify fission products into categories based on their chemistry [37, 140], see Figure 3.1. The chemical state of fission products is important in that the chemical state influences the physical properties of the fuel, e.g. thermal conductivity, swelling, melting point, etc. [37].

ton and xenon, bromine and iodine are chemically reactive with other species in this gap [145]. In fact, it has been suggested that iodine may react with the zircalloy fuel cladding material thus leading to stress related cracking [146]. Until this issue has been settled, reactor design must account for non-appreciable concentrations of iodine in the fuel cladding gap.

A number of other fission products precipitate out of solution in the form of a complex oxide, which is referred to as the "grey phase." The composition of grey phase precipitates will vary with fuel composition and reactor history, though the main constituents include Ba, Zr and U, see Figure 3.1. The most commonly reported precipitates are perovskites of the type $[Ba_{1-x-y}Sr_xCs_y]$(U, Pu, Ln, Zr, Mo)O_3 which are essentially substituted $BaZrO_3$ [147].

The fission products found in solid solution include Sr, Y, Nb and the lanthanide ions. The extent of Sr solubility is dependent on the metal to oxygen ratio. For example, the solubility of Sr is over ten times higher in UO_2 than $UO_{1.94}$ [37]. It has also been suggested that Sr is more soluble than its chemical relative Ba [148]. It is then likely that Sr will remain in the fuel while Ba will precipitate in the grey phase. It has also been observed that chemical relatives Ce and Zr exhibit different solubilities, where Ce is more soluble than Zr [149]. Concentrations of CeO_2 in excess of what is the result of fission (at usual burnups) have shown complete solubility in a range of UO_2 non-stoichiometries down to room temperature. ZrO_2 is only soluble above 1350^oC.

The remaining quarter of fission products will precipitate out of solution in the form of metallic inclusions. These precipitates are known as the "white phase," and are comprised mainly of 4d transition metals Mo, Tc, Ru, Rh and Pd [37].

3.2.2 Calculation of Fission Product Solution Energy

Motivated by the fundamental diversity of uranium dioxide and subsequently its technological importance, great interest has been placed upon this material. To reiterate, experimental studies on this material are very difficult indeed, given the extreme conditions of greatest technological importance. UO_2 thus lends itself to reliable theoretical studies. Early studies on defects in UO_2 [150] demonstrated the viability of pair potential calculations, deriving suitable parameters and calculating a range of defect energies which were in accord with the experimental data of the time.

These early studies prompted the development of more refined studies. Later studies calculated with increased accuracy: defect formation, clustering, migration and solution energies [151–153]. Initial fission product studies were confined to the volatile fission products Xe and Kr [154–158], which determined the solution sites of these fission products as a function of stoichiometry.

Of particular relevance to this work is that of Grimes and Catlow [36], whose paper on the stability of fission products provides a review of the experimentally demonstrated behaviour of fission products and proceeds to discuss the development of a theoretical model which incorporates all of the constituents required to simulate the properties of fission products in UO_2 at thermodynamic equilibrium. The calculations of that study were carried out at the atomistic level, employing the methodology described in Chapter 2. The work considered the solution of fission products at existing trap sites. With the eventuality of fission products outnumbering existing trap sites, the energy to form trap sites was included. In order to facilitate this, trap site equilibria for Frenkel and Schottky intrinsic defects had to be calculated. From these calculations, Grimes and Catlow were able to predict equilibrium solution sites for many fission products at different stoichiometries.

It was found that the equilibrium solution site is stoichiometry dependent. For example, the low energy solution site for Xe in hypo-stoichiometric UO_{2-x} and stoichiometric UO_2 was the neutral tri-vacancy. However, for hyper-stoichiometric UO_{2+x}, the lowest energy site was the uranium vacancy. Similar behaviours were observed for other fission products. The calculated low energy solution sites for Xe, Cs and Rb were all substantiated by experiment [159], but there exists no other experiment with which to compare the remaining data.

The solution of oxides was also considered using this model (e.g. Cs_2O, BaO, La_2O_3 and ZrO_2). A significant aspect of this model is that it is able to predict the differences in the variation of solubility with stoichiometry exhibited by fission product compounds. There is certainly room to expound the behaviour of the components of fission product precipitates with changing fuel history.

There have also been recent *ab initio* UO_2 point defect studies [160–162]. These studies employ the local-density approximation and apply it to density-functional theory. The defect energies are calculated using a linear muffin-tin orbital super-cell method. In this supercell method, a characteristic region is defined and then repeated periodically. Due to the complexity of these calculations, the supercells are rather small, for example 12 and 24 atoms in the work of Petit *et al.* [161]. A limitation of this type of calculation is that the atoms surrounding the defect are not permitted to relax on account of the defect.

In regard to formation energies of oxygen and uranium vacancies, interstitials and Frenkel pairs as well as Schottky trio defects, the *ab initio* results are in good agreement with the aforementioned classical studies. However, those authors contest that there are discrepancies with the classical studies when confronting the issue of the location of Kr atoms [160]. This was due to a misunderstanding of the definitions of solution and incorporation energy as defined by Grimes and Catlow [36]. Once

corrected, the *ab initio* and classical results agree remarkably well. The discrepancy and its origin are discussed in detail in Section 3.3 and have been previously published in a letter by Stanek *et al.* [163].

3.3 Location of Krypton Atoms in UO_2

In a recent paper, Petit *et al.* [160] discussed their results concerning an *ab initio* study of the location of krypton in UO_2. The results from this study were compared to similar studies, which employed different techniques, namely experimental [142, 164] (Rutherford backscattering) and theoretical (energy minimization based on pair potentials) [36]. The paper concludes that their result (of the neutral tri-vacancy trap site providing the lowest solution energy for Kr) is in agreement with experiment, but in contradiction with previous theoretical studies. Petit *et al.* suggest that the "crude approximation made in semi-empirical (pair potential) schemes can explain some of the discrepancies with the results obtained in the present study." It is our understanding that it is not the approximations inherent to pair potentials, but rather a misinterpretation of terms which has led to the discrepancy and in fact the two sets of results agree remarkably well.

3.3.1 Discussion

In the previous work by Grimes and Catlow [36], two definitions were given for the energy associated with placing fission products in the UO_2 lattice. The first was the incorporation energy (i.e. the energy to place a fission product at a pre-existing trap site). The energies of two atomic configurations must be calculated: the empty trap site and the fission product at the trap site. Then, the incorporation energy is given by:

$$\begin{array}{ccccc} \text{incorporation} & = & \text{energy of fission product} & - & \text{energy of empty} \\ \text{energy} & & \text{in trap site} & & \text{trap site} \end{array}$$

Inherent in this definition is the assumption that there are more trap sites than fission products. Given the large defect energy of trap sites (defined as the calculated energy to remove the appropriate ions from the lattice to infinity), this is unlikely to be the case. Therefore, a second definition was made, the solution energy. This assumes that for the fission product to be accommodated in the lattice, the energy to form the trap site in equilibrium with the majority Frenkel intrinsic defects must be accounted for. The solution energy is then:

$$\begin{array}{ccccc} \text{solution} & = & \text{incorporation} & - & \text{equilibrium trap} \\ \text{energy} & & \text{energy} & & \text{formation energy} \end{array}$$

Of course the equilibrium trap formation energy is a strong function of stoichiometry. The energies for equilibrium trap formation are given in Tables 3.1 and 3.2, where Table 3.1 denotes how each energy is calculated and Table 3.2 provides the corresponding values [36].

Trap Site	UO_{2-x}	UO_2	UO_{2+x}
oxygen vacancy	nil	$\frac{1}{2}E_F$	E_F
uranium vacancy	E_S	E_S-E_F	E_S-$2E_F$
di-vacancy	E_S-B_{DV}	E_S-$\frac{1}{2}E_F$-B_{DV}	E_S-E_F-B_{DV}
neutral tri-vacancy	E_S-B_{NTV}	E_S-B_{NTV}	E_S-B_{NTV}
charged tetra-vacancy	$2E_S$-B_{CTV}	$2E_S$-E_F-B_{NTV}	$2E_S$-E_F-B_{NTV}

Table 3.1: The effective energy to form a trap site, where E_S is the Schottky trio formation energy = 13.34eV; E_F is the Frenkel pair formation energy = 6.82eV; B_{DV} is the binding energy of a di-vacancy = 3.24eV; B_{NTV} is the binding energy of a neutral tri-vacancy = 4.93eV; B_{CTV} is the binding energy of a charged tetra-vacancy = 8.89eV. Reproduced from [36].

We are now in a position to understand the confusion. Petit *et al.* [160] calculated incorporation energies which were then erroneously compared to the solution energies of Grimes and Catlow [36]. Petit *et al.* [160] found the discrepancy puzzling since the agreement between the two sets of calculations is correct for simple point defects (interstitial, oxygen and uranium vacancies) but very poor for more complex structures (divacancy and neutral tri-vacancy). This discrepancy can easily be explained. The trap site formation energy for simple point defects is either negligible or zero, whereas for more complex defect structures there is a more substantial trap site formation energy, see Table 3.2. For example, there is a 5eV disparity between the trap site formation energies of an oxygen vacancy and a neutral tri-vacancy in stoichiometric UO_2.

Trap Site	UO_{2-x}	UO_2	UO_{2+x}
oxygen vacancy	0.0	3.41	6.82
uranium vacancy	13.34	6.51	-0.31
di-vacancy	10.09	6.68	3.27
neutral tri-vacancy	8.41	8.41	8.41
charged tetra-vacancy	17.78	10.96	4.13

Table 3.2: Calculated values for trap site formation energies in eV, according to Table 3.1, reproduced from [36].

To rectify the discrepancy, the pair potential trap site formation energies of Grimes and Catlow [36] are added to the *ab initio* incorporation energies of Petit *et al.* [160], resulting in hybrid *ab inito*/pair potential values, see Table 3.3. Unfortunately, there is insufficient past data from which to formulate *ab initio* trap site formation energies [161, 165, 166].

	Grimes (pair potential)			Petit (hybrid *ab initio*/pair potential)		
Krypton location	UO_{2-x}	UO_2	UO_{2+x}	UO_{2-x}	UO_2	UO_{2+x}
interstitial	13.3	13.3	13.3	14.2	14.2	14.2
oxygen vacancy	9.9	13.3	16.8	8.0	11.4	14.8
uranium vacancy	17.2	10.3	3.5	16.3	9.5	2.7
di-vacancy	12.5	9.0	5.7	12.5	9.0	5.7
neutral tri-vacancy	9.5	9.5	9.5	9.8	9.8	9.8
charged tetra-vacancy	19.1	12.3	5.5	-	-	-

Table 3.3: Comparison of calculated solution energies of a krypton atom in uranium dioxide

3.3.2 Conclusion

When corrected for trap site formation energy, the hybrid *ab initio* results agree remarkably well with the pair potential results, especially for those complex defect structures which provide the most stable solution sites. However, what should also be noted from these studies is the predicted preference for Kr solution at di-vacancies in stoichiometric UO_2. Furthermore, that these two studies agree does not invalidate the agreement with experiment. The experimental work was conducted on Xe, which is a considerably larger atom than Kr and consequently, solution is expected at the larger neutral tri-vacancy trap, despite the chemical similarity of Kr and Xe. Of course, a hybrid *ab initio*/pair potential calculation is not entirely satisfactory. Therefore, it would be beneficial to calculate the equilibrium solution site energies *ab initio*. It is accepted that good quality *ab initio* simulations are inherently more reliable than pair potential calculations. However, in the event of a more complete comparison between the techniques, attention should also be paid to the difference between large unit cell simulations [160] and isolated defect cluster calculations that relate to the infinite dilute limit.

Chapter 4

Segregation of Fission Products to UO_2 Surfaces

"But we know from observation that it is only within very small distances of such a surface that any mass is sensibly affected by its vicinity, - a natural consequence of the exceedingly small sphere of sensible molecular action."

J.W. Gibbs

On the Equilibrium of Heterogeneous Substances, 1875

4.1 Introduction

Segregation of fission products to the stable low index surfaces of UO_2 has been predicted using atomistic simulation techniques. Three pairs of fission products were considered: isolvalent Ce^{4+} and Zr^{4+}, divalent Ba^{2+} and Sr^{2+} and zero valent Kr^{o} and Xe^{o}. The divalent and zero valent fission products are charge compensated by oxygen vacancies. Three low index surfaces are considered: (110), (111) and (100). The (100) surface is dipolar (Type III) and therefore unstable. Thus, a series

of surface defects must be incorporated to neutralize the dipole. The dependence of segregation upon specific surface type, configuration of surface defects on dipolar surfaces, defect cluster geometry and fission product chemistry is discussed.

4.2 Previous Work

4.2.1 Experimental Segregation Studies

Properties of oxide materials (e.g. strength, sinterability, conductivity, creep, etc.) are governed to a large extent by defects as well the structure and stability of surfaces and interfaces. Understanding the segregation of impurities to these surfaces and interfaces will therefore be important in controlling materials properties. Unfortunately, experiments in this area are few, attesting to the difficulty of these types of study. The seminal work of McCune and Wynblatt [167] has served as an impetus to motivate further work. They investigated the segregation of Ca^{2+} to the (100) surface of the prototypical ionic ceramic, MgO, by using low energy ion scattering spectroscopy and Auger spectroscopy to measure equilibrium surface coverage. Roshko and Kingery similarly looked at segregation of Ca^{2+} in MgO [168], but rather than to (100) surfaces, they investigated three high angle grain boundaries using scanning transmission electron microscopy. They found different segregation behaviour for Ca to the different boundaries, suggesting that grain boundary structure does have an effect on segregation.

In order to better understand the phenomenon whereby MgO beneficially affects the sintering of Al_2O_3, Baik, Mukhopadhyay, Blakely *et al.* investigated the segregation of Mg and Ca to Al_2O_3 surfaces [63, 169, 170]. Early grain boundary experiments on MgO doped Al_2O_3 surprisingly revealed the segregation of Ca [171]. This observation was interesting considering that the concentration of Ca in the bulk

was between 5 and 15 ppm. In similar surface sensitive experiments, Ca was also found [172–174]. Unfortunately, Ca has a detrimental effect on densification [175]. Nevertheless, due to these early segregation studies, Baik, Mukhopadhyay, Blakely *et al.* were forced to consider Ca as well as Mg in their experiments.

An interesting result from the work of Mukhopadhyay *et al.* is that the segregation behaviour of both Ca and Mg was different for the $(10\bar{1}0)$ prismatic plane than it was for the (0001) basal plane of Al_2O_3. The effective heat of segregation for Mg was found to be lower for the basal plane than the prismatic plane, although qualitatively similar (differing only by ≈0.5eV) [63]. Baik and White found that Ca did not segregate to the (0001) surface while there was strong segregation to the $(10\bar{1}0)$ surface [169].

4.2.2 Modelling Segregation Studies

The simulation of segregation can be considered as a progression of the early computational work of the type mentioned in Chapters 2 and 3. Much of the methodology is based exactly on the earlier bulk material and surface methodology. As mentioned in the previous section, experimental segregation studies are very difficult to perform. It then follows that simulation studies concerned with segregation can be potentially useful in providing information where equivalent experimental work would be rather challenging. Furthermore, simulations can be a valuable tool not only in predicting segregation behaviour, but also in complimenting or directing experimental work.

That said, there have been relatively few segregation simulation studies compared to equivalent studies of bulk materials or even surface structure. Nevertheless, several simulation methods for determining segregation trends have been applied. Monte Carlo techniques have been used previously in metals [176, 177], but until

recently have not been used in ionic solids because of their computational intensity. Harding *et al.* have used modified, kinetic Monte Carlo techniques to investigate diffusion in grain boundaries in the ionic solids NiO and Al_2O_3 [178], but not segregation to these boundaries.

The early work of Tasker and co-workers used similar techniques as described in Chapter 2 to determine surface energetics and segregation trends in metal oxides [76, 179–181]. In the first of these studies [76], Tasker *et al.* combined detailed atomistic simulation techniques with simple statistical mechanics to describe Ca segregation to surfaces of MgO. Results obtained using potentials derived both empirically and by quantum mechanical calculations were in agreement with the experimental results of McCune and Wynblatt discussed previously [167]. Defect formation energies near surfaces and grain boundaries were also investigated [179, 180]. In these studies, it was found that defect formation energies vary with depth from the surface or boundary. This result suggests that the population and kinetics of defects are surface or boundary dependent. Tasker *et al.* then expanded the scope of their work by considering the segregation of Be, Mg, Ca, Ba and Ni to (001) and (110) surfaces of MgO and CaO [181]. Not only did this seminal paper investigate the concentration and segregation of defects at the surfaces of MgO and CaO, but also accounted for ensuing effects, such as facetting. It was also shown that dopants near the surfaces of MgO and CaO can have important effects on the structure and properties. An interesting review can be found in another paper by Tasker [182].

Cotter *et al.* also investigated Ba segregation in MgO, both experimentally with XPS and theoretically using atomistic simulation techniques [183]. Unfortunately, the scatter in the experimental data was too large to allow meaningful comparison with the modelling results. Cotter *et al.* also specifically assumed that the vibrational entropy of segregation was small compared with the enthalpy of segre-

gation [183].

With a method well established to determine segregation trends to surfaces of simple oxides, more complex materials were duly investigated. Davies *et al.* investigated the segregation of various dopants to surfaces of oxides with the corundum structure [184]. In contrast to the Langmuir adsorption model, their results suggest that segregation enthalpy is coverage dependent. Their results for Ca segregation to the prismatic plane of Al_2O_3 qualitatively agree with the previously mentioned results of Baik *et al.* [169], though they noted that the results for the basal plane were not as convincing, citing the complexity of the segregation phenomenon.

A review of the work conducted at the University of Bath is provided in [185]. Not only does this paper detail the simulation of impurity segregation to surfaces of Al_2O_3 and ZrO_2, but also discusses morphology as well as the generation of segregation paths via molecular dynamics. Of particular relevance to the work in this thesis is the study by Sayle *et al.*, which investigated the segregation of Rh^{3+}, Pd^{2+} and Pt^{2+} to the (111) and (110) surfaces of CeO_2 [186]. For Pd^{2+} and Pt^{2+}, they found preferential segregation of isolated defects as well as the formation of coherent second phases at the (111) surface.

The work of Sayle *et al.* paved the way for more recent studies, such as that of Slater *et al.* [187]. This work investigated the segregation of Sb to the (110) and (001) surfaces of SnO_2. Applications for SnO_2 include gas sensors and thin film coatings, and the conductivity of this material may be enhanced by doping with Sb or by forming oxygen vacancies. However, both Sn and Sb exhibit variable charge states, which increases the number of potential contributing defects. Slater *et al.* therefore began this study by calculating defect energies for Sb^{3+}, Sb^{5+}, Sn^{2+} and Sn^{4+} as well as an oxygen vacancy, and their corresponding defect clusters. Surface energies for SnO_2 were then calculated and successfully compared to the work of

Mullheran and Harding [188]. Segregation energies were calculated for each defect complex by comparing bulk defect energies with those on the surface.

In attempt to improve upon the Langmuir - McLean method (LM), utilized in aforementioned studies [181, 182] to determine segregation trends, Srolovitz *et al.* have used the atomistic simulation type methods (LM) to describe atomic interactions and combined it with a minimization of free energy [189, 190]. Several limitations of the LM method are cited by Srolovitz *et al.* as the reason for employing free energy minimization. These limitations include: the inability to account for surface concentration, neglect of the finite extent of segregation (i.e. not just at the surface), inaccurate emphasis on solute misfit as well as the lack of accounting for vibrational contributions. The free energy minimization technique used by Srolovitz *et al.* combines interionic pair potentials with a local harmonic approximation of lattice dynamics [190] and a mean-field effective atom representation of solute concentrations [191]. Srolovitz *et al.* have used this technique to calculate the segregation of Ca^{2+}, Mn^{2+} and Sr^{2+} to the (001) and (011) surfaces of CaO, MnO and SrO. Each of these oxides was doped with Co, Fe and Ni. Despite a different approach, the results of Srolovitz were found to be in agreement with both LM and Monte Carlo methods [189]. The agreement with LM methods suggested to the authors that vibrational effects are of only limited importance in determining the segregation to free surfaces, thereby supporting the assumption of Cotter *et al.* [183].

4.3 Surfaces of UO_2

The three stable, lowest index surfaces of UO_2, as defined by Miller indices, are the (110), (111) and (100). Recalling the Tasker classification of surfaces described in Chapter 1, the (110) surface is a neutral Type 1 surface and therefore has no surface normal dipole to account for. The anion terminated (111) surface has charged

hybrid was also recently seen in MD simulations of the (100) surface of CaF_2 [192]. In this case, the (100) surface was simulated by using a single cluster of 3645 ions bounded by (111) and (100) surfaces. The (100) surface sizes were equivalent to an array of 3x3 single cells. After equilibrating for 10ns at 300K, the (100) surface consisted of an intergrowth of type A and type AB surfaces.

As the A, B and AB were found to be the lowest energy surfaces, they are the three that are considered in this segregation study. However, for segregation calculations, a 3x3 unit cell size has been employed as opposed to 2x2, in order to reduce defect - defect interactions between adjacent period boundary images. A 3x3 repeat unit clearly leads to many more surface configurations than the 153 considered by Abramowski. To be sure, the number of ways to configure the surface oxygen ions in a 3x3 cell size has not yet been calculated (although, without symmetry the number of configurations is greater than $9x10^9$). It is an assumption of this work that the three (100) surface configurations utilized remain the low energy surfaces with the larger surface repeat unit size. However, when the AB surface consisting of 3x3 cells is repeated, rather than a strictly AB surface (as would be the case if the repeat cell was 2x2), an intergrowth of AB and B is obtained. This intergrowth is analogous to that observed in CaF_2 and is therefore considered in this work.

Previous surface studies have been concerned with equilibrium morphology and stability of various crystallites. Those of particular relevance were conducted on stoichiometric CeO_2 [137] and UO_2 [45]. Both of these oxides crystallize in the fluorite structure, as mentioned in Chapter 1. These studies are similar in methodology (atomistic simulation as described in Chapter 2) and employ the same computational code (MARVIN) as used in the work presented in this thesis. Both previous studies predict that the equilibrium morphologies of CeO_2 and UO_2 are dominated by the (111) face. However, if thermodynamic equilibrium is not reached, and mor-

phology is instead governed by growth (i.e. kinetics), other surfaces were shown to be of importance (e.g. (100)).

STM experiments which have been conducted on all three of the UO_2 surfaces considered in this work [193–196] show that the structure of UO_2 surfaces can be quite complex, and that it is not necessarily accurate to assume that a simple low energy (111) surface is always sufficient. Temperature and stoichiometry can have effects on the surface termination. For example, the (110) surface of stoichiometric UO_2 has been shown to be slightly defective, with missing rows of surface atoms along the $[1\bar{1}0]$ direction [196]. However, the (110) surface of hyper-stoichiometric UO_{2+x} has been shown to be different than the stoichiometric surface. Muggelberg *et al.* suggest the formation of dimer pairs on the hyper-stoichiometric (110) surface to be the initial stages of U-O superstructure formation, as described by Campbell *et al.* [197]. The formation of this superstructure is suggested to be a function of temperature and extent of non-stoichiometry. Nevertheless, in the STM experiments, it was not clear if equilibrium had been established.

It should be noted that in this thesis, a stoichiometric material is assumed, and as such, the results are not applicable to non-stoichiometric $UO_{2\pm x}$, though it is noted that the investigation of the superstructure surfaces inherent to non-stoichiometric $UO_{2\pm x}$ as described above is worthwhile.

4.4 Methodology

In this work, three types of segregating species are investigated, categorized by their charge state. Ce^{4+} and Zr^{4+} are of the same charge state as U^{4+}, and therefore simply substitute for U^{4+}. This is in concert with previous calculations [36], which have determined the low energy solution site for Ce^{4+} and Zr^{4+} in stoichiometric UO_2 to be a uranium vacancy. Ba^{2+} and Sr^{2+} are also considered to substitute for

U^{4+}, but since they also substitute at uranium sites, the dissimilar charge needs to be compensated by an oxygen vacancy. Again, when compared to previous solution site calculations, the uranium/oxygen divacancy is a competitive site. Unfortunately, since it uses a supercell repeat methodology, MARVIN is unable to account for charged defects, and therefore, it was not possible to consider isolated charged solution sites. Finally, zero-valent Kr^o and Xe^o substitute for U^{4+}, but need to be charge compensated by two oxygen vacancies. As discussed in Chapter 3, the neutral tri-vacancy is the low energy solution site for these fission products.

Since these calculations are not dynamical in nature, it is necessary to develop a strategy to determine segregation trends from available data. This study investigates the effect of surface relaxation on segregation. As such, a characteristic repeat unit is defined. To determine segregation trends, each of these fission product defects is introduced into the bulk, where a calculation is performed to determine its energy. The defect is then systematically moved stepwise to the surface, where a calculation is performed at each layer (see Figure 4.2). These energies are then compared to one another and plotted as a function of depth. By means of relative energies, this approximately describes the chemical potential, which is the driving force for segregation. It is important to note that the energies used to determine and discuss segregation trends are *relative*.

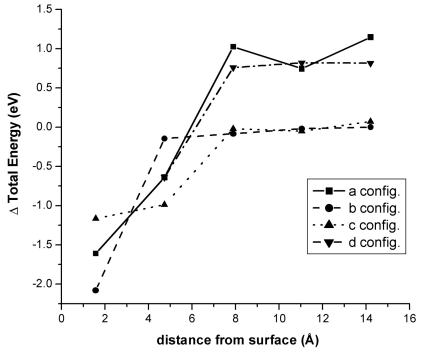

(a) 1x1x6

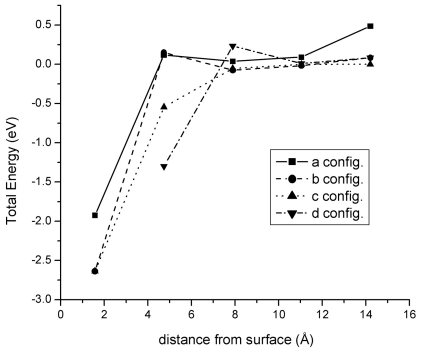

(b) 2x2x6

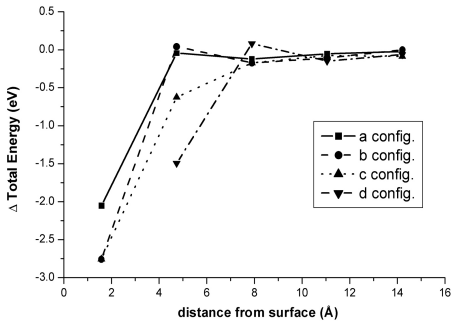

(c) 3x3x9

Figure 4.3: The calculated relative energies of $\{(Ba_U)'':(V_O)^{\cdot\cdot}\}$ as a function of depth from the (111) surface using 1x1x6, 2x2x6 and 3x3x9 simulation cells respectively. As the simulation cell increases in size, the unphysical defect - defect interaction is reduced.

To reduce the defect-defect interactions, larger simulation cells were used. The 2x2x6 simulation cell in Figure 4.3(b) was also found to be unsatisfactorily small. Therefore, a 3x3x9 unit cell simulation block was employed, see Figure 4.3(c). There are several reasons to use a simulation block of this size. First, some evidence

of horizontal defect - defect interaction remains in Figure 4.3(b) (though greatly reduced). Second, in some results (to follow), cluster configuration effects were still evident at depths greater than 6 unit cells (see next section). Results for each of the two larger cell sizes are compared to the 1x1x6 cell size in Figure 4.3. It is clear that by using a repeat cell of 3x3x9 unit cells, the total defect energies have converged with respect to cell size. The results which follow are denoted with the simulation cell size that was used.

4.4.1 Orientation of Fission Product Defect Clusters

In Chapter 3, the concept of low energy solution site was introduced in regard to defect clusters. For example, in these segregation calculations Ba and Sr are considered as a constituent of a defect cluster which also consists of a single oxygen vacancy and single uranium vacancy (where the divalent ion resides). This cluster is configured such that the oxygen vacancy is in a nearest neighbour position with respect to the Ba or Sr atom, as it was calculated to have a lower energy than other defect clusters [36]. This preference was determined by calculating the binding energy of the cluster, where binding energy is defined as:

$$BE_{\text{cluster}} = \left[\sum_{\text{components}} E_{\text{defect}} \right] - E_{\text{cluster}} \tag{4.1}$$

Binding energies are calculated by systematically moving the oxygen vacancy in question (namely, in Kröger-Vink notation $(\mathrm{V_O})^{\cdot\cdot}\}$) away from the Ba or Sr at the uranium site (i.e. $\{(\mathrm{Me_U})''$) one atomic position at a time and calculating the defect energy at each step. A positive binding energy indicates a preference for the defects to form a cluster rather than to remain isolated. From Figure 4.4, it is clear that the nearest neighbour configuration is preferred.

Comparison of segregation trends is also facilitated by a second energy, E_T, which is defined as the difference between the energy of the fission product at the surface and the energy of the fission product in its most stable position, often just beneath the surface. In this regard, Zr^{4+} behaves slightly different than Ce^{4+}. For Zr^{4+}, $E_T^{Zr} = 0.352$eV, which is considerably greater than E_S, suggesting that Zr^{4+} will not segregate to the (111) surface, but will remain trapped just below the surface. This trap is not evident for Ce^{4+}, with E_T^{Ce} - $E_S^{Ce} = 0.004$eV. It is likely that the disparity in ionic radii between U^{4+} and Zr^{4+} (0.89 vs. 0.72 Å respectively) gives rise to the subsurface trapping phenomenon, while the similarity in ionic radius between U^{4+} and Ce^{4+} (0.89 vs. 0.87 Å respectively [6]) may explain the lack of trapping.

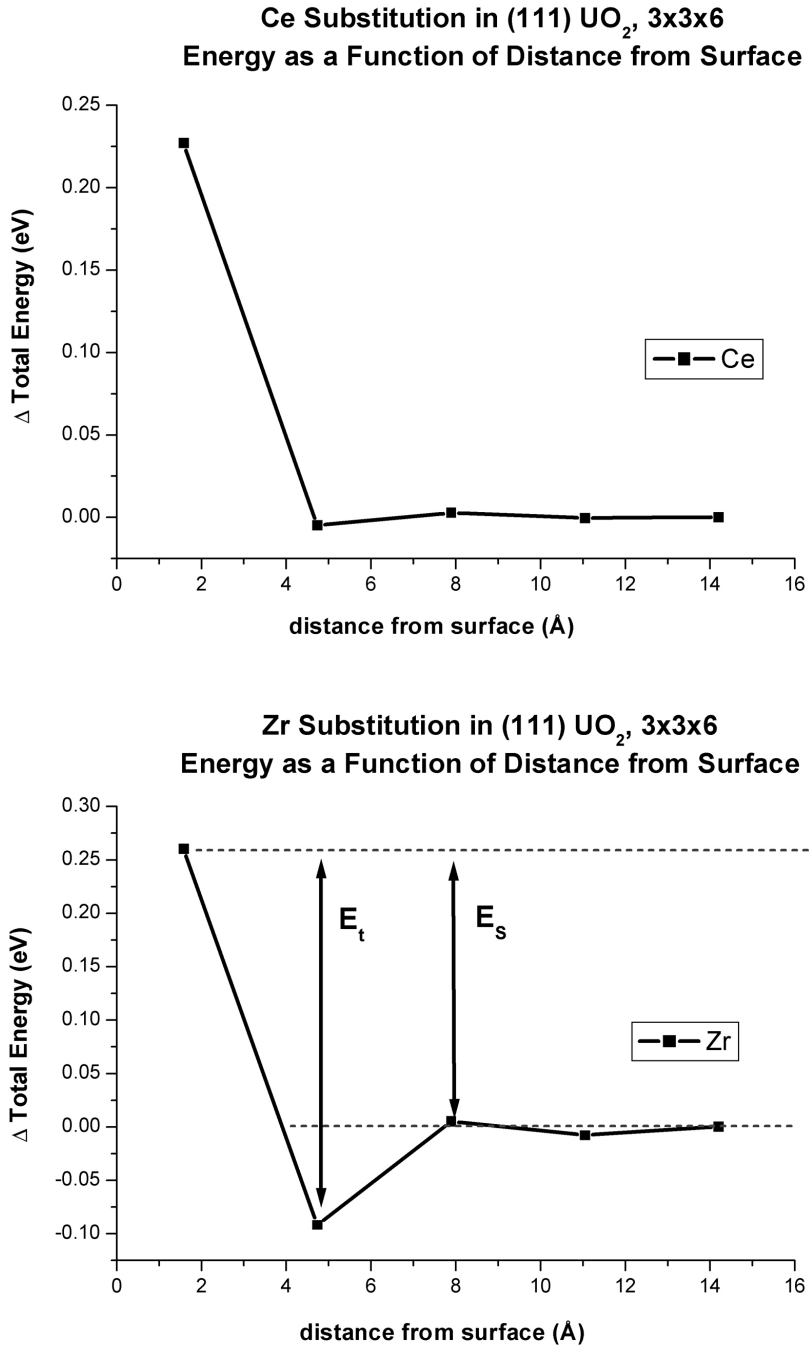

Figure 4.10: The calculated relative energies of $(Ce_U/Zr_U)^{''''}$ as a function of depth from the (111) surface, where E_T is the trap energy and E_S is the segregation energy.

It should be noted that the manner in which segregation trends are calculated in this work differs from the method of Slater *et al.* [187] as discussed in Section 4.2.2. In their work, Slater *et al.* define E_S as the difference between the energy of a defect in the bulk and at the surface. Srolovitz *et al.*, as previously mentioned in Section 4.2.2, make note of this limitation of the Langmuir - McLean analysis, citing that segregation to subsurface layers is appreciable. The methodology of this work (i.e. performing a calculation at each atomic layer, from the surface to the bulk), describes the segregation behaviour at each atomic layer, rather than only comparing the surface to the bulk. Nevertheless, this is still only part of the complete picture as kinetic barriers to migration of fission products to surfaces are not considered.

In Figure 4.11, it is clear that there is a pronounced driving force for both Ba^{2+} and Sr^{2+} to segregate to the (111) surface of UO_2. The segregation energies for Ba^{2+} and Sr^{2+} are E_S^{Ba} = -2.706eV and E_S^{Sr} = -1.603eV respectively. Clearly, the driving force for Ba^{2+} to segregate is greater than for Sr^{2+}. Again, this disparity in E_S can be attributed to ionic radius mismatch. The ionic radius for Sr^{2+} (1.18Å) is more similar to U^{4+} (0.89Å) than is the radius for Ba^{2+} (1.35Å).

Figure 4.11 also shows that within the bulk (i.e. >11Å from the surface) there is practically no preference between the cluster configurations. Conversely, nearer to the surface, it appears that there is a cluster configuration dependence. This behaviour is a consequence of how the strain field induced by the cluster interacts with the strain field induced by the surface (i.e. a competition between the relaxation modes).

Simulations involving Xe and Kr proved to be very difficult and only preliminary results were obtained. These are presented in Figure 4.12. The complexity of the Schottky trio made calculations of this type difficult. More calculations are needed in order to make a more reliable and systematic statement. However, the indication from Figure 4.12 is that Kr does not segregate to the (111) surface. It is even more difficult to make a statement about Xe segregation from Figure 4.12. Nevertheless, it appears that for the (a) configuration, there is a segregation barrier. However, calculations for the (b) and (c) configurations have not been completed to the extent that an argument for or against segregation can be made.

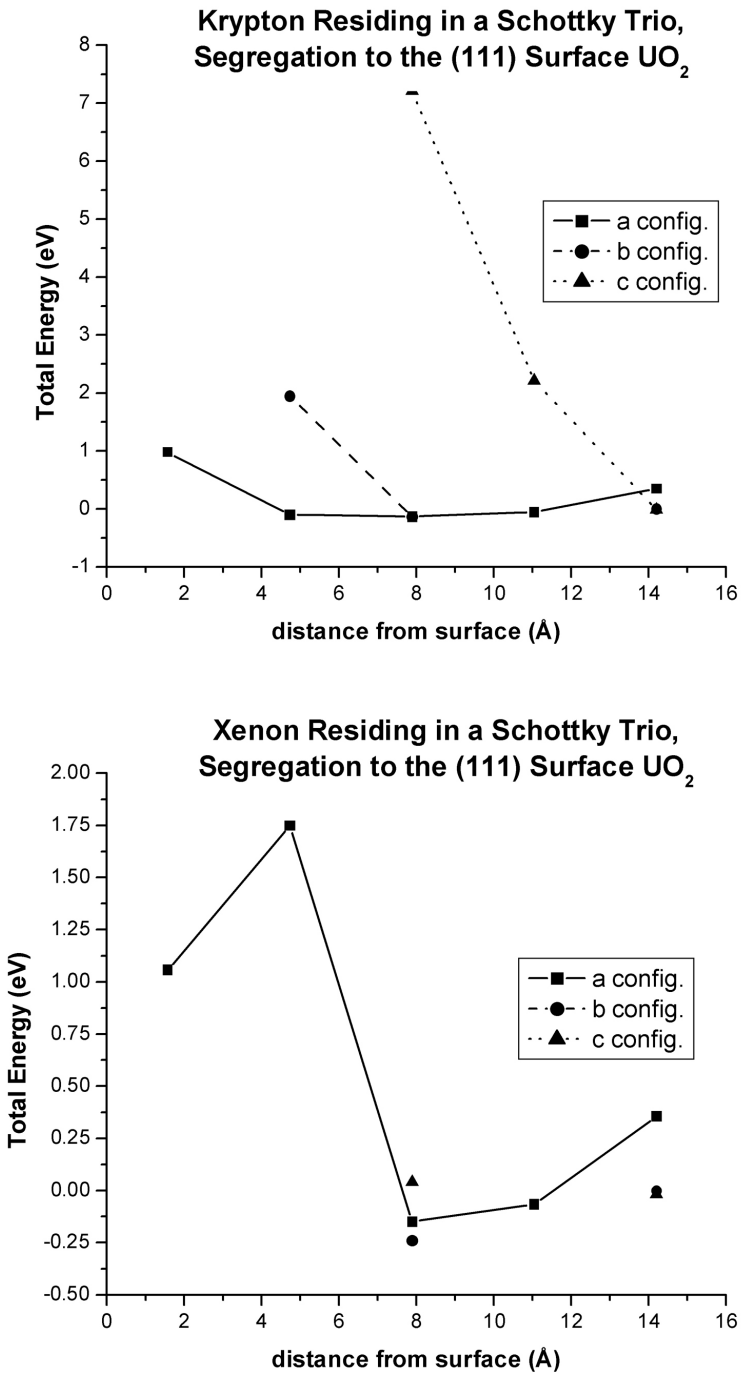

Figure 4.12: The calculated relative energies of $\{(V_O)^{\cdot\cdot}:(Kr_U/Xe_U)^{''''}:(V_O)^{\cdot\cdot}\}$ as a function of depth from the (111) surface.

Another apparent problem with this simulation is that in the bulk, the different cluster configurations do not have the same energy. As previously mentioned, this is because the cluster is approaching the Region I - Region II boundary. Thus, the cluster causes a distortion to the lattice that cannot be propagated into Region II, and therefore, the energy can only be partly minimized. Since the oxygen vacancies associated with the different orientations are at different distances from the Region I - Region II boundary, this causes the different orientations to have different energies.

The position of the fission product relative to the Region I - Region II boundary will also have an effect on the total polarization energy of the lattice. That is, a fission product at the centre of Region I will polarize Region I to a greater extent than if it is at the Region I - Region II boundary. This is again because Region II is not polarizable. This limitation manifests itself in an unphysical effect where as the fission product moves from the boundary into Region I, the polarization energy increases (before the effect of the surface is encountered). Fortunately, such an effect seems negligible in the results on UO_2 presented here (however, it is more apparent in the results on ZrO_2 presented in the Appendix).

4.5.2 The (110) Surface

There are similarities between the two plots in Figure 4.13, the most obvious being that the trends predict the same tendency for Ce^{4+} and Zr^{4+} to not segregate to the (110) surface, as was the case with the (111) surface. Upon closer inspection, it is clear that the segregation energy barrier for Ce^{2+} is greater than that of Zr^{4+}, where $E_S^{Ce} = 0.667$eV and $E_S^{Zr} = 0.132$eV. These energies should be compared to those obtained for the (111) surface (i.e. 0.232eV and 0.261eV for Ce^{4+} and Zr^{4+} respectively). Thus, the segregation barrier for Ce^{4+} is 0.435eV larger for the (110) than for the (111) surface, while the segregation barrier for Zr^{4+} is 0.099eV smaller.

Regardless, both segregation energies are positive, consistent with suggesting no Ce^{4+} or Zr^{4+} segregation to the (110) surface. Also, the energy of Ce^{4+} within the bulk appears to vary more smoothly than Zr^{4+}. This can again be attributed to the similarity in size between Ce^{4+} and U^{4+}, compared to U^{4+}. Consequently, the alternate compression and dilation of atomic layers which characterizes the (110) surface of the fluorite structure [44] has a greater effect on the relative energies of Zr^{4+} than on Ce^{4+}.

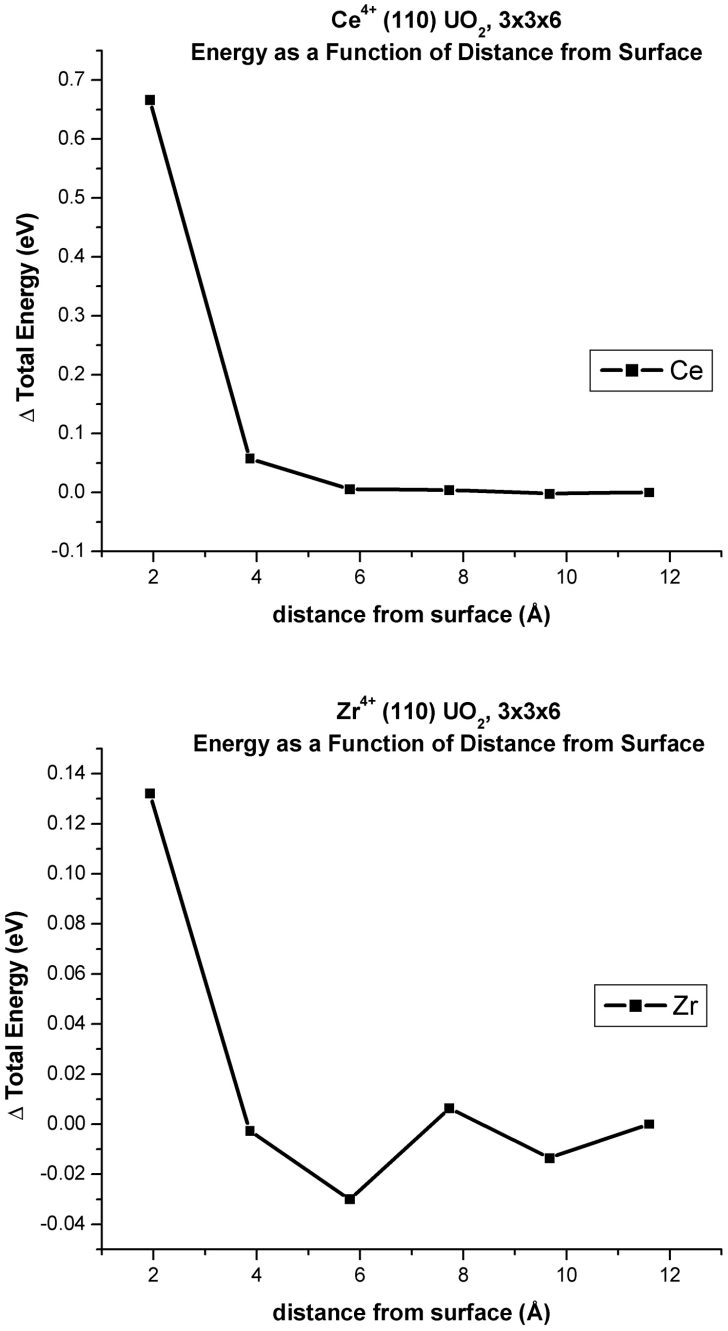

Figure 4.13: The calculated relative energies of $(Ce_U/Zr_U)^{''''}$ as a function of depth from the (110) surface.

Figure 4.14 presents the results for Ba^{2+} and Sr^{2+} segregation to the (110) surface. It is clear that both fission products tend to segregate to this surface, as was the case for the (111) surface. Also evident in Figure 4.14 is that E_S^{Ba} is considerably more negative than E_S^{Sr}, suggesting a stronger tendency for Ba^{2+} to segregate than Sr^{2+}. An interesting comparison can be made between the segregation energies of both species to the (110) and (111) surfaces. The energy of segregation, E_S, for both Ba^{2+} and Sr^{2+} to these two surfaces is very similar: E_S^{Ba} = -2.695eV for the (110) and = -2.706eV for the (111); E_S^{Sr} = -1.604eV for the (110) and = -1.603eV for the (111).

Another interesting comparison between Ba^{2+} and Sr^{2+} segregation to the (111) and (110) surfaces is that the fall in energy (and thus the driving force for segregation) begins between 6 and 8Å from the (110) surface, but between 4 and 6Å for the (111) surface. Consequently, it might be expected that a greater amount of Ba^{2+} or Sr^{2+} will be adjacent to the (110) surface than the (111) surface, despite the similarity in segregation energies, E_S.

4.5.3 The (100) Surface

Figure 4.15 depicts the results for Ce^{4+} and Zr^{4+} segregation to each of the three anion terminations described in Section 4.3 for the (100) surface. The top image in Figure 4.15 describes the segregation trends of Ce^{4+}. What is interesting about this plot, is that the segregation energies for each anion termination are different: -0.1221eV, 0.3292eV and 0.098eV for the A, B and AB terminations respectively. Although these are not large energies, it is evident that segregation is a function of the configuration of the anion terminations for polar surfaces. This effect is again evident in the bottom plot in Figure 4.15, describing the segregation trend of Zr^{4+} to the three anion terminations of the (100) surface. Unfortunately, this plot is less compelling as the two energies of the defect near the (100)AB would not successfully minimize. However, what can be seen is that for the (100)A and (100)B surfaces, there is a significant negative segregation energy: -0.7495 and -0.9141 respectively. This suggests that Zr^{4+} will segregate to these two surfaces.

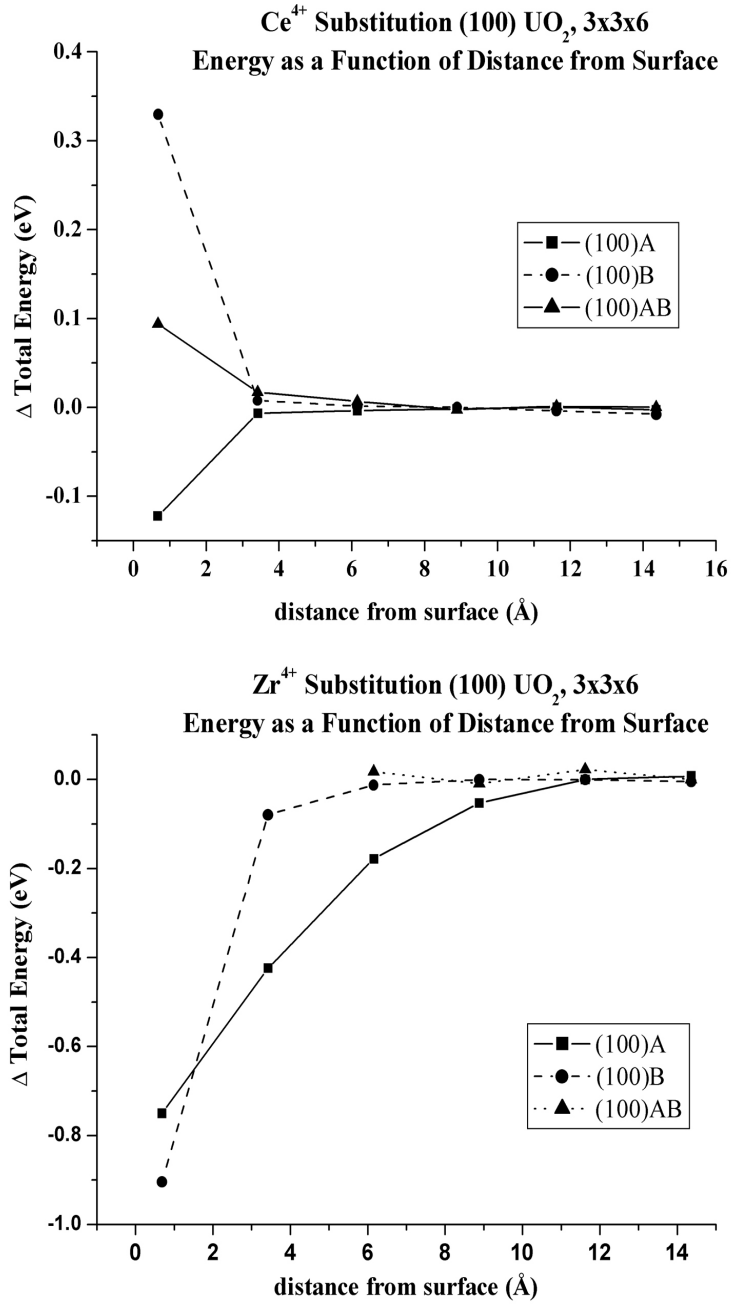

Figure 4.15: The calculated relative energies of the $\{(Ba/Sr_U)'':(V_O)^{\cdot\cdot}\}$ defect cluster as a function of depth from the three anion terminations of the (100) surface.

When comparing Figure 4.15 with Figures 4.10 and 4.13, the segregation trends for Ce^{4+} and Zr^{4+} to the three surfaces are clearly different. For both Ce^{4+} and Zr^{4+}, the trend to segregate to the (100)A surface is opposite that calculated for the (111) and (110).

Figure 4.16 shows the results for Ba^{2+} and Sr^{2+} segregation to the (100)A surface. Immediately, when comparing Figure 4.16 with Figures 4.11 and 4.14, clear differences are apparent. Although the segregation energies for Ba^{2+} and Sr^{2+} are again negative (E_S^{Ba} = -4.8527eV and E_S^{Sr} = -3.2844eV), suggesting that these fission products will segregate to this surface, the profile of the energy from the bulk to the surface is different than observed for the previous two surfaces. In both cases, the"c." cluster configuration steadily decreases in energy as it moves to the surface, while the other three configurations decrease in energy more abruptly near the surface. Also in both cases, the "a." configuration is of lower energy throughout the segregation profile than the "b." and "d." configurations. Referring back to Figure 4.7, both the "a." and "c." configurations lie underneath a surface oxygen, while the "b." and "d." configurations lie underneath a surface vacancy. This may contribute to the lower energy. It should also be noted that the segregation energies are substantially more negative than for the previous two surfaces. Again, E_S^{Ba} is more negative than E_S^{Sr}, which can be attributed to size of these ions, as was the case for the previous two surfaces.

Calculations which determine the segregation trends to the (100)B and (100)AB have not yet been successful.

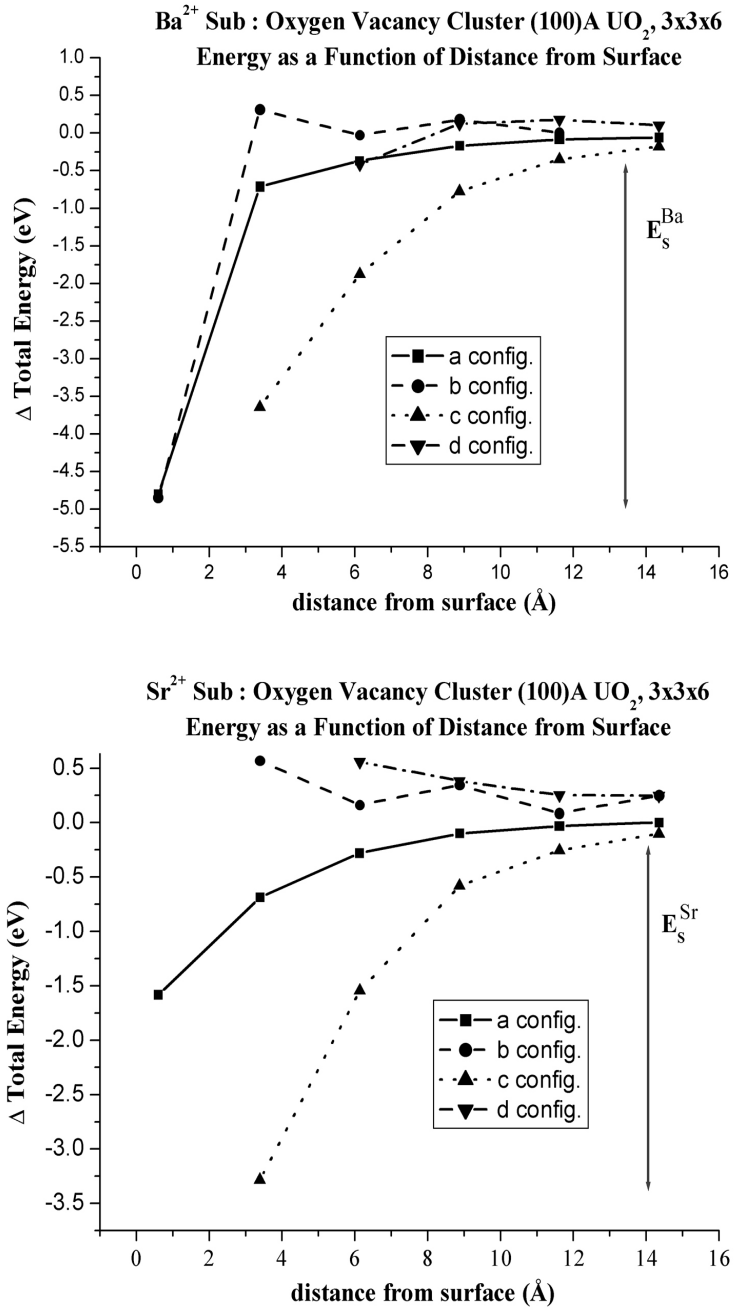

Figure 4.16: The calculated relative energies of the $\{(Ba_U/Sr_U)'':(V_O)^{\cdot\cdot}\}$ defect cluster as a function of depth from the (100)A surface, where E_S is the segregation energy.

4.6 Conclusions

The manner in which the segregation energy, E_S, of a given fission product varies between surface types has been demonstrated. Furthermore, E_S has been shown to be a strong function of defect cluster configuration with respect to surface as well as anion termination of the polar (100) surface. These results suggest that release of fission products from grains of UO_2 in nuclear fuel will not be isotropic. Consequently, the distributions of surface types will influence fission product release. This is particularly important when it is considered that surface types will change due to grain growth *in situ* as a function of burn-up. As fission product release is a limiting factor in fuel performance, these results suggest that release may be controlled to an extent through surface modification.

Qualitative comparison can be made to the work of Sato *et al.* [198]. In this work, Sato *et al.* investigated the behaviour of Ba and Zr in fuel specimens irradiated up to burnups of 13.3at% at the experimental fast reactor of the Japanese Nuclear Cycle Development Institute. Although the samples studied were polycrystalline, and the surfaces were not analyzed, it might be deduced that these samples were predominantly consisting of low energy surfaces (i.e. (111) and (100)). Using X-ray micro scanning and X-ray micro analysis to determine radial distributions of Ba and Zr, Sato *et al.* found Ba concentrations to increase in the radial direction, while the Zr concentration remained homogenous in the radial direction. This observation suggested to the authors that Ba easily migrates, while Zr remains in the fuel [198]. If the predominant surface of the fuel is assumed to be the (111) surface, the positive segregation energies calculated for these two species to these two surfaces suggest that the calculations presented in this chapter preliminarily account for this phenomenon, although much more analysis is required.

More calculations are need in order to formulate a systematic statement about

fission product segregation behaviour. At the time these calculations were made, the complexity and size was at the limit of computing resources. As this technology improves, these calculations will become possible. Nevertheless, this chapter clearly shows that the phenomenon of fission product segregation is quite complicated.

Chapter 5

Non-Stoichiometry in $A_2B_2O_7$ Pyrochlores

"So he thinks that they hold on to one another and remain together up to the time when some stronger force reaches them from their environment and shakes them and scatters them apart."

- Aristotle

On Democritus, c.350 BC

5.1 Introduction

Due to the extensive compositional range of the compounds which exhibit the pyrochlore structure, there are a variety of actual and potential applications for these materials. Examples include: dielectric materials [199, 200], catalysts [201, 202], solid electrolytes [203–205], thermal barrier coatings [206, 207] as well as actinide host phases for nuclear waste encapsulation [208–211]. Given this broad range of functionality, in order to tailor pyrochlore properties it is desirable to understand

their non-stoichiometry in a consistent manner.

Here, the $A_2B_2O_7$ pyrochlores in which A is strictly a 3+ cation and B a 4+ cation are considered (refer to Chapter 1 for a detailed description of pyrochlore crystallography). Our aim is to predict the mechanisms that accommodate non-stoichiometry and thereby provide data that can be evaluated against A_2O_3-BO_2 binary phase diagrams. As such, 4+ cations are not allowed to exhibit variable charge states, despite the fact that cations such as Ti, Ru, Mo and Pb are able to exhibit a 3+ charge state. If 3+ charge states were included for the B cations, the appropriate comparison would be to ternary A_2O_3-BO_2-B_2O_3 phase diagrams, none of which have been found in the literature (although ternary phase diagrams do exist for certain A_2O_3-BO_2-$A\prime_2O_3$ combinations, such as HfO_2 - Y_2O_3 - Er_2O_3 and HfO_2 - Y_2O_3 - La_2O_3 [212, 213]). Similarly, the possibility that Pr^{3+} may be oxidized to a 4+ charge state is not considered (Note: Ce^{3+} and Tb^{3+} may also exhibit a 4+ charge state although these cations are not explicitly modelled).

5.1.1 Review of Phase Diagrams

Existing experimental work relating to non-stoichiometry has focused exclusively on determining phase diagrams. Of the pyrochlores modelled explicitly in this study, there exist selected phase diagrams that include compounds in the series $A_2Ti_2O_7$ and $A_2Zr_2O_7$. The titanate pyrochlores $Lu_2Ti_2O_7$, $Yb_2Ti_2O_7$, $Dy_2Ti_2O_7$, $Sm_2Ti_2O_7$, $Nd_2Ti_2O_7$ and $La_2Ti_2O_7$ exhibit stability in the form of a line compound [214–218]. In all of the corresponding phase diagrams, pyrochlores are reported between 900^o - 2000^oC, see for example Figure 5.1.

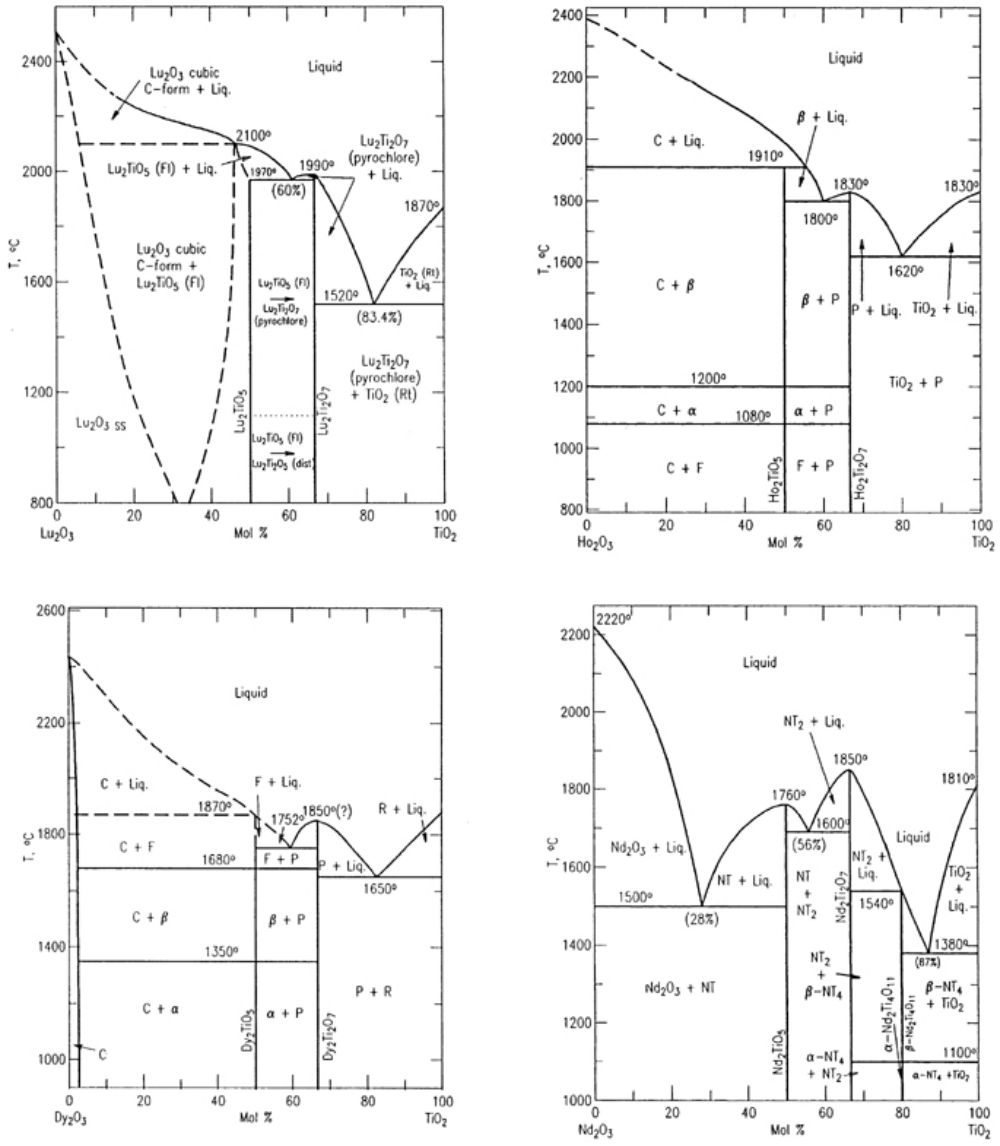

Figure 5.1: Phase diagrams of the $A_2Ti_2O_7$ series of compounds for small A^{3+} cations, reproduced from [214, 215, 217].

However, there exist several other titanate phase diagrams (e.g. $Dy_2Ti_2O_7$, $Er_2Ti_2O_7$, $Sm_2Ti_2O_7$ and $Y_2Ti_2O_7$ [219–222]) which demonstrate modest non-stoichiometry. An example of this is shown in Figure 5.2, where there is an extended pyrochlore phase field in the Y_2O_3 -TiO_2 system. The dashed line between the fluorite and

pyrochlore phase regions is an undetermined boundary, as the investigators were unable to establish the two phase region.

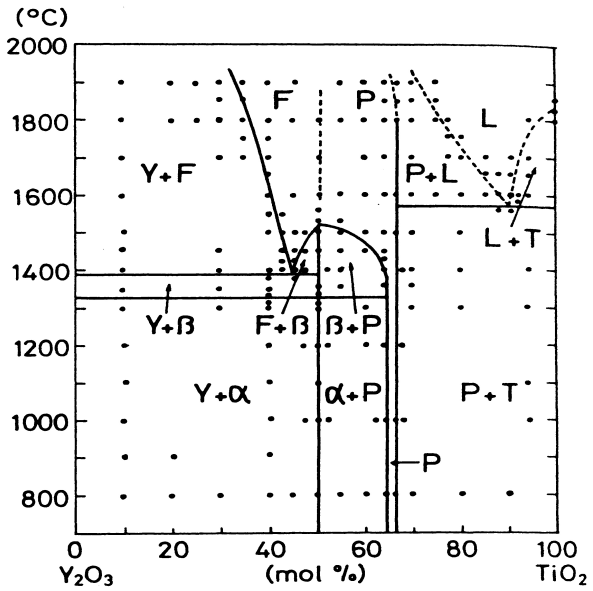

Figure 5.2: The phase diagram of the Y_2O_3 -TiO_2 system, reproduced from [222].

An interesting comparison of phase diagrams is provided by two in the Sm_2O_3 - TiO_2 system, shown in Figure 5.3. Clearly, there are glaring differences between these two phase diagrams, especially in the region of the pyrochlore phase. Such inconsistency in the titanate series of phase diagrams does not lend itself to quantitative comparison with our calculations, though the qualitative information is useful.

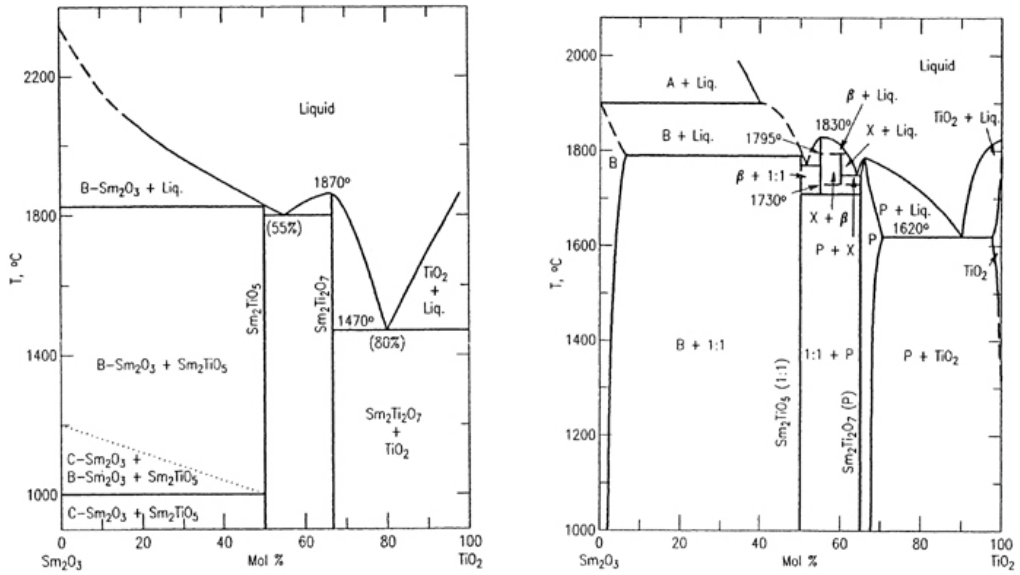

Figure 5.3: Comparison of Sm_2O_3 - TiO_2 phase diagrams, where the pyrochlore phase in the left diagram is a line compound while in the right hand diagram exhibits modest non-stoichiometry; reproduced from [216] and [221], respectively.

There are several potentially pertinent phase diagrams within the zirconate series. However, in those diagrams the pyrochlore phase regime is usually extrapolated. Figure 5.4 depicts such hypothetical pyrochlore phase regions for $Eu_2Zr_2O_7$, $Gd_2Zr_2O_7$ and $Sm_2Zr_2O_7$ [223–225]. Furthermore, the bottom two phase diagrams in Figure 5.4 both describe the Sm_2O_3 - ZrO_2 system, albeit differently. Nevertheless, these diagrams suggest that zirconates will exhibit both BO_2 and A_2O_3 non-stoichiometry.

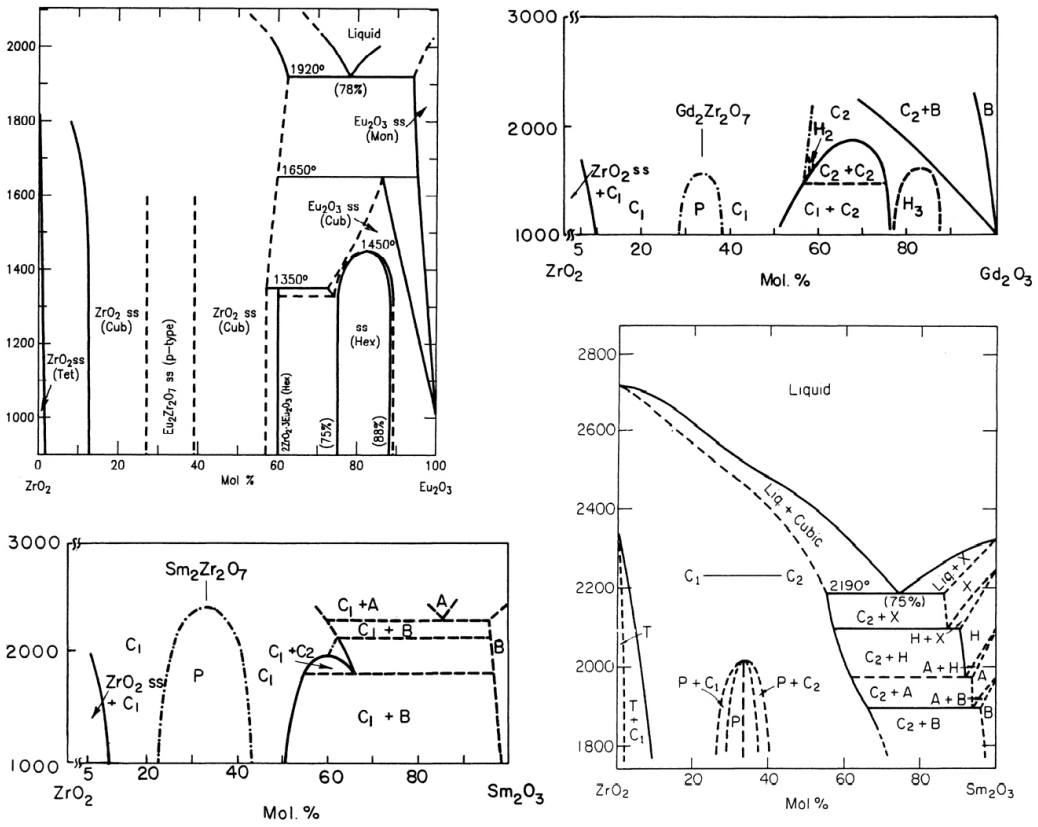

Figure 5.4: Comparison of Eu_2O_3 - ZrO_2, Gd_2O_3 - ZrO_2 and Sm_2O_3 - ZrO_2 phase diagrams, where the pyrochlore region in each diagram is hypothesized; reproduced from [223–225].

A singular exception from the hypothesized pyrochlore phase region is in the La_2O_3 - ZrO_2 system [224, 225], in which the pyrochlore regime is well defined, see the top two phase diagrams in Figure 5.5. However, substantial differences exist between these two reported La_2O_3 - ZrO_2 phase diagrams. These two diagrams can be compared to three phase diagrams of the same system, shown in the bottom of Figure 5.5. Although the three diagrams display probable phase regions, when compared to the two phase diagrams above, it is clear that this system is not very well understood.

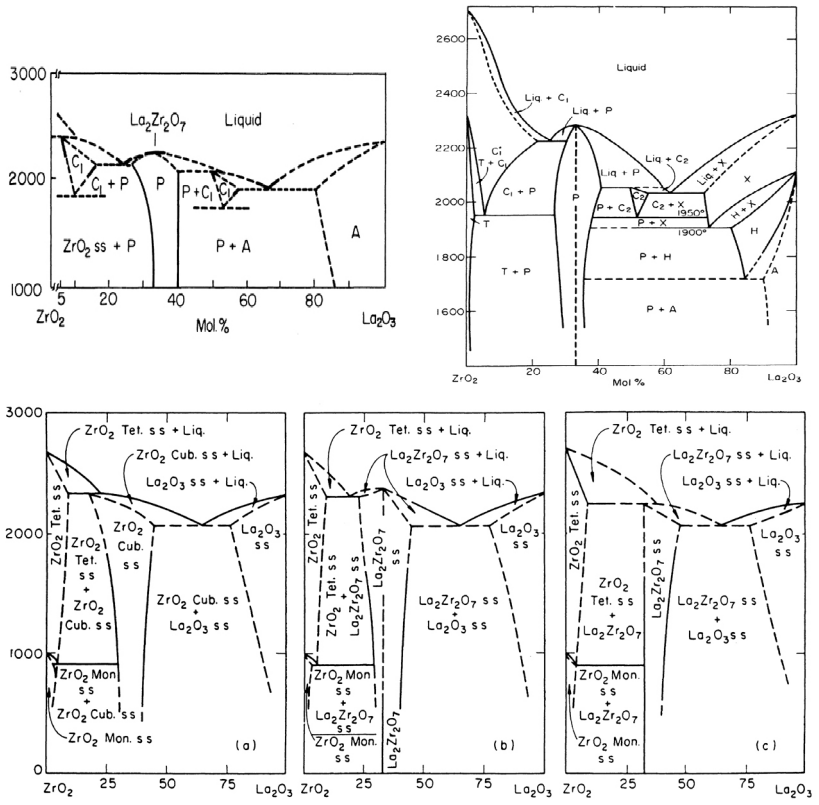

Figure 5.5: Several La_2O_3 - ZrO_2 phase diagrams, reproduced from [224], [225] and [226, 227] respectively.

Returning to the zirconate phase diagrams with hypothesized pyrochlore regimes, for example the two describing the Nd_2O_3 - ZrO_2 series [225–227], there exist substantial differences, see Figure 5.6. Again, it is difficult to quantitatively compare our calculated results to these phase diagrams. However, what can be qualitatively noted from the zirconate series, when compared to the titanate series, is the increased extent of pyrochlore non-stoichiometry.

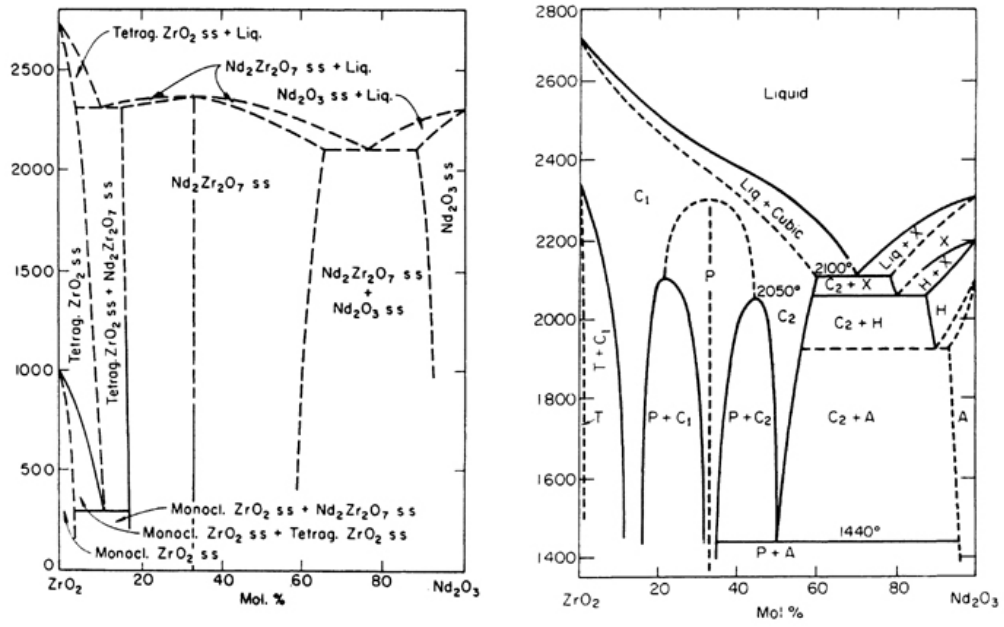

Figure 5.6: Comparison of Nd_2O_3 - ZrO_2 phase diagrams, reproduced from [226, 227] and [225] respectively.

There have been recent theoretical calculations of zirconate phase diagrams. Figure 5.7 depicts phase diagrams for the Y_2O_3 - ZrO_2 and La_2O_3 - ZrO_2 systems as calculated by Yokokawa *et al.* [228]. It is interesting to compare these two phase diagrams to those generated through experiment. The diagram on the right depicting the La_2O_3 - ZrO_2 system can be compared to Figure 5.5. In both the experimental and theoretical diagrams, a pyrochlore phase clearly exists. However, in the experimentally generated diagrams, there is pronounced non-stoichiometry, while for the theoretical, the pyrochlore phase appears only as a line compound.

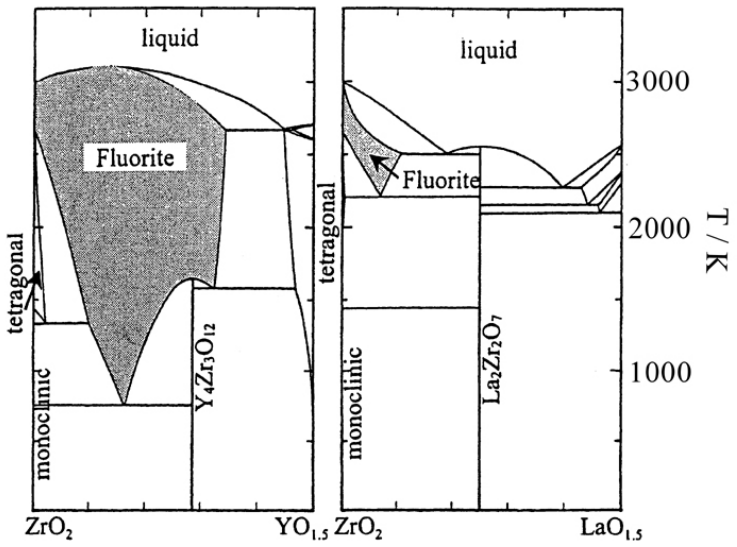

Figure 5.7: ZrO_2 - A_2O_3 phase diagrams calculated by Yokokawa *et al.* [228].

The left diagram in Figure 5.7 depicts the Y_2O_3 - ZrO_2 system. Due to the technological significance of this system, there has been considerable experimental effort in order to generate the phase diagram. Figure 5.8 displays a representative evolution of this phase diagram, reproduced from various sources [229–234]. The details of these phase diagrams are not pertinent here and can be found in the original texts, but it should be noted that in both the theoretical and experimental phase diagrams for the Y_2O_3 - ZrO_2 system, there is no indication of a $Y_2Zr_2O_7$ pyrochlore phase, although a $Y_4Zr_3O_{12}$ phase is reported.

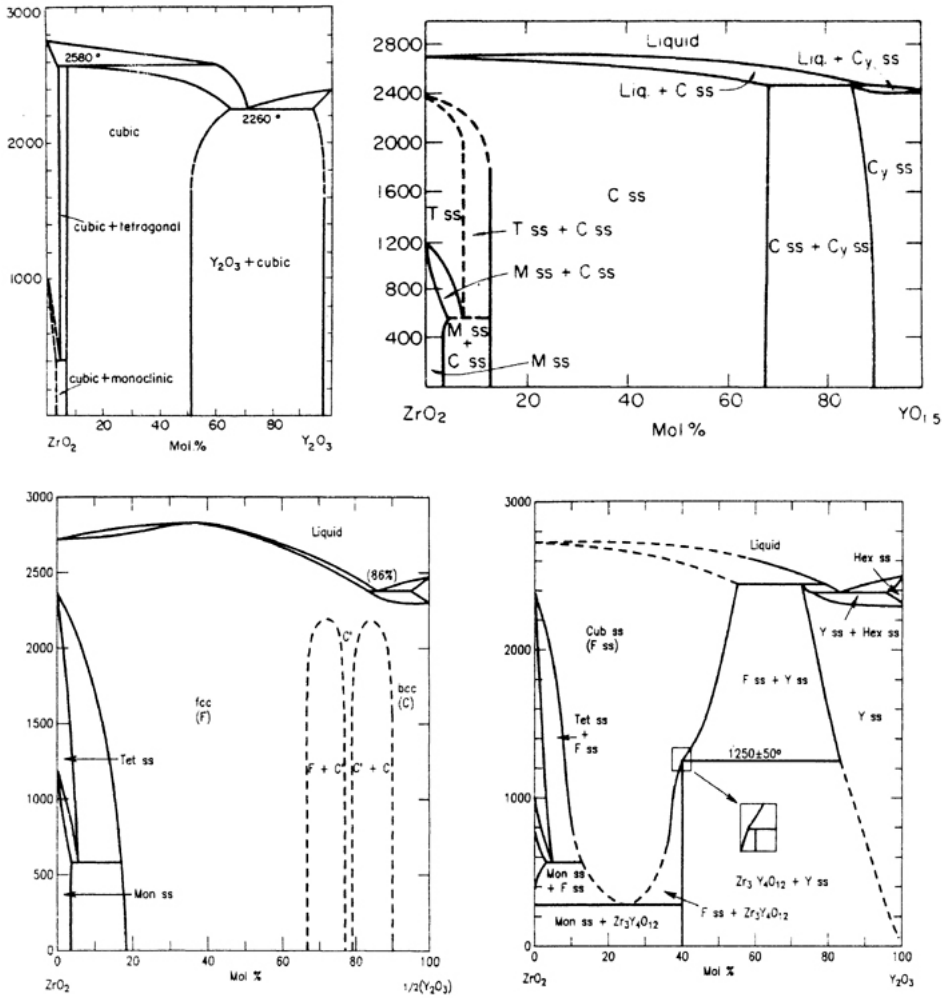

Figure 5.8: Experimental phase diagrams of the Y_2O_3 - ZrO_2 system, reproduced from [229] and [230] respectively for the top two diagrams and [231,232] and [233,234] respectively for the bottom two diagrams.

A more complete set of phase diagrams exists for the $A_2Hf_2O_7$ series of compounds, with pyrochlore phases reported between 1600^o - 2500^{o}C. Although hafnium has not been explicitly modelled, zirconium and tin were considered explicitly, and their ionic radii, 0.72Å and 0.69Å respectively [6], lie either side of hafnium, 0.71Å. Thus, the computational data for hafnium can be extrapolated and subsequently

can be compared to experimental data [235–238]. The hafnate phase diagrams show that the pyrochlore structure is stable from La^{3+} (1.16Å) to Tb^{3+} (1.04Å), but with no pyrochlore phase field apparent for the smaller A^{3+} cations from Dy^{3+} (1.027Å) to Lu^{3+} (0.977Å), see Figures 5.9 and 5.10.

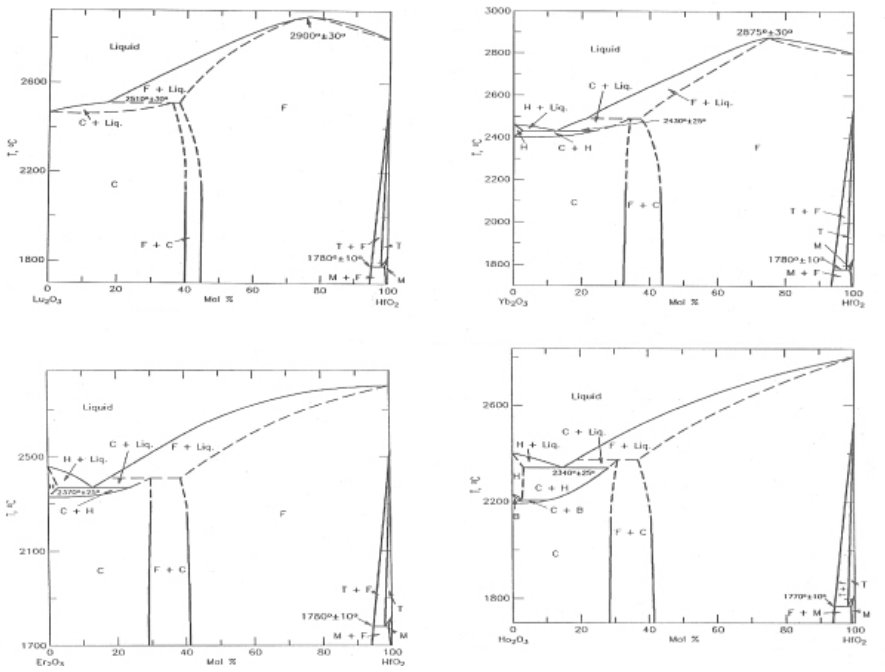

Figure 5.9: Phase diagrams of the $A_2Hf_2O_7$ series of compounds for small A^{3+}, reproduced from [235]. Here the A^{3+} cations have the ionic radii of Lu^{3+} = 0.977Å, Yb^{3+} = 0.985Å, Er^{3+} = 1.004Å and Ho^{3+} = 1.015Å.

The transition from the non-existence of a pyrochlore phase to the emergence of such a phase is depicted in Figure 5.10, with the Dy_2O_3 - HfO_2 system displaying no pyrochlore phase, while Tb_2O_3, Gd_2O_3 and Sm_2O_3 - HfO_2 do exhibit a pyrochlore phase. This transition will be revisited in Chapter 6. For now, the dependence of pyrochlore stability on A^{3+} cation radius is simply noted.

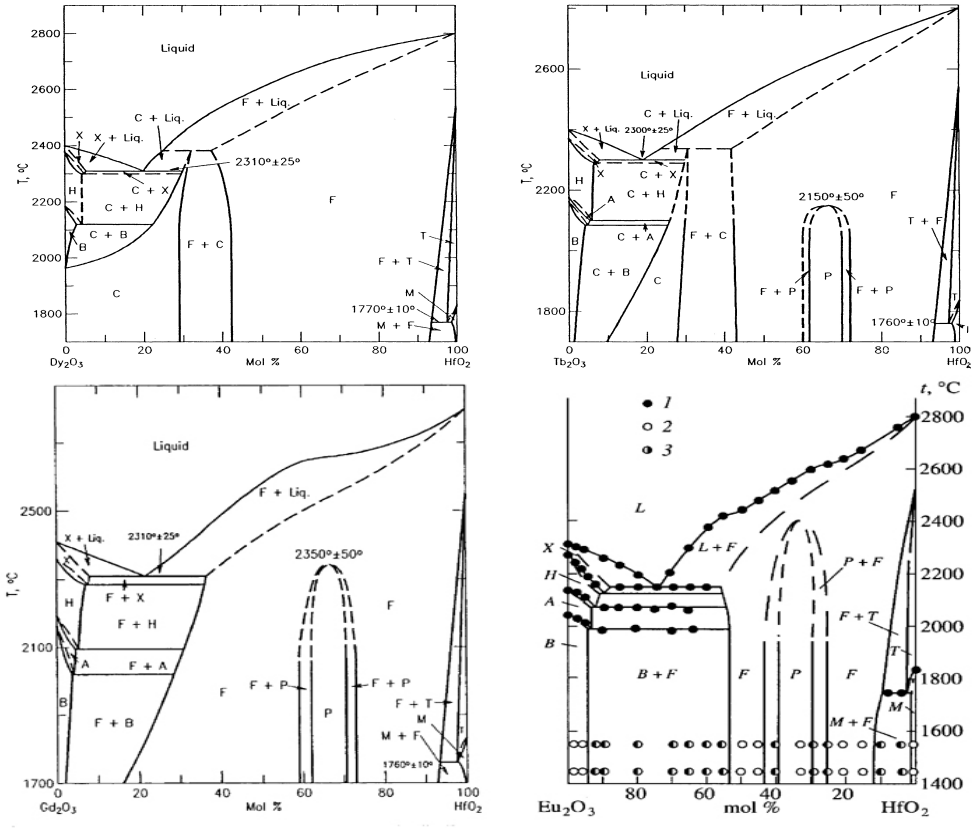

Figure 5.10: Phase diagrams of the $A_2Hf_2O_7$ series of compounds for intermediate A^{3+}, reproduced from [236, 237]. Here the A^{3+} cations have the ionic radii of Dy^{3+} = 1.027Å, Tb^{3+} = 1.04Å, Gd^{3+} = 1.053Å and Eu^{3+} = 1.066Å.

Of particular interest in the hafnate phase diagrams are the larger A^{3+} cations (i.e. Sm^{3+}, Nd^{3+}, Pr^{3+} and La^{3+}, shown in Figure 5.11). In particular, in all of these diagrams the BO_2 excess non-stoichiometry extends to approximately 70 mol percent BO_2. That is, the extent of non-stoichiometry is essentially constant as a function of increasing A cation radius. Conversely, there does seem to be some variation in A_2O_3 excess non-stoichiometry between compounds. This observation will be returned to in Section 5.3.4.

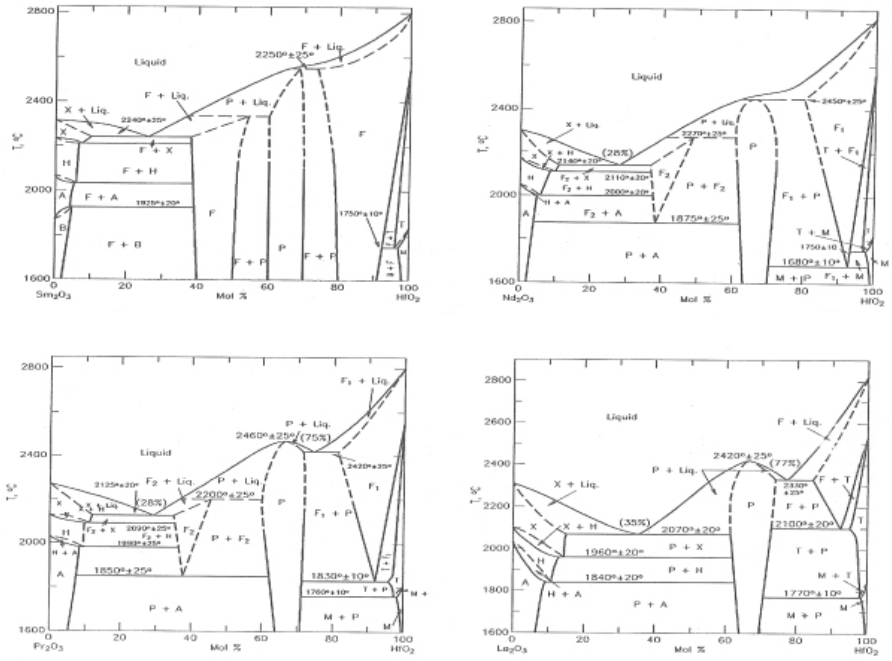

Figure 5.11: Phase diagrams of the $A_2Hf_2O_7$ series of compounds for large A^{3+}, reproduced from [238]. Here the A^{3+} cations have the ionic radii of $Sm^{3+} = 1.079$Å, $Nd^{3+} = 1.109$Å, $Pr^{3+} = 1.126$Å and $La^{3+} = 1.16$Å.

An advantage of the A_2O_3 - HfO_2 series of phase diagrams is that they were generated by a single research group, thus reducing error which may occur due to inconsistencies in the experimental approaches of different research groups. Of course, this also has its limitations, and it would be desirable to have further verification of the validity of these diagrams.

Finally, phase diagrams for the $A_2Ru_2O_7$, $A_2Mo_2O_7$ or $A_2Sn_2O_7$ series of compounds were unable to be found.

5.1.2 Previous Modelling Studies

There have been a number of previous modelling studies which have focused on specific pyrochlore compounds. In particular, defect formation energies and anion

migration in $Gd_2Zr_2O_7$ were studied as a function of doping and disorder by Wilde and Catlow [239, 240]. In addition, Williford *et al.* [241, 242] focused on defect energetics as well as both cation and anion migration as a function of cationic disorder in $Gd_2Ti_2O_7$-$Gd_2Zr_2O_7$ solid solutions. Recently, a systematic study over a wide range of potential pyrochlore compositions was carried out by Minervini *et al.* [243]. That study attempted to correlate the energies for local disorder on both the anion and cation sublattices with the stability of the pyrochlore lattice compared to the corresponding disordered fluorite solid solution. This work was extended by Pirzada *et al.* [244] who considered the activation energy for oxygen migration, again over the same wide range of composition. Minervini *et al.* have also carried out calculations in order to determine the oxygen positional parameter in pyrochlores in an attempt to correlate these values to disorder [245]. However, no previous simulation studies which have considered the detailed mechanisms responsible for non-stoichiometry in pyrochlore compounds are known.

5.2 Methodology

The calculations carried out to determine deviations from stoichiometry are of the same type as described in Chapter 2, that is, atomistic simulations based on a Born like ionic description of the lattice and using the Buckingham short range potential to describe pair interactions, as well as the shell model to account for polarizability. Reaction energies were calculated by summing the appropriate lattice and defect energies. This process is discussed further in the Section 5.3. Many compounds are considered in this study, and as such, contour maps are employed as a convenient means of conveying such large amounts of data.

5.2.1 Contour Maps

In this study, contour maps have been used as a means of interpreting the large number of reaction energies calculated (see Figures 5.13 - 5.15). The maps sort $A_2B_2O_7$ compounds by their cationic radii: increasing A radius along the ordinate and B along the abscissa. Thus each compound occupies a point on the map. Solid points refer to a stable pyrochlore former for which calculations were carried out. Hollow points refer to compounds which have not been observed to form, i.e. exist as disordered fluorites (thus showing where the pyrochlore to fluorite compositional boundary occurs). Here, such compounds were modelled in the pyrochlore structure since this facilitates the construction of a continuous pyrochlore contour map.

For each compound modelled, a defect energy process is calculated and plotting software [246] generates contours of equal energy over the cation radius surface. Cationic radii and reaction energies are converted to a matrix via the Kriging method [247] (using a smoothness value of 0.5). This method is an optimized linear interpolation from which 3D surfaces can be generated. Using this approach, areas of compositional interest (i.e. that have similar process energies as predicted by our methodology) are easily identified. Furthermore, as these plots pertaining to isolated defects use the same scale, the trends are comparable between plots. An advantage of this approach is that predictions of properties can also be made for pyrochlore structures that were not explicitly calculated (e.g. here for hafnates: $A_2Hf_2O_7$; Hf ionic radius = 0.71Å [6]).

Brisse and Knop [248] have shown experimentally that the pyrochlore lattice parameter of lanthanide stannates ($Ln_2Sn_2O_7$) varies smoothly as a function of lanthanide (Ln) ionic radius. Furthermore, Kennedy [249] has shown using neutron diffraction that the oxygen positional parameter of the lanthanide stannate pyrochlores also changes smoothly as a function of lanthanide radius. These types

of experiments support the use of contour maps based on cationic radii as an ordering parameter.

5.3 Results and Discussion

5.3.1 Solution Mechanisms

Our first aim is to investigate the mechanisms responsible for non-stoichiometry and then correlate the results with the relative extents to which different compounds can deviate from their stoichiometric $A_2B_2O_7$ compositions. Such processes are controlled by the energetics associated with the solution reactions. Here, results are reported for the three lowest energy reactions that can be responsible for accommodating BO_2 excess and the three reactions that accommodate A_2O_3 excess without the necessity of including electronic disorder. In each case, results are normalized to reflect excess concentration of A or B ions (i.e. the non-stoichiometry). The normalization factors, which appear in front of each reaction below, have been calculated via the mass action approximation [5]. In Kröger-Vink notation [14], these reactions are as follows:

BO_2 excess:

$$\frac{7}{4}\,(BO_2 \;+\; \frac{4}{7}\,{A_A}^{x} \;\rightarrow\; \frac{3}{7}\,{B_A}^{\cdot} \;+\; \frac{1}{7}{V_A}^{\prime\prime\prime} \;+\; \frac{2}{7}A_2B_2O_7) \tag{5.1}$$

$$\frac{7}{5}\,(BO_2 \;+\; \frac{1}{7}{B_B}^{x} \;+\; \frac{4}{7}\,{A_A}^{x} \;\rightarrow\; \frac{4}{7}\,{B_A}^{\cdot} \;+\; \frac{1}{7}{V_B}^{\prime\prime\prime\prime} \;+\; \frac{2}{7}A_2B_2O_7) \tag{5.2}$$

$$\frac{4}{3}\,(BO_2 \;+\; \frac{1}{2}\,{A_A}^{x} \;\rightarrow\; \frac{1}{2}\,{B_A}^{\cdot} \;+\; \frac{1}{4}{O_i}^{\prime\prime} \;+\; \frac{1}{4}A_2B_2O_7) \tag{5.3}$$

A_2O_3 excess:

$$\frac{2}{3}\,(A_2O_3 \;+\; {B_B}^{x} \;+\; \frac{1}{2}\,{O_O}^{x} \;\rightarrow\; {A_B}^{\prime} \;+\; \frac{1}{2}{V_O}^{\cdot\cdot} \;+\; \frac{1}{2}A_2B_2O_7) \tag{5.4}$$

$$\frac{7}{4}\,(\frac{1}{2}A_2O_3 \;+\; \frac{3}{7}\,{B_B}^{x} \;\rightarrow\; \frac{3}{7}\,{A_B}^{\prime} \;+\; \frac{1}{7}\,{A_i}^{\cdots} \;+\; \frac{3}{14}A_2B_2O_7) \tag{5.5}$$

$$\frac{7}{5}\,(\frac{1}{2}A_2O_3 \;+\; \frac{4}{7}\,{B_B}^{x} \;\rightarrow\; \frac{4}{7}\,{A_B}' \;+\; \frac{1}{7}\,{B_i}^{\cdots} \;+\; \frac{3}{14}A_2B_2O_7) \tag{5.6}$$

(As previously mentioned, non-stoichiometry compensated by a variation of cationic charge state is not considered, since such reactions do not correspond to binary phase diagrams). For each compound, the constituent perfect lattice and individual defect energies were calculated (as described in Chapter 2) in order to construct the appropriate reaction energies from Equations 5.1 - 5.6 above (this required 900 separate calculations for the isolated defects alone). In all reactions, the lowest calculated lattice energies of binary oxides were used, i.e. bixbyite for A_2O_3 and either fluorite or rutile for BO_2. Where applicable, oxygen "split vacancy" defect energies were used (see Figure 5.12) according to the results of Pirzada, *et al.* [244]. This structure differs from the isolated 48f vacancy as an adjacent 48f oxygen will relax considerably towards the unoccupied 8a site. This effectively creates an additional 48f oxygen vacancy, such that there are two oxygen vacancies and an oxygen interstitial. The vacancies are oriented along the <110>. Oxygen interstitial ions were found to occupy 8a sites, as did A and B interstitials.

If the pyrochlore structure is considered to be an ordered fluorite solid solution, it seems intuitive that B cation excess should be accommodated by oxygen interstitials. For many compositions, our results are therefore at odds with intuition. Thus, our model implies that non-stoichiometry associated with B cation excess in the most stable pyrochlore compounds (i.e. the majority) is distinct from solid solution formation in fluorites. Consequently, if subsequent experiments show these results to be correct, simply assuming that pyrochlore materials are ordered fluorite solid solutions can be seriously misleading.

B cation non-stoichiometry is therefore an example of how the properties of pyrochlore compounds are predicted to evolve as their compositions move towards the pyrochlore - fluorite stability threshold, described in reference [243]. Another example is the structure of the oxygen vacancy which changes from a symmetric geometry to a split vacancy [244]. However, the boundary for that property occurs somewhat before the pyrochlore - fluorite boundary is reached. It has also been found that the extent of lattice disorder increases dramatically as this boundary is approached [245]. Such disorder demonstrates how the pyrochlore lattice evolves as a function of composition to become more similar to fluorite solid solution. However, this change is not continuous as a function of composition as evidenced by either clear order-disorder transformations (see in particular reference [237]), or by the distinct pyrochlore phase fields (see reference [238]).

Another important feature of the contour plots is how solution energies change as a function of the radii of the constituent ions. For example, in Figure 5.13a, it is clear for stannates, and by extrapolation for hafnates, that the solution energies do not vary greatly as a function of A cation radius, spanning only two contours (this example will be returned to later). Within the titanates, there is modest variation, as three contours are crossed. Conversely, there is a more considerable

increase in solution energy when the A cation (e.g. Gd) is kept constant while the B cation radius varies; typically five contours are spanned. This implies that titanate compounds have significantly higher solution energies than zirconates or hafnates.

A_2O_3 Excess

From Figure 5.14, it is clear that initial A_2O_3 excess will always be compensated by oxygen vacancies (i.e. Equation 5.4, Figure 5.14a). Therefore, non-stoichiometry associated with A_2O_3 excess is simpler than BO_2 excess in that a single solution mechanism is dominant over the entire compositional range considered. In this regard, the pyrochlore lattice is behaving like a fluorite lattice since it is well established that fluorites also accommodate the solution of A^{3+} cations by forming oxygen vacancies [250].

From Figure 5.14 it is also apparent that, for corresponding compounds, the accommodation of A_2O_3 is a higher energy process than BO_2 accommodation. This should imply that the extent of A_2O_3 solution will be lower than that of BO_2. However, the energies predicted for the hafnate series, for example, indicate that there will be considerable solution of A_2O_3 (despite the fact that our over-estimation of energies via the full charge model will tend to underestimate the extent of solution). As a consequence, it is not complete to rely only on an isolated defect model to understand the extent of solution. Therefore, defect cluster formation must be modelled.

Finally, for A_2O_3 excess, the distribution of solution energies can be considered as a function of composition (as was the case for BO_2 excess). The most favourable mechanism, i.e. Equation 5.4, Figure 5.14a, shows that the titanate series exhibit substantially higher solution energies than do zirconates, hafnates or stannates. This is similar to BO_2 excess. However, there are differences compared to BO_2 excess when the change in energies is considered within a B cation series as a function of varying A cation radius. In this case for the titanates and ruthanantes, no contours are crossed, i.e. there is no A cation radius dependence. Whereas for the zirconates, stannates and hafnates, the energy range extends over four contours, i.e. there is considerable A cation radius dependence.

5.3.3 Effect of Defect Clustering

For each defect cluster considered, it is initially necessary to ascertain its minimum energy configuration. This becomes challenging with the increasing number of constituent defects per cluster and the complexity of the lattice. Regardless, the preferential geometries for the three low energy mechanisms (i.e. Equations 2 and 4 for BO_2 solution and Equation 5 for A_2O_3 solution) were determined. The geometries are available in Table 5.1 and were used for all cluster calculations.

Defect Cluster Constituent	x	y	z
Reaction 2			
$(B_A)^{\cdot}$	0.5	0.0	0.0
$(B_A)^{\cdot}$	0.5	0.5	0.5
$(B_A)^{\cdot}$	0.25	0.25	0.5
$(V_A)^{'''}$	0.5	0.25	0.25
Reaction 4			
$(B_A)^{\cdot}$	0.5	0.0	0.0
$(B_A)^{\cdot}$	0.0	0.5	0.0
$(O_i)^{''}$	0.125	0.125	0.125
Reaction 5			
$(V_O)^{\cdot\cdot}$	0.330	0.125	0.125
$(A_B)^{'}$	0.25	0.25	0.0
$(A_B)^{'}$	0.0	0.25	0.25

Table 5.1: The perfect lattice coordinates for the preferential configuration of compensating defect clusters.

If the solution of BO_2 is considered first (see Figures 5.15a and 5.15b, where the solution energies for Equations 5.1 and 5.3 are presented), it is evident that clustering of the compensating defects lowers the overall energy (compare to Figures 5.13a and 5.13c). It is also evident that for all stannates and hafnates (Hf ionic radius = 0.71Å [6]), the solution of BO_2 is still largely independent of A cation radius (i.e. the range of solution energies is no greater than 0.2eV over these series). However, the situation for the titanates is once again more complex with solution energies increasing as a function of A cation radius (the variation is 0.7eV over the titanate series).

Although defect clustering lowers reaction energies, the distribution of contour positions remains similar (compare values in Figures 5.13a, 5.13c and 5.14a with Figures 5.15a, 5.15b and 5.15c respectively). For example, Figure 5.13c shows a dip in the bottom left corner as does the corresponding Figure 5.15b. Nevertheless, the spacing between contours is greater in Figure 5.15 since clustering leads to smaller variations in solution energies between compounds (with the same energy scale used for all diagrams). However, clustering does not change the lowest predicted energy mechanisms for accommodation of non-stoichiometry deduced from the results assuming an isolated defect model.

5.3.4 Comparison to Phase Diagrams

The results presented in sections 3.2 and 3.3 above can be correlated to the phase diagrams which include the $A_2Ti_2O_7$, $A_2Zr_2O_7$ and $A_2Hf_2O_7$ compounds.

This comparison begins by considering the most complete set of phase diagrams, that is, those diagrams that exhibit a stable $A_2Hf_2O_7$ compound [235–238]. These diagrams show that the extent of BO_2 excess non-stoichiometry is not drastically affected by varying the A cation radius (the stoichiometry range limit is approximately constant at 70 mol percent BO_2). This behaviour is consistent with the prediction of Figures 5.13a and 5.15a, in that only one contour is crossed, i.e. the solution energy does not alter greatly with varying A cation. The low energies in this region of the map are also consistent with the considerable BO_2 excess non-stoichiometry observed experimentally.

Considerable A_2O_3 excess non-stoichiometry is also predicted in the hafnates, as a consequence of the low energy regions of the contour maps Figures 5.14a and 5.15c. This is also in qualitative agreement with experimental observations. For $A_2Hf_2O_7$, where A = Sm, Eu and Gd, the solution energy for A_2O_3 excess is practically

the same as for BO_2 excess. Thus the pyrochlore phase field should be essentially symmetric about the stoichiometric ratio (i.e. at $\approx 66\frac{2}{3}$ mol percent BO_2). Again, this is what is observed [237]. However, the energies for A_2O_3 excess begin to increase for compounds of larger A radii, e.g. Nd, Pr and La. From this prediction, a reduction in the extent of A_2O_3 excess non-stoichiometry is expected for these compounds. Although, it is difficult from the experimental data to be definitive, as the A radius increases, the extent of A_2O_3 excess non-stoichiometry does indeed seem to fall from approximately 60 mol percent BO_2 to approximately 64 mol percent BO_2 [238].

Many titanate phase diagrams [214–218] have the pyrochlore structure occurring only as a line compound, recall Figure 5.1. Conversely, several phase diagrams mentioned contradict this picture and show a deviation from pyrochlore stoichiometry which is pronounced in the BO_2 direction but still non-existent in the A_2O_3 direction see Figures 5.2 and 5.3 [221, 222]. Our results do predict that the titanates will exhibit less deviation from stoichiometry than will other series of B cations. However, for BO_2 excess, since these solution energies for the titanates are only modestly greater then for zirconates or hafnates (see Figure 5.15a), some discernable deviations from the stoichiometric ratio for BO_2 excess is expected. Conversely, little if any non-stoichiometry is expected for A_2O_3 excess, due to the rather high relative energy of this process (see Figures 5.14a and 5.15c).

A contributing factor to difficulties in investigating the titantates experimentally compared to the hafnates might be the greater difference between the solution energies predicted assuming isolated defects (Figure 5.13a) versus clustered defects (Figure 5.15a). Since cluster formation in titanates lowers solution energies more, it may be that titanates take longer to reach equilibrium than do hafnates as cluster formation requires cation migration. Nevertheless, it would seem to be potentially

worthwhile to revisit the titanates experimentally.

It is difficult to make any definite comparisons to the existing set of zirconate phase diagrams [223–226], due to the predominantly hypothesized nature of their pyrochlore phase fields. However, what is clear from these phase diagrams is that the zirconate pyrochlores are expected to exhibit non-stoichiometry in both the BO_2 and A_2O_3 directions. The relative energies observed in the contour plots predict slightly greater deviations from stoichiometry for the zirconates than for the hafnates. Again, the phase fields should be essentially symmetric for $A_2Zr_2O_7$ where A = Dy to Sm, but asymmetric with greater ZrO_2 excess than A_2O_3 excess for A = Nd to La.

Of course, it is desirable to have a more complete series of phase diagrams with which to compare the current predicted trends. Hopefully, this study will stimulate further experimental work focused on determining the extent of non-stoichiometry in various pyrochlore oxides. Given the excellent crystallographic data available for the stannates [249, 251] and their significant non-stoichiometry, this series may be particularly profitable to study.

5.4 Conclusions

There are a number of general and specific conclusions that result from this work. Firstly, some general comments are made.

Given the great number of calculations necessary to carry out this comparative type study, a simple computational approach was employed. Given the limitations of such a methodology, trends have been focused on, rather than absolute solution energies. However, the trends are clearly complex and therefore required a contour map approach to aid with interpretation.

It seems that the calculated trends agree with the available, albeit confused, experimental data. The maps can therefore be used as a basis for further systematic

experimental studies. Furthermore, the maps can be used to select compositions that exhibit greater or lesser deviations from stoichiometry. Of course the maps can be used predictively to consider elements which have not been explicitly modelled, but whose ionic radii are known. This may also include certain compounds whose elements that are able to exhibit variable charge states (e.g. Pr and Ce containing). This will form the basis of a future study.

Some specific comments should also be made.

- It is predicted that for stable pyrochlore formers, non-stoichiometry associated with BO_2 excess is generally accommodated by forming A^{3+} cation vacancies. As the pyrochlore - fluorite boundary is approached, oxygen interstitial ions will also contribute to the solution mechanism, resulting in complex defect behaviour.

- These calculations therefore demonstrate that the mechanism for BO_2 excess non-stoichiometry in pyrochlore oxides is distinct from solid solution formation in fluorite, especially for the majority, stable pyrochlore compositions.

- Oxygen vacancies are clearly the defects that accommodate the solution of excess A_2O_3 in all pyrochlore compositions considered in this study. In this regard, pyrochlores are behaving like fluorite solid solutions.

- The clustering of compensating defects lowers the overall energy of each mechanism, but does not affect the preferential solution mechanism or greatly affect the relative energies predicted by isolated defect calculations.

- The model predicts that the extent of BO_2 excess non-stoichiometry in hafnates, zirconates and stannates will be considerably greater than for titanates or ruthanates. Furthermore, while the possible deviation is constant for haf-

nates in particular, it decreases as a function of increasing A cation radius for the titanates.

- Similarly, the extent of A_2O_3 excess non-stoichiometry in hafnates, zirconates and stannates is again much greater than for titanates or ruthanates, the latter probably not exhibiting any substantial deviation.

Chapter 6

Prediction of Rare Earth $A_2Hf_2O_7$ Pyrochlore Phases

"If, without disturbing a system, we can predict with certainty the value of a physical quantity, then there exists an element of physical reality corresponding to this physical quantity."

- Albert Einstein

Physical Review, 1935

6.1 Introduction

Materials with the pyrochlore lattice exhibit properties that are advantageous for applications as diverse as dielectrics [199, 200] and actinide host phases [208, 211]. However, the phase stability for any $A_2B_2O_7$ pyrochlore compound (where A is a 3+ rare earth cation ranging in size from Lu^{3+} to La^{3+} and B is a 4+ cation ranging in size from Ti^{4+} to Pb^{4+}) is not well characterized. Limited and at times conflicting phase diagrams exist for the series of compounds $A_2Zr_2O_7$ and $A_2Ti_2O_7$

(refer to Figures 5.1, 5.2 and 5.3 for titanates and Figures 5.5 and 5.6 for zirconates). However, there is a more complete set of data showing the existence of certain $A_2Hf_2O_7$ compounds (refer to Figures 5.9, 5.10 and 5.11).

Considering this latter series further, the HfO_2 - Pr_2O_3 and HfO_2 - La_2O_3 phase diagrams [238], both exhibit a considerable pyrochlore phase field which melts congruently (i.e. the liquid is the same composition as the compound) at 2420^{o}C and 2460^{o}C $\pm$25^{o}C respectively. The HfO_2 - Nd_2O_3 and HfO_2 - Sm_2O_3 phase diagrams [237, 238] similarly exhibit significant pyrochlore phase fields, but both melt incongruently at 2450^{o}C and 2550^{o}C $\pm$25^{o}C respectively. The HfO_2 - Tb_2O_3, HfO_2 - Gd_2O_3 and HfO_2 - Eu_2O_3 phase diagrams [237, 252] also exhibit a pyrochlore phase field, however, these do not melt but rather undergo an order-disorder transformation at 2150^o, 2350^{o}C and 2450^{o}C $\pm$50^{o}C respectively. All HfO_2 - A_2O_3 phase diagrams with A smaller than Gd^{3+}, including Dy_2O_3 - HfO_2 [235, 237, 252, 253], show no evidence of pyrochlore compound formation. In all cases, the experimental error of the order-disorder temperature is given as denoted in the original texts.

Figure 6.1, although consisting of A_2O_3 - HfO_2 differs from those in Chapter 5. Each of the phase diagrams in Figure 6.1 was obtained from the original texts. Here, the transition from no pyrochlore phase observed for the Dy_2O_3 - HfO_2 system to a pronounced pyrochlore region in the Tb_2O_3 - HfO_2 is evident, as is the subsequent progression of the pyrochlore phase (i.e. the increase in order-disorder temperature) from Gd_2O_3 - HfO_2 up to Eu_2O_3 - HfO_2. The benefit of the original experimental data is that the temperatures at which the experiments are clearly labelled. This will be shown to be important in the forthcoming sections.

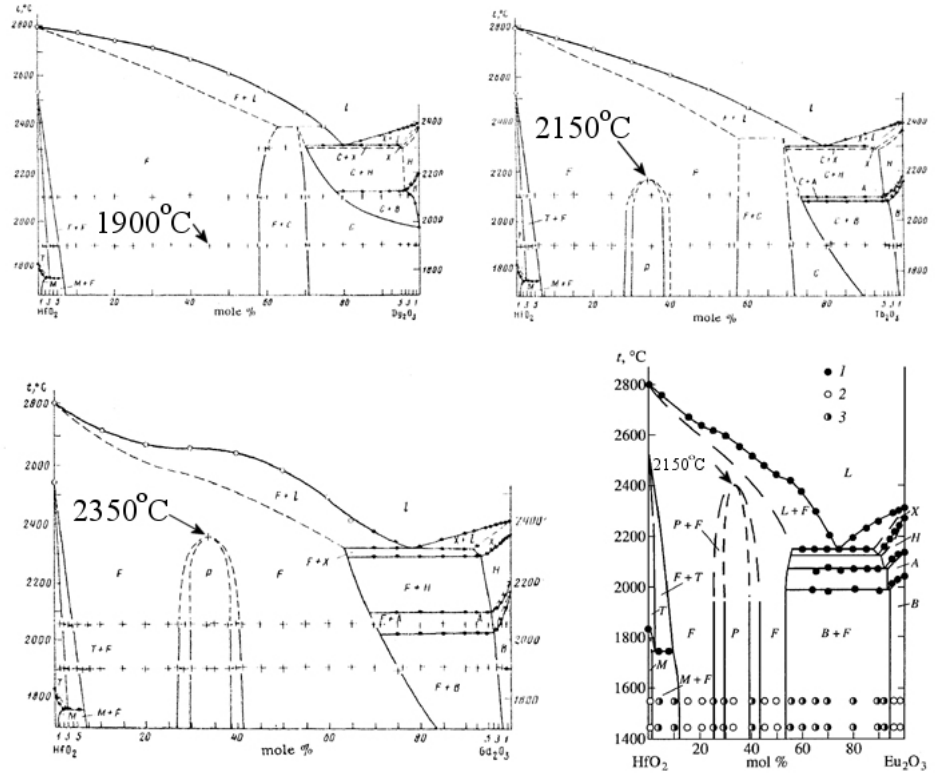

Figure 6.1: Phase diagrams of the $A_2Hf_2O_7$ series of compounds for intermediate A^{3+}, reproduced from [236, 237, 252].

The completeness of the HfO_2 - A_2O_3 series of phase diagrams allows us to compare this experimental data with atomistic simulation calculations. The simulations provide relative energies of a local disorder process for a wide range of pyrochlore compounds [243]. From these disorder energies and the aforementioned phase diagrams, it is possible to generate an Arrhenius-type plot of disorder temperature versus disorder energy, which predicts order-disorder temperatures for $Dy_2Hf_2O_7$ as well as $Ho_2Hf_2O_7$ and $Er_2Hf_2O_7$. These compounds have not been previously observed experimentally.

6.2 Methodology

Atomistic simulation calculations were carried out based on a Born like, ionic description of the lattice [79] and using the Buckingham potential to describe the short range interactions between ions (see Table 2.5 for the complete listing of potentials used). The polarizability of ions is accounted for by the shell model [109], where a massless shell of charge Y$|e|$ is coupled to a massive core of charge X$|e|$ by a force constant, k. All calculations consider O^{2-} and larger B^{4+} cations as polarisable. The shell parameters used can be found in Table 2.5. A comprehensive description of the Mott-Littleton defect calculation methodology is provided in Chapter 2 and elsewhere [254]. In all cases, calculations were carried out using the CASCADE code [127], which employs energy minimization to predict relaxed ion positions. The reader is referred to Chapter 2 for computational details.

The approach described has been used successfully to predict various properties of $A_2Hf_2O_7$ pyrochlores, including oxygen migration [244], disorder process energies [243] and the effect of disorder on the oxygen positional parameter [245].

6.3 Results and Discussion

By far the two most important disorder processes for pyrochlores are: cation antisite and anion Frenkel [250]. Cation antisite is essentially the swapping of an A^{3+} cation for a B^{4+} cation:

$$A_A^x + B_B^x \rightarrow A'_B + B^{\cdot}_A \tag{6.1}$$

Frenkel anion disorder proceeds when an oxygen ion on a 48f site is displaced to an 8a interstitial site, thus leaving the 48f site unoccupied:

$$O_O^x \rightarrow V^{\cdot\cdot}_{(48f)} + O''_{i(8a)} \tag{6.2}$$

Previous simulation results [243] for both of these processes for an extensive range of pyrochlore compounds were presented in the form of contour maps. These clearly demonstrate the same trend for both cation antisite and anion Frenkel. That is, the enthalpy increases considerably with increasing B cation radius, while the increase in enthalpy with increasing A radius is less pronounced. These results are qualitatively supported by experimental studies [204, 255].

However, for the three series of pyrochlore compounds: $A_2Sn_2O_7$, $A_2Hf_2O_7$ and $A_2Zr_2O_7$, the extent of disorder at temperatures above 1000K is sufficient for defect clusters to form [245]. Therefore, the appropriate disorder reaction (as discussed in [243]) involves the formation of neutral defect clusters consisting of a cation antisite pair adjacent to an anion Frenkel pair:

$$A_A^x + B_B^x + O_O^x \rightarrow \{A'_B + B_A^{\cdot} + V_{O(48f)}^{\cdot\cdot} + O''_{i(8a)}\}^x \tag{6.3}$$

The rationale for defect cluster formation in these systems has been established in previous publications [239, 242].

though calculations have not been performed for $Dy_2Hf_2O_7$, the disorder energy can be extracted from the contour map, as shown in Figure 6.2 (Dy ionic radius = 1.027Å and Hf ionic radius = 0.71 Å [6]). Indeed, disorder energies can be obtained from this map for the entire series of $A_2Hf_2O_7$ pyrochlores, despite not calculating the values explicitly.

If the local disorder energy for each $A_2Hf_2O_7$ pyrochlore obtained from Figure 6.2 is correlated with the known disorder temperature (via an Arrhenius plot [257], see Figure 6.3), it is found that there is, within experimental error, a linear relationship. Such an observation supports the idea that, for each compound of this series, the local disorder energy is related to an order - disorder enthalpy. Of course, our local order - disorder internal energies are incomplete compared to order - disorder free energies. Consequently, further work is being carried out in order to develop a more thorough thermodynamic interpretation.

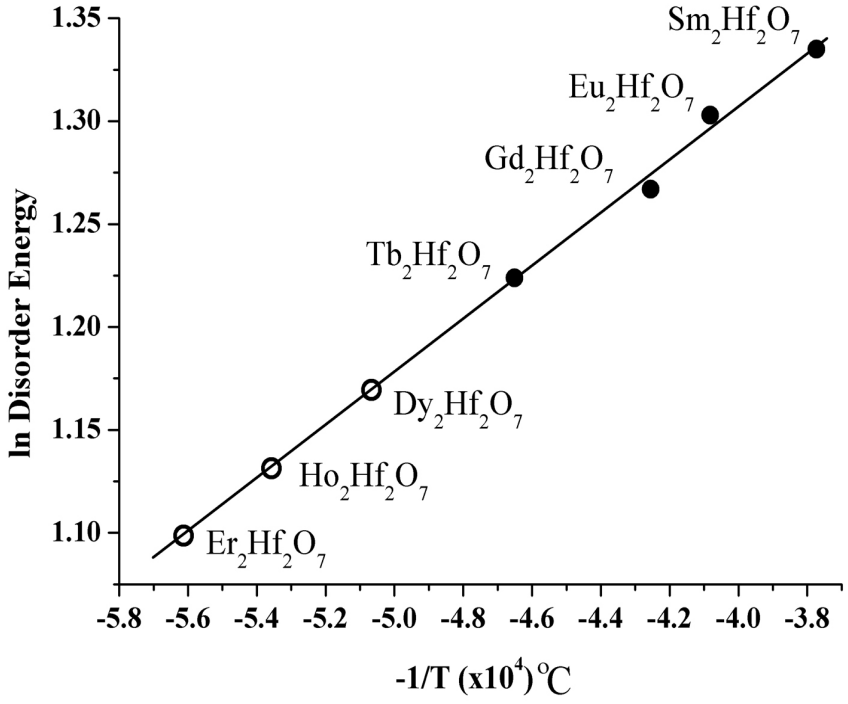

Figure 6.3: An Arrhenius plot of local disorder energy versus temperature. From the linear fit of the pyrochlore formers (solid points), it is possible to predict formation temperatures for three other compounds: $Dy_2Hf_2O_7$, $Ho_2Hf_2O_7$ and $Er_2Hf_2O_7$.

Despite its approximate nature, there exists a useful relationship which, via Figure 6.3, can be used to predict order - disorder temperatures for compositions which have not yet been observed in the pyrochlore structure, but only as fluorite solid solutions. For example, it is clear from Figure 6.3 that, next to those pyrochlores already observed, $Dy_2Hf_2O_7$ will be the composition with the highest predicted order - disorder temperature: $1975^oC \pm 50^oC$.

It is now possible to revisit the region of the Dy_2O_3 - HfO_2 phase diagram where a $Dy_2Hf_2O_7$ pyrochlore should be observed, see Figure6.1. The experimental points from which the phase diagram was constructed ($1900^oC \pm 50^oC$) are found to be at

the threshold temperature of a stable pyrochlore, as indicated by points in Figure 6.1. Conversely, order - disorder temperatures predicted for $Ho_2Hf_2O_7$, 1865^{o}C $\pm$50^{o}C and $Er_2Hf_2O_7$, 1780^{o}C $\pm$50^{o}C are well below the experimental data points.

The aim of this prediction is to stimulate experimental investigation. The recent work of Helean *et al.* [258] lends itself to verifying the prediction of this chapter. Using high temperature oxide melt calorimetry, Helean *et al.* have derived enthalpies of formation for several pyrochlores.

Chapter 7

Concluding Comments and Future Work

"There always remain in the abyss of things slumbering, parts which have yet to be awakened."

- Gottfried Wilhelm von Leibniz

On the Ultimate Origination of Things, 1697

7.1 Summary

The last four chapters have attempted to solve problems, all of which involve disorder in ceramic systems. In particular, each of these chapters dealt with a specific technological issue, the detailed conclusions of which are included in each chapter. It is therefore not the purpose of this chapter to repeat those results. However, what has not yet been provided is the connection between each chapter and their general relation to disorder.

Firstly, all of the systems considered in this thesis involve fluorite or fluorite related oxides, namely UO_2, ZrO_2 and $A_2B_2O_7$. Furthermore, each chapter dealt with some aspect of structural disorder in one of these systems. In Chapter 6, intrinsic disorder was considered in the $A_2B_2O_7$ group of materials. The calculation of defect energies led to a prediction of yet unobserved compounds, namely $Dy_2Hf_2O_7$, $Ho_2Hf_2O_7$ and $Er_2Hf_2O_7$. This was facilitated by relating the fluorite to pyrochlore disorder transformation temperature to a local disorder process. Chapter 5 considered non-stoichiometry in the same series of compounds, broadening the scope to consider a form of extrinsic disorder that does not involve species foreign to the lattice constituents (recalling the comments from Chapter 1, classifying only thermally activated disorder as intrinsic, though it is acknowledged that non-stoichiometry is at times referred to as intrinsic). Chapter 3 considered the solution of fission products, especially Kr, thereby further expanding the types of disorder considered to include a species different than that of the lattice ions (and therefore clearly extrinsic). In each of these three chapters, each system was modelled as an infinite single crystal.

However, real materials have surfaces and it is important to acknowledge that with respect to an infinite crystal, surfaces are defects (it is noted that grain boundaries are another form of termination, though not considered in this work). Surfaces were included in Chapter 4, through the calculation of segregation energies. The segregation studies show quite clearly how strong the influence of surface structure can be on defect behaviour. That is, the defect energies change dramatically increasing or decreasing in stability as they approach a specific surface.

This thesis is not an exhaustive study of disorder in fluorite and fluorite related oxides. Rather, it is a selective representation of important concepts. In many cases, the models were forced to make use of approximations on account of the complexity

of the problems encountered. As computing resources continue to improve, these approximations will either become unnecessary or at least less significant (e.g. as the size of the repeat units can be increased further). Although much information has been presented in this thesis, there is still even more work needed in order to better understand disorder and all of its manifestations in these materials. Some possibilities for further work are discussed in the following section.

7.2 Future Work

7.2.1 Bulk Related Studies

- Figure 4.4 described the binding energy between a divalent ion and a charge compensating oxygen vacancy as a function of distance between these two species. This plot showed that at rather large separations (i.e. ≈10Å), the binding energy is still ≈25% of its maximum value. This result suggests that the idea of a completely isolated defect is only valid at dopant levels below 0.1%. An improved Debye-Hückel correction should be developed to better describe defect - defect interaction.

- The material systems modelled in this work have the advantage (from the pair potential point of view) of being highly ionic. As noted in Chapter 3, high quality quantum mechanical calculations are accepted as a more accurate representation, in terms of electronic contributions. Currently, QM calculations are limited by the number of atoms that can be realistically considered. As computing resources improve, QM type calculations will become more feasible, as more atoms will be able to be modelled.

- Contour maps can be used predictively to consider elements which have not

been explicitly modelled, but whose ionic radii are known. This may also include certain compounds whose elements that are able to exhibit variable charge states (e.g. Pr and Ce containing). However, the consideration of elements with variable charge state requires comparison to ternary phase diagrams. This problem becomes even more complicated if the charge state varies with temperature, which would then introduce another variable- the partial pressure of oxygen.

- In order to validate the prediction of $Dy_2Hf_2O_7$ formation (as discussed in Chapter 6), experimental verification is necessary. It is the belief of the author that precision calorimetry experiments will yield results supporting the predictions described in Chapter 6. However, it is also acknowledged that experiments of this type are difficult. As previously mentioned, there are two cation sublattices in the pyrochlore structure. If there is ordering of these cationic sublattices, it will take long periods of time to reach equilibrium. Also, there may be deviations from stoichiometry if the sample reacts with the gas phase.

7.2.2 Surface Related Studies

- The segregation of fission products to surfaces of UO_2 was a more complicated problem than initially expected. With improved computing resources, the remaining calculations can be completed in order to formulate a systematic statement regarding the segregation of these fission products in this system.

- In addition to free surfaces, the segregation of fission products to grain boundaries in UO_2 is significant. In a similar fashion to the model used in Chapter 5 to simulate segregation to free surfaces, it is possible to model segregation

to grain boundaries. However, it is noted that these calculations will be even more intensive than those considering only free surfaces. Instead of considering a single simulation cell, grain boundary calculations require another cell of a specific orientation placed on top of the original cell. This significantly increases the number of atoms which need to be considered.

- Oxygen vacancy diffusion can be calculated in UO_2, CeO_2 or ZrO_2, as it is an important phenomenon in all of these materials. Vacancy migration was not originally considered because of code limitations, namely the lack of ability to simulate charged defects. However, a methodology has been formulated which will allow us to circumvent the problem. First, a defect cluster such as $\{(Ba_U)'':(V_O)^{\cdot\cdot}\}$ is introduced near to the bottom of the repeat unit, as far from the surface as possible. The cation is then pinned whilst moving the oxygen vacancy towards the surface. The binding energy of the oxygen vacancy to the barrier defect can be calculated independently, and subsequently subtracted from the clustered defect energy at each corresponding oxygen vacancy step. Therefore, the only energy of interest is that of the oxygen vacancy nearing the surface. The binding energy correction term is determined by performing a similar calculation with the repeat unit mirrored at the surface in order to account only for bulk effects. This correction assumes that the $(Ba_U)''$ defect pinned in the bulk does not alter the phenomenon at the surface significantly and needs to be examined more closely. In this case, a code such as CHAOS [74] might be more useful in that it treats Region II as a dielectric continuum.

- This thesis has not taken into account space charge effects. This effect is noted to be of importance, but unfortunately, there was not enough time to take it into consideration. The formation of electrically active surfaces and

grain boundaries via this effect is thought to be especially important.

- In Chapter 4, the limitations of the MARVIN code were discussed. In addition to region size issues, the issue of Region II polarizability was mentioned. Clearly, modifications to the code in order to include Region II polarizability are necessary. This could take the form of a single continuum approximation (e.g. analogous to the Mott-Littleton Region IIb approach), or a layer by layer calculation where ions are dispersed (e.g. more like the Mott-Littleton Region IIa).

- At this point, the surfaces of pyrochlores have yet to be investigated. If these materials are to be used as nuclear waste forms, then surface related phenomena (such as dissolution) is important. Initially, morphology and hydroxylation calculations are possible, as these calculations have already been performed on similar materials, such as UO_2 [46, 259]. The simulation of radiation damage is also of interest. This might require molecular dynamics in order to simulate the instantaneous amount of energy which needs to be transferred to an ion during irradiation.

Appendix A

Segregation of Yttrium Ions to the Surfaces of t-ZrO_2

This work will be published in Mat. Res. Symp. Proc., vol.751 #21.6. These calculations were initiated by Dr. S.E. Redfern but repeated and completed by the author.

A.1 Abstract

Atomistic simulation has been used to predict the segregation of defect clusters containing two substitutional Y^{3+} ions and one charge compensating oxygen vacancy to the (100) and (101) surfaces of t-ZrO_2. The most stable orientation of the defect cluster depends on its distance from the surface. Significantly, segregation energies vary greatly between surfaces. For example, the defect cluster is equally stable up to a depth of 8Å from the (100) surface but only to a depth of 4Å below the (101) surface. In both cases, segregation energies are negligible 14Å beneath the surface.

A.2 Introduction

At temperatures below ≈1000^{o}C the crystal structure of zirconia is monoclinic. Above this temperature it transforms to a structure with tetragonal symmetry. However, a suitable combination of small grain size and the addition of an appropriate amount of a stabilising oxide, e.g. 3mol% yttria (Y_2O_3), results in a metastable tetragonal structure (t-ZrO_2) even at room temperature. This metastable material is commonly known as tetragonal zirconia polycrystalline ceramic (TZP) and has excellent mechanical properties. Unfortunately a complication arises at moderate temperatures (typically 60-200^{o}C), when the presence of moisture causes the tetragonal phase to uncontrollably transform into the more stable monoclinic phase, thus degrading the mechanical performance [260, 261]. Microstructural studies have shown that the reaction is nucleated at the surface and that the nuclei grow to form a monoclinic surface layer, which increases in thickness with time [262–264]. Unfortunately, the nucleation mechanism is not well understood.

One suggestion for the origin of monoclinic nucleation is the preferential dissolution of yttria due to the presence of water [265]; this leaching causes a local reduction in yttria content, which may lead to the transformation. As part of this mechanism, it is proposed that yttrium ions segregate to surfaces of t-ZrO_2 grains. Furthermore this segregation, and hence the leaching rate, is orientation dependent. The atomic simulation work reported here was designed to investigate this hypothesis under dry conditions by modelling the surface orientation dependence of the driving force for segregation.

There have been a number of previous experimental studies concerning segregation effects in TZP. For example, yttrium ions have been explicitly shown to segregate to grain boundaries [266] and to domain boundaries [267]. In addition, the segregation of Sr and Bi to surfaces of polycrystalline TZP has been studied

using angular-resolved X-ray photoelectron spectroscopy [268, 269]. Within the resolution limits of this technique, the results were consistent with there having been an increase in concentration of Bi in the top five atomic layers [269] whereas for Sb results were consistent with segregation to the top fifteen layers [268].

A.3 Methodology

The methodology used in these calculations is based on a pair potential description of forces between charged ions, as described in Chapter 2. Surfaces are modelled using a 2D repeat unit (the simulation block) whose thickness is in excess of 40Å. Final ion positions are determined through energy minimisation techniques. Using the tetragonal unit cell index, the (100) and (101) surfaces of t-ZrO_2 are studied; these are type I and II respectively [182]. Details of the computational technique and the model parameters are available in previous publications [77, 259, 270, 271].

In the model presented here, trivalent Y^{3+} cations substitute for Zr^{4+}, and thereby form charged defects. Two such substitutional defects are compensated by an oxygen vacancy to form, in Kroger-Vink notation, the defect cluster $\{(Y_{Zr})':(V_O)^{\cdot\cdot}:(Y_{Zr})'\}$. The most stable geometric configuration for this cluster is when both cations are in second neighbour positions with respect to the oxygen vacancy. The same result was found previously in studies of yttria doped cubic zirconia [272].

Segregation trends have been modelled by calculating the total internal energy of the simulation block as the cluster was moved from the bulk stepwise to the surface. The depth of the cluster from the surface is defined with respect to the position of the oxygen vacancy. This is the same approach used to investigate the segregation of fission products in UO_2 as reported in Chapter 4 and [273]. However, this technique was developed earlier to model impurities in other ceramic systems [274–276].

In a bulk crystal all orientations of a fixed geometry defect cluster are equivalent.

Conversely, when a surface is introduced, there is an inherent directionality; that is, the cluster has several non-equivalent orientations with respect to the surface. Thus, when the cluster is deep within the simulation block the differences in energy between different orientations becomes small. However, as the cluster approaches the surface different cluster orientations result in different total energies. In the present study, this meant that below 14Å all cluster orientations had practically the same energy. However, as the cluster approaches the (100) and (101) surfaces, there are four unique orientations of the second neighbour yttrium ions for each fixed position of the oxygen vacancy. All four possibilities were investigated at each position of the oxygen vacancy as it moved from the surface into the bulk. Table A.1 provides the coordinates for each of these defect cluster orientations, including those with respect to the (110) surface, although the results for that surface are not discussed.

(100)	x_1	y_1	z_1	x_2	y_2	z_2
A	x+3.59	y-1.45	z+1.80	x	y+3.67	z+1.80
B	x-1.80	y+3.67	z	x-1.80	y-1.45	z-3.59
C	x+3.59	y-1.45	z-1.80	x	y+3.67	z-1.80
D	x-1.80	y+3.67	z	x-1.80	y-1.45	z+3.59
(101)						
A	x-1.80	y-3.25	z±2.11	x-1.80	y+3.01	z±2.11
B	x-1.80	y+3.01	z±2.11	x-1.80	y+0.88	z±3.77
C	x-3.59	y+0.16	z±2.30	x	y-4.04	z±0.67
D	x-3.59	y+2.22	z±0.64	x	y+1.97	z±3.59
(110)						
A	x+1.27	y-1.11	z+3.81	x-1.27	y+3.67	z+1.27
B	x-1.27	y+3.67	z+1.27	x-3.81	y-1.11	z-1.27
C	x+3.81	y-1.11	z+1.27	x+1.27	y+3.67	z-1.27
D	x+1.27	y+3.67	z-1.27	x-1.27	y-1.45	z-3.81

Table A.1: Coordinates of (Y_{Zr})' sites with respect to the oxygen vacancy (at (x,y,z)), where the notation A,B,C and D is used in the results. The Z direction is perpendicular to the surface plane and therefore denotes depth below surface.

Finally, for the (101) surface, symmetry results in there being an inversion in the (101) plane of the positions of the second neighbour zirconium lattice sites with respect to an oxygen site in each successive oxygen layer. That is, the zirconium sites are above the oxygen vacancy with respect to the (101) surface in one layer

A.4.1 The (101) surface: Type II Surface

The (101) surface has been shown to be the most stable of the three perfect surfaces studied under dry conditions [270]. The energetics associated with the segregation process are shown in Figure A.2. It is clear that the cluster is more stable at the surface than in the bulk. The value calculated for E_S = -2.5eV, so that the driving force for segregation is strong. However, the stability of the cluster within the first three layers beneath the surface is constant. In fact, there may even be a very shallow trap site (E_T = 0.13eV) at a distance of 4Å from the surface plane. It is therefore expected that yttrium will segregate towards the (101) surface forming a higher concentration layer extending over 4Å (i.e. three or perhaps even four layers from the top). This result is consistent with the experimental observations on Bi segregation to the top five atomic layers in polycrystalline TZP [269]. It is also clear from Figure A.2 there is some smaller driving force for segregation ($E_S \gg$ 0.6eV) from the interior (bulk) to a region between 6 and 14Å. It seems likely that this is a consequence of the (101) surface being Type II. This is supported by the small energy differences between cluster orientations in this depth region, where the cluster dipole is interacting with the local dipole. Furthermore, analysis of ion displacements shows almost no movement for ions in layers beneath 8Å.

A.4.2 The (100) surface: Type I Surface

The energy associated with segregation of the cluster to the (100) surface is shown in Figure A.3. At distances of 9Å or more from the surface, the total energy no longer depends significantly on cluster orientation. However, similarly to the (101) surface, as the cluster approaches the surface, a strong configurational dependence is apparent. Interestingly the segregation energy, E_S, is larger than for the (101) surface, with a value of -3.29eV. This indicates that the (100) surface could be

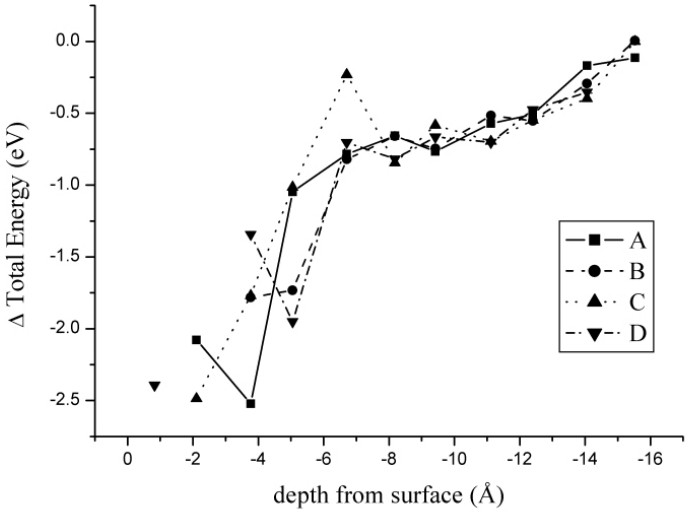

Figure A.2: Segregation of (Y_{Zr})' to the (101) surface of t-ZrO2.

stabilised with respect to the (101) surface through the addition of yttria. However, the extent to which this surface is stabilised will be concentration dependent. In this context, it may also be significant that the (100) surface shows this greater cluster stability within the top five layers compared to only three or four layers with the (101) surface.

An interesting feature of the (100) surface is the lack of stability of most configurations in the second and third layers beneath the surface. Clearly the distribution of yttria in surface layers may be quite complex. Nevertheless, this Type I surface seems well behaved in that values for E_S drop to zero very clearly below 10Å. This is the depth below which there are no significant displacements of ions from their bulk lattice positions.

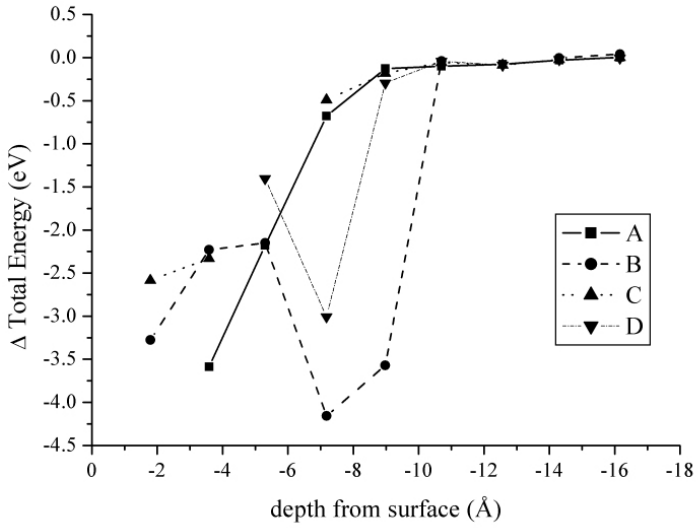

Figure A.3: Segregation of (Y_{Zr})' to the (100) surface of t-ZrO2.

A.5 Conclusions

Y^{3+} ions as part of neutral clusters are more stable in layers beneath the (101) and (100) surfaces than in the interior bulk crystal. This provides a driving force for segregation.

The segregation energy is greater for the (100) surface compared to the (101).

There is a correlation between the extent of surface relaxation and segregation effects. However, for Type II surfaces, cluster orientation effects persist at greater depths.

It has been calculated in a previous study [270] that under dry conditions, the morphology of a single crystal of tetragonal zirconia is dominated by the (101) face, with the (100) surface not present and the Type III (110)A present to a minor degree. The present results imply that segregation of yttria to the crystal surfaces could be significant in promoting the amount of (100) surface present by lowering its energy with respect to the (101) surface.

A.6 Acknowledgements

Support for this work was provided by the EPSRC, grant number GR/M 44903 via the ROPA scheme. Simon Phillpot is thanked for sharing his potentials.

Bibliography

[1] P.W. Kasteleyn, in *Theory of Imperfect Crystalline Solids*. International Atomic Energy Agency (1971).

[2] L. Pauling, *The Nature of the Chemical Bond and the Structure of Molecules and Crystals: An Introduction to Modern Structural Chemistry*, Cornell University Press, Ithaca, NY (1960).

[3] L. Pauling, *J. Am. Ceram. Soc.* **51** 1010 (1929).

[4] J.K. Burdett, *Chemical Bonding in Solids*, Oxford University Press, New York (1995).

[5] Y.M. Chiang, D.P. Birnie III and W.D. Kingery, *Physical Ceramics*, John Wiley & Sons, Inc., New York (1997).

[6] R.D. Shannon, *Acta Cryst. A* **32** 751 (1976).

[7] R.W.G. Wyckoff, *Crystal Structures*, vol. 1, Interscience, New York, 2nd edn. (1963).

[8] N.F.M. Henry and K. Lonsdale, eds., *International Table for X-Ray Crystallography*, Kynoch Press, Birmingham (1952).

[9] S.M. McDeavitt, *J. Mater.* **52** 11 (2000).

[10] M.A. Subramanian, G. Aravamudan and G.V. Subba Rao, *Prog. Solid State Chem.* **15** 55 (1983).

[11] E. Aleshin and R. Roy, *J. Am. Ceram. Soc.* **45** 18 (1962).

[12] J.M. Longo, P.M. Raccah and J.B. Goodenough, *Mat. Res. Bull.* **4** 191 (1969).

[13] C. Wagner, *Trans. Faraday Soc.* **34** 851 (1938).

[14] F.A. Kröger and H.J. Vink, *Solid State Physics - Advances in Research and Applications*, Academic Press, New York (1957).

[15] J. Frenkel, *Z. Phys.* **35** 652 (1926).

[16] W. Schottky and C. Wagner, *Z. phys. Chem.* **11B** 335 (1930).

[17] W. Schottky, *Z. phys. Chem.* **29B** 335 (1935).

[18] R. Dieckmann, *J. Phys. Chem. Solids* **59** 507 (1998).

[19] J. Stirling, *Methodus Differentialis*, London (1730).

[20] T.J. Gray, *The Defect Solid State*, Interscience Publishers, Inc., New York (1957).

[21] P. Kofstad, *Non-Stoichiometry, Diffusion and Electrical Conductivity in Binary Metal Oxides*, Wiley - Interscience, New York (1972).

[22] J. Dalton, *A New System of Chemical Philosophy*, Manchester (1808).

[23] N.S. Kurnakov, *Z. anorg. Chem.* **52** 430 (1907).

[24] L. Solymar and D. Walsh, *Lectures on the Electrical Properties of Materials*, Oxford University Press, Oxford (1995).

[25] C. Kittel, *Introduction to Solid State Physics*, John Wiley & Sons, Inc., New York, 5th edn. (1976).

[26] L. Meitner and O.R. Frisch, *Nature* **143** 239 (1939).

[27] O.R. Frisch, *Nature* **143** 276 (1939).

[28] L. Badash, E. Hodes and A. Tiddens, *Nuclear Fission: Reaction to the Discovery in 1939*, University of California, San Diego (1985).

[29] E. Fermi, E. Amaldi, O. D'Agostino, F. Rasetti and E. Segrè, *Proc. Roy. Soc.* **A146** 483 (1934).

[30] H. Bethe, *Phys. Rev.* **47** 747 (1935).

[31] G. Breit and E. Wigner, *Phys. Rev.* **49** 519 (1936).

[32] O. Hahn and F. Strassman, *Naturwiss.* **26** 756 (1938).

[33] E.U. Condon and H. Odishaw, eds., *Handbook of Physics*, McGraw Hill Book Company, New York (1967).

[34] R.S. Shankland, *Atomic and Nuclear Physics*, Macmillan, New York (1960).

[35] N. Bohr and J.A. Wheeler, *Phys. Rev.* **56** 426 (1939).

[36] R.W. Grimes and C.R.A. Catlow, *Philos. T. Roy. Soc. Lond. A* **335** 609 (1991).

[37] H. Kleykamp, *J. Nucl. Mater.* **131** 221 (1985).

[38] P. Debye and E. Hückel, *Z. Phys.* **24** 185 (1923).

[39] P. Debye and E. Hückel, *Z. Phys.* **25** 97 (1924).

[40] N. Hainovsky and J. Maier, *Phys. Rev. B* **55** 15789 (1995).

[41] F. Zimmer, P. Ballone, J. Maier and M. Parrinello, *Ber. Bunsenges. Phys. Chem.* **101** 1333 (1997).

[42] J.H. Harding, in *Computer Modelling in Inorganic Crystallography*. Academic Press Ltd. (1997).

[43] P.W. Tasker, *J. Phys. C.* **12** 4977 (1979).

[44] M. Abramowski, *Atomistic Simulations of the Uranium/Oxygen System*, Ph.D. thesis, Imperial College (2001).

[45] M. Abramowski, R.W. Grimes and S. Owens, *J. Nucl. Mater.* **275** 12 (1999).

[46] M. Abramowski, S.E. Redfern, R.W. Grimes and S. Owens, *Surf. Sci.* **490** 415 (2001).

[47] W.C. Mackrodt, R.J. Davey, S.N. Black and R. Doherty, *J. Cryst. Growth* **80** 441 (1987).

[48] S.C. Parker, P.J. Lawrence, C.M. Freeman, S.M. Levine and J.M. Newsam, *Catalysis Lett.* **15** 123 (1992).

[49] F. Bertaut, *Compt. Redu.* **246** 3447 (1958).

[50] A.E. Fick, *Pogg. Ann.* **94** 59 (1855).

[51] J.S. Kirklady and D.J. Young, *Diffusion in the Condensed State*, The Institute of Metals, London (1987).

[52] P. Shewmon, *Diffusion in Solids*, The Minerals, Metals and Materials Society, Warrendale, PA (1989).

[53] J. Crank, *The Mathematics of Diffusion*, Oxford University Press, Oxford (1975).

[54] R. Brown, *Philos. Mag.* **4** 161 (1828).

[55] M. von Smoluchowski, *Ann. Physik (Leipzig)* **25** 205 (1908).

[56] A. Einstein, *Ann. Physik (Leipzig)* **17** 549 (1905).

[57] A. Einstein, *Ann. Physik (Leipzig)* **19** 371 (1906).

[58] A. Einstein, *Zeit. Elektrochem.* **14** 235 (1908).

[59] J. Perrin, *J. de Chem. Physique* **8** 57 (1909).

[60] J. Perrin, *Les Atoms*, Van Nostrand, New York (1923).

[61] A. Einstein, *Investigations on the Theory of Brownian Movement*, Dover Publications, Inc. (1956).

[62] J.W. Gibbs, *The Collected Works of J. Willard Gibbs*, Longmans, Green and Co., New York (1928).

[63] S.M. Mukhopadhyay, A.P Jardine, J.M. Blakely and S. Baik, *J. Am. Ceram. Soc.* **71** 358 (1988).

[64] G.E. Moore, *Electronics* **38** (1965).

[65] A.T. Brunger and L.M. Rice, in J.H. Kalivas, ed., *Adaptation of Simulated Annealing to Chemical Optimisations Problems*. Elsevier (1995).

[66] I.M. Boswara and A.B. Lidiard, *Philos. Mag.* **16** 805 (1967).

[67] I.M. Boswara, *Philos. Mag.* **16** 827 (1967).

[68] C.R.A. Catlow, B.E.F. Fender and D.G. Muxworthy, *J. Phys. Colloque* **C7** 67 (1977).

[69] C.R.A. Catlow and D.G. Muxworthy, *Philos. Mag. B* **37** 63 (1978).

[70] C.R.A. Catlow, *Proc. Roy. Soc. London A* **353** 533 (1977).

[71] R.A. Jackson, A.D. Murray and C.R.A. Catlow, *Physica B+C* **131B** 136 (1985).

[72] R.A. Jackson and C.R.A. Catlow, *J. Nucl. Mater.* **127** 161 (1985).

[73] P.W. Tasker, "R.9130," Tech. rep., AERE Harwell (1978).

[74] D.M. Duffy and P.W. Tasker, "R.11059," Tech. rep., AERE Harwell (1983).

[75] P.W. Tasker and D.M. Duffy, *Surf. Sci.* **137** 91 (1984).

[76] E.A. Colburn, W.C. Mackrodt and P.W. Tasker, *J. Mater. Sci.* **18** 1917 (1983).

[77] D.H. Gay and A.L. Rohl, *J. Chem. Faraday Trans.* **91** 925 (1995).

[78] E. Madelung, *Phys. Zeit.* **11** 898 (1910).

[79] M. Born, *Atomtheorie des Festen Zustandes*, Teubner, Leipzig (1923).

[80] M. Born, *Handbuch der Physik*, Springer, Berlin (1933).

[81] M.P. Allen and D.J. Tildesley, *Computer Simulation of Liquids*, Clarendon Press, Oxford (1987).

[82] P.P. Ewald, *Ann. Phys. (Leipzig)* **64** 253 (1921).

[83] C. Kittel, *Introduction to Solid State Physics*, John Wiley & Sons, Inc., New York (1954).

[84] C.R.A Catlow and M.J. Norgett, "AERE - M2936," Tech. rep., Harwell Laboratory (1976).

[85] W. Pauli, *Z. Phys.* **31** 765 (1925).

[86] W. Pauli, *General Principles of Quantum Mechanics*, Springer-Verlag, Berlin (1980).

[87] P. Debye, *Phys. Zeit.* **21** 178 (1920).

[88] F. London, *Z. Phys.* **63** 245 (1930).

[89] F. London, *Z. phys. Chem. (B)* **11** 222 (1930).

[90] R. Eisenschitz and F. London, *Z. Phys.* **60** 491 (1930).

[91] H. Margenau, *Phys. Rev.* **38** 747 (1931).

[92] L. Pauling and E.B. Wilson, *Introduction of Quantum Mechanics, with Applications to Chemistry*, McGraw Hill, New York (1935).

[93] P.W. Fowler, P.J. Knowles and N.C. Pyper, *Mol. Phys.* **56** 83 (1985).

[94] M. Born and A. Landé, *Verhandlungen der Deutschen Phys. Gesellschaft* **21/24** 210 (1918).

[95] M. Born and J.E. Mayer, *Z. Phys.* **75** 1 (1932).

[96] J.E. Mayer, *J. Chem. Phys.* **1** 270 (1933).

[97] J.E. Lennard-Jones, *Proc. Roy. Soc.* **106** 441,463,709 (1924).

[98] J.E. Lennard-Jones, *Proc. Roy. Soc.* **109** 476 (1925).

[99] J.E. Lennard-Jones and A.E. Ingham, *Proc. Roy. Soc. A* **107** 636 (1925).

[100] R.A. Buckingham, *Proc. Roy. Soc. A* **168** 264 (1938).

[101] J.C. Slater and J.G. Kirkwood, *Phys. Rev.* **37** 682 (1931).

[102] N.W. Grimes and R.W. Grimes, *J. Phys.: Condensed Matter* **10** 3029 (1998).

[103] J.D. Gale, *Philos. Mag. B* **73** 3 (1996).

[104] J.H. Harding and N.C. Pyper, *Philos. Mag. Lett.* **71** 113 (1995).

[105] L. Minervini, *Atomistic Simulation of Defective Oxides*, Ph.D. thesis, Imperial College (2000).

[106] W.C. Mackrodt and R.F. Stewart, *J. Phys. C* **12** 5015 (1979).

[107] J.D. Gale, C.R.A. Catlow and W.C. Mackrodt, *Modelling Simul. Mater. Sci Eng.* **1** 73 (1992).

[108] R.W. Grimes, C.R.A. Catlow and A.M. Stoneham, *J. Phys.: Condensed Matter* **1** 7367 (1989).

[109] B.G. Dick and A.W. Overhauser, *Phys. Rev.* **112** 90 (1958).

[110] C.R.A. Catlow, R. James, W.C. Mackrodt and R.F. Stewart, *Phys. Rev. B* **25** 1006 (1982).

[111] C.R.A. Catlow, M. Dixon and W.C. Mackrodt, in *Computer Simulation of Solids*. Springer-Verlag (1982).

[112] F. Seitz, *The Modern Theory of Solids*, McGraw Hill, New York (1940).

[113] A.E.H. Love, *A Treatise on the Mathematical Theory of Elasticity*, Dover Publications, New York (1944).

[114] U. Schroder, *Solid State Commun.* **4** 347 (1966).

[115] M.J. Sangster, *J. Phys. Chem. Solids* **35** 195 (1974).

[116] G.W. Watson, P. Tschaufeser, A. Wall, R.A. Jackson and S.C. Parker, in *Computer Modelling in Inorganic Crystallography*. Academic Press Ltd. (1997).

[117] W.H. Press, S.A. Teukolsky, W.T. Vetterling and B.P. Flannery, *Numerical Recipes in Fortran*, Cambridge University Press, Cambridge (1992).

[118] C.R.A Catlow and M.J. Norgett, "AERE - M2763," Tech. rep., Harwell Laboratory (1978).

[119] C.R.A. Catlow and W.C. Mackrodt, in *Computer Simulation of Solids*. Springer-Verlag (1982).

[120] N.F. Mott and M.J. Littleton, *Trans. Faraday Soc.* **34** 485 (1938).

[121] A.B. Lidiard and M.J. Norgett, in *Computational Solid State Physics*. Plenum Press (1972).

[122] M.J. Norgett, "AERE - R.7015," Tech. rep., Harwell Laboratory (1972).

[123] D.E. Parry, *Surf. Sci.* **49** 433 (1975).

[124] D.E. Parry, *Surf. Sci.* **54** 195 (1976).

[125] D.M. Heyes, M. Barber and J.H.R. Clarke, *J. Chem. Soc., Faraday Trans. II* **73** 1485 (1977).

[126] M.B Taylor, C.E. Sims, G.D. Barrera, N.L. Allen and W.C. Mackrodt, *Phys. Rev. B* **59** 6742 (1999).

[127] M. Leslie, "DL/SCI/TM31T," Tech. rep., SERC Daresbury Laboratory (1982).

[128] A.L. Shluger, A.L. Rohl, D.H. Gay and R.T. Williams, *J. Phys.: Condens. Matter* **6** 1825 (1994).

[129] M.A. McCoy, R.W. Grimes and W.E. Lee, *Philos. Mag. A* **75** 833 (1997).

[130] R.W. Grimes, D.J. Binks and A.B. Lidiard, *Philos. Mag. A* **72** 651 (1995).

[131] R.W. Grimes, *J. Am. Ceram. Soc.* **77** 378 (1994).

[132] S.P. Chen, M. Yan, R.W. Grimes and S. Vyas, *Ceram. Trans.* **69** 129 (1997).

[133] M.A. McCoy, R.W. Grimes and W.E. Lee, *Philos. Mag. A* **76** 1187 (1997).

[134] R.W. Grimes, G. Busker, M.A. McCoy, A. Chroneos, J.A. Kilner and S.P. Chen, *Ber. Bunsen. Phys. Chem.* **101** 1204 (1997).

[135] C.R. Stanek, L. Minervini and R.W. Grimes, *J. Am. Ceram. Soc.* **85** 2792 (2002).

[136] M.O. Zacate, R.W. Grimes and K. Scrivner, *J. Mater. Sci.* **35** 3727 (2000).

[137] S. Vyas, R.W. Grimes, D.H. Gay and A.L. Rohl, *J. Chem. Soc., Faraday Trans.* **94** 427 (1998).

[138] G. Busker, A. Chroneos and R.W. Grimes, *J. Am. Ceram. Soc.* **82** 1553 (1999).

[139] R.W. Grimes and G. Busker, *Nucl. Energy* **35** 403 (1996).

[140] S. Imoto, *J. Nucl. Mater.* **140** 19 (1986).

[141] J.A. Turnbull and R.M. Cornell, *J. Nucl. Mater.* **41** 156 (1971).

[142] Hj. Matzke and J.A. Davies, *J. Appl. Phys.* **38** 805 (1967).

[143] Hj. Matzke, *Radiat. Eff.* **53** 219 (1980).

[144] J.A. Turnbull, C.A. Friskney, J.R. Findlay, F.A. Johnson and A.J. Walter, *J. Nucl. Mater.* **107** 168 (1982).

[145] R.G.J. Ball, W.G. Burns, J. Henshaw, M.A. Mignanelli and P.E. Potter, *J. Nucl. Mater.* **167** 191 (1989).

[146] T.T. Yang and C.H. Tsai, *J. Nucl. Mater.* **166** 252 (1989).

[147] C. Sari, C.T. Walker and G. Schumacher, *J. Nucl. Mater.* **79** 255 (1979).

[148] A. Maeda, T. Ohmichi, S. Fukushima and M. Handa, *J. Nucl. Sci. Tech.* **21** 800 (1984).

[149] T.L. Markin, R.S. Street and E.C. Crouch, *J. Inorg. Nucl. Chem* **32** 59 (1970).

[150] C.R.A. Catlow, *Proc. Roy. Soc. A* **353** 533 (1977).

[151] R.A. Jackson, C.R.A. Catlow and A.D. Murray, *J. Chem. Soc., Faraday Trans. II* **83** 1171 (1987).

[152] R.A. Jackson, A.D. Murray, J.H. Harding and C.R.A. Catlow, *Philos. Mag. A* **53** 27 (1986).

[153] R.W. Grimes, C.R.A. Catlow and A.M. Stoneham, *J. Am. Ceram. Soc.* **72** 1856 (1989).

[154] R.G.J. Ball and R.W. Grimes, *J. Chem. Soc., Faraday Trans. II* **86** 1257 (1990).

[155] C.R.A. Catlow, *Proc. Roy. Soc. London A* **364** 473 (1978).

[156] R.A. Jackson and C.R.A. Catlow, *J. Nucl. Mater.* **127** 161 (1985).

[157] R.A. Jackson and C.R.A. Catlow, *J. Nucl. Mater.* **127** 167 (1985).

[158] J.H. Harding, *J. Chem. Soc., Faraday Trans. II* **83** 1177 (1987).

[159] Hj. Matzke and H. Blank, *J. Nucl. Mater.* **166** 120 (1989).

[160] T. Petit, G. Jomard, C. Lemaignan, B. Bigot and A. Pasturel, *J. Nucl. Mater.* **275** 119 (1999).

[161] T. Petit, C. Lemaignan, F. Jollet, B. Bigot and A. Pasturel, *Philos. Mag. B* **77** 779 (1998).

[162] J.P. Crocombette, *J. Nucl. Mater.* **305** 29 (2002).

[163] C.R. Stanek and R.W. Grimes, *J. Nucl. Mater.* **282** 265 (2000).

[164] Hj. Matzke, *J. Nucl. Mater.* **30** 110 (1969).

[165] T. Petit, B. Morel, C. Lemaignan, A. Pasturel and B. Bigot, *Philos. Mag. B* **73** 893 (1996).

[166] F. Jollet, T. Petit, S. Gota, N. Thromat, M. Gautier-Soyer and A. Pasturel, *J. Phys.: Condensed Mat.* **9** 9393 (1997).

[167] R.C. McCune and P. Wynblatt, *J. Am. Ceram. Soc.* **66** 111 (1983).

[168] A. Roshko and W.D. Kingery, *J. Am. Ceram. Soc.* **68** C331 (1985).

[169] S. Baik and C.L. White, *J. Am. Ceram. Soc.* **70** 682 (1987).

[170] S. Baik, D.E. Fowler, J.M. Blakely and R. Raj, *J. Am. Ceram. Soc.* **68** 281 (1985).

[171] H.L. Marcus and M.E. Fine, *J. Am. Ceram. Soc.* **55** 568 (1973).

[172] R.I. Taylor, J.P. Coad and R.J. Brook, *J. Am. Ceram. Soc.* **57** 539 (1974).

[173] W.C. Johnson and D.F. Stein, *J. Am. Ceram. Soc.* **58** 485 (1975).

[174] P.E.C. Franken and A.P. Gehring, *J. Mater. Sci.* **16** 384 (1981).

[175] W.C. Johnson and R.L. Coble, *J. Am. Ceram. Soc.* **61** 110 (1978).

[176] S.M. Foiles, *Phys. Rev. B* **32** 7685 (1985).

[177] S.M. Foiles, *Phys. Rev. B* **40** 11502 (1989).

[178] J.H. Harding and D.J. Harris, *Phys. Rev. B* **63** 094102 (2001).

[179] D.M. Duffy, J.P. Hoare and P.W. Tasker, *J. Phys. C: Solid State Phys.* **17** L195 (1984).

[180] D.M. Duffy and P.W. Tasker, *Philos. Mag. A* **50** 143 (1984).

[181] P.W. Tasker, E.A. Colburn and W.C. Mackrodt, *J. Am. Ceram. Soc.* **68** 74 (1985).

[182] P.W. Tasker and W.C. Mackrodt, *J. Am. Ceram. Soc.* **72** 1576 (1989).

[183] M. Cotter, S. Campbell, L.L. Cao, R.G. Egdell and W.C. Mackrodt, *Surf. Sci.* **208** 267 (1989).

[184] M.J. Davies, P.R. Kenway, P.J. Lawrence, S.C. Parker, W.C. Mackrodt and P.W. Tasker, *J. Chem. Soc., Faraday Trans. II* **85** 555 (1989).

[185] P.R. Kenway, P.M. Oliver, S.C. Parker, D.C. Sayle, T.X.T. Sayle and J.O. Titiloye, *Mol. Simulat.* **9** 83 (1992).

[186] T.X.T. Sayle, S.C. Parker and C.R.A. Catlow, *J Phys. Chem.* **98** 13625 (1994).

[187] B. Slater, C.R.A. Catlow, D.H. Gay, D.E. Williams and V. Dusastre, *J. Phys. Chem. B* **103** 10644 (1999).

[188] P.A. Mulheran and J.H. Harding, *Modelling Mater. Sci. Eng.* **1** 39 (1992).

[189] C.C. Battaile, R. Najafabadi and D.J. Srolovitz, *J. Am. Ceram. Soc.* **78** 3915 (1995).

[190] R. LeSar, R. Najafabadi and D.J. Srolovitz, *Phys. Rev. Lett.* **63** 624 (1989).

[191] R. Najafabadi, H.Y. Wang, D.J. Srolovitz and R. LeSar, *Acta Metall.* **39** 3071 (1991).

[192] S. Vyas, R.W. Grimes, V. Bulatov and M. Abramowski, *Mol. Simulat.* **26** 307 (2001).

[193] C. Muggelberg, M.R. Castell, G.A.D. Briggs and D.T. Goddard, *App. Surf. Sci.* **142** 124 (1999).

[194] M.R. Castell, C. Muggelberg, G.A.D. Briggs and D.T. Goddard, *J. Vac. Sci. Technol. B* **14** 966 (1996).

[195] C. Muggelberg, M.R. Castell, G.A.D. Briggs and D.T. Goddard, *Surf. Rev. Lett.* **5** 315 (1998).

[196] C. Muggelberg, M.R. Castell, G.A.D. Briggs and D.T. Goddard, *Surf. Sci.* **402-404** 673 (1998).

[197] B.D. Campbell and W.P. Ellis, *J. Chem. Phys.* **52** 409 (1970).

[198] I. Sato, H. Furuya, T. Arima, K. Idemitsu and K. Yamamoto, *J. Nucl. Sci. Tech.* **36** 775 (1999).

[199] D.P. Cann, C.A. Randall and T.R. Shrout, *Solid State Commun.* **7** 529 (1996).

[200] M. Valant and P.K. Davies, *J. Am. Ceram. Soc.* **83** 147 (2000).

[201] J.B. Goodenough and R.N. Castellano, *J. Solid State Chem.* **44** 108 (1982).

[202] S.J. Korf, H.J.A. Koopmans, B.C. Lippens, A.J. Burggraaf and P.J. Gellings, *J. Chem. Soc., Faraday Trans.* **83** 1485 (1987).

[203] H.L. Tuller, *Solid State Ionics* **52** 135 (1992).

[204] S. Kramer, M. Spears and H.L. Tuller, *Solid State Ionics* **72** 59 (1994).

[205] C. Heremans, B.J. Wuensch, J.K. Stalick and E. Prince, *J. Solid State Chem.* **117** 108 (1995).

[206] M.J. Maloney, "Thermal Barrier Coating Systems and Materials," U.S. Patent No. US 6,117,560 (2000).

[207] M.J. Maloney, "Thermal Barrier Coating Systems and Materials," U.S. Patent No. US 6,177,200 B1 (2001).

[208] W.J. Weber, R.C. Ewing, C.R.A. Catlow, T. Diaz de la Rubia, L.W. Hobbs, C. Kinoshita, Hj. Matzke, A.T. Motta, M. Nastasi, E.K.H. Salje, E.R. Vance and S.J. Zinkle, *J. Mater. Res.* **13** 1434 (1998).

[209] R.C. Ewing, W. Lutze and W.J. Weber, *J. Mater. Res.* **10** 243 (1995).

[210] R.C. Ewing, W.J. Weber and F.W. Clinard Jr., *Prog. Nucl. Energy* **29** 63 (1995).

[211] K.E. Sickafus, L. Minervini, R.W. Grimes, J.A. Valdez, M. Ishimaru, F. Li, K.J. McClellan and T. Hartmann, *Science* **289** 748 (2000).

[212] E.R. Andrievskaya, L.M. Lopato and V.P. Smirnov, *J. Am. Ceram. Soc.* **79** 714 (1996).

[213] E.R. Andrievskaya and L.M. Lopato, *J. Am. Ceram. Soc.* **84** 2415 (2001).

[214] A.V. Zagorodnyuk, L.V. Sadkovskaya, G.V. Shamrai, I.P. Kovalevskaya, R.L. Magunov and G.A. Teterin, *Russ. J. Inorg. Chem.* **31** 1377 (1986).

[215] G.V. Shamrai, R.L. Magunov, I.V. Stasenko and A.P. Zhirnova, *Inorg. Mater.* **25** 233 (1989).

[216] G.V. Shamrai, R.L. Magunov and I.P. Kovalevskaya, *Inorg. Mater.* **22** 1695 (1986).

[217] G.A. Teterin, V.F. Zinchenko, A.V. Zagorodnyuk and I.M. Minaev, *Sov. Progr. Chem.* **54** 31 (1988).

[218] N.F. Fedorov, O.V. Mel'nikova, V.A. Saltykova and M.V. Chistyakova, *Russ. J. Inorg. Chem.* **24** 649 (1979).

[219] F. Queyroux, *C.R.H. Acad. Sci.* **259** 1527 (1964).

[220] L.G. Shcherbakova, V.B. Glushkova, L.P. Lyashenko, A.P. Zaitseva and L.V. Sazonova, *Dokl. Chem. (USSR)* **236** 619 (1977).

[221] A.V. Kolesnikov, G.E. Sukhanova, A.P. Zaitseva and L.G. Scherbakova, *Inorg. Mater.* **23** 222 (1987).

[222] N. Mizutani, Y. Tajima and M. Kato, *J. Am. Ceram. Soc.* **59** 168 (1976).

[223] S.S. Kiparisov, R.A. Belyaev, A.I. Belyakov, V.V. Kondarenko, V.P. Vyskubov, V.G. Kozlov, S.A. Kuznetsov and L.P. Melikhova, *Inorg. Mater.* **12** 1393 (1976).

[224] M.P. y Jorba, *Ann. Chim. (Paris)* **7** 479 (1962).

[225] A. Rouanet, *Rev. Int. Hautes Temp. Refract.* **8** 161 (1971).

[226] F.H. Brown Jr. and P. Duwez, *J. Am. Ceram. Soc.* **38** 95 (1955).

[227] R.S. Roth, *J. Res. Natl. Bur. Std.* **56** 24 (1956).

[228] H. Yokokawa, N. Sakai, T. Horita, K. Yamaji, T. Otake, H. Yugami, T. Kawada and J. Mizusaki, *Journal of Phase Equilibria* **22** 331 (2001).

[229] P.S. Duwez and F.H. Brown Jr., *J. Electrochem. Soc.* **98** 360 (1951).

[230] K.K. Srivastava, R.N. Patil, C.B. Choudhary, K.V.G.K. Gokhale and E.C. Subbarao, *Trans. J. Br. Ceram. Soc.* **73** 85 (1974).

[231] H.G. Scott, *J. Mater. Sci.* **10** 1527 (1975).

[232] H.G. Scott, *J. Aust. Ceram. Soc.* **17** 16 (1982).

[233] V.S. Stubican and J.R. Hellmann, *Adv. Ceram.* **3** 25 (1981).

[234] V.S. Stubican, R.C. Hink and S.P. Ray, *J. Am. Ceram. Soc.* **61** 17 (1978).

[235] A.V. Shevchenko, L.M. Lopato and I.E. Kir'yakova, *Inorg. Mater.* **20** 1731 (1984).

[236] A.V. Shevchenko and L.M. Lopato, *Inorg. Mater.* **18** 1583 (1982).

[237] A.V. Shevchenko, L.M. Lopato and L.V. Nazarenko, *Inorg. Mater.* **20** 1615 (1984).

[238] A.V. Shevchenko, L.M. Lopato and Z.A. Zaitseva, *Inorg. Mater.* **20** 1316 (1984).

[239] P.J. Wilde and C.R.A. Catlow, *Solid State Ionics* **112** 173 (1998).

[240] P.J. Wilde and C.R.A. Catlow, *Solid State Ionics* **112** 185 (1998).

[241] R.E. Williford and W.J. Weber, *J. Am. Ceram. Soc.* **82** 3266 (1999).

[242] R.E. Williford, W.J. Weber, R. Devanathan and J.D. Gale, *J. Electroceram.* **3** 409 (1999).

[243] L. Minervini, R.W. Grimes and K.E. Sickafus, *J. Am. Ceram. Soc.* **83** 1873 (2000).

[244] M. Pirzada, R.W. Grimes, L. Minervini, J.F. Maguire and K.E. Sickafus, *Solid State Ionics* **140** 201 (2001).

[245] L. Minervini, R.W. Grimes, Y. Tabira, R.L. Withers and K.E. Sickafus, *Philos. Mag. A* **82** 123 (2002).

[246] "OriginPro v6.1," Microcal Software, Inc., Northampton, MA (1999).

[247] J.C. Davis, *Statistics and Data Analysis in Geology*, John Wiley & Sons, Inc., New York (1986).

[248] F. Brisse and O. Knop, *Can. J. Chem.* **46** 859 (1968).

[249] B.J. Kennedy, *Physica B* **241** 303 (1998).

[250] H.L. Tuller, *J. Phys. Chem. Solids* **55** 1393 (1994).

[251] B.J. Kennedy, B.A. Hunter and C.J. Howard, *J. Solid State Chem.* **130** 58 (1997).

[252] E.R. Andrievskaya, L.M. Lopato, A.V. Shevchenko and V.P. Smirnov, *Inorg. Mater.* **33** 835 (1997).

[253] P. Duran, C. Pascual, J. Coutures and S.R. Skaggs, *J. Am. Ceram. Soc.* **66** 101 (1983).

[254] C.R.A. Catlow and W.C. Mackrodt, eds., *Computer Simulation of Solids*, Springer-Verlag, Berlin, Germany (1982).

[255] P.K. Moon and H.L. Tuller, *Solid State Ionics* **28** 470 (1988).

[256] A.W. Sleight, *Inorg. Chem.* **8** 1807 (1969).

[257] S. Arrhenius, *Z. phys. Chem.* **10** 51 (1892).

[258] K.B. Helean, A. Navrotsky, E.R. Vance, M.L. Carter, B. Ebbinghaus, O. Krikorian, J. Lian, L.M. Wang and J.G. Catalano, *J. Nucl. Mater.* **303** 226 (2002).

[259] M. Abramowski, R.W. Grimes and S. Owens, *J. Nucl. Mater.* **275** 12 (1999).

[260] J.J. Swabb, *J. Mat. Sci.* **26** 6706 (1991).

[261] T. Sato, S. Ohtaki, T. Endo and M. Shimeda, *High Tech. Ceramics*, 281, Elsevier, Amsterdam (1987).

[262] K.L. Grant and R.D. Rawlings, *J. Mat. Sci. Lett.* **18** 739 (1999).

[263] K.L. Grant, R.D. Rawlings and R. Sweeney, *J. Mat. Sci.: Mat. Med.* **12** 557 (2001).

[264] J. Chevalier, B. Cales and J.M. Drouin, *J. Am. Ceram. Soc.* **82** 2150 (1999).

[265] J.F. Li and R. Watanabe, *J. Am. Ceram. Soc.* **66** 196 (1983).

[266] S. Stemmer, J. Vleugels and O. van der Biest, *J. Europ. Ceram. Soc.* **18** 1565 (1998).

[267] H. Ogawa, A. Yashua, N. Shibata, Y. Ikuhara and T. Sakuma, *Philos. Mag. Lett.* **77** 199 (1998).

[268] A. Gulino, R.G. Egdell, G.A. Baratta, G. Compagnini and I. Fragala, *J. Mat. Chem.* **7** 1023 (1997).

[269] A. Gulino, R.G. Egdell and I. Fragala, *J. Am. Ceram. Soc.* **81** 757 (1998).

[270] S.E. Redfern, R.W. Grimes and R.D. Rawlings, *J. Mater. Chem* **11** 449 (2001).

[271] P.K. Schelling, S.R. Phillpot and D. Wolf, *J. Am. Ceram. Soc.* **84** 1609 (2001).

[272] M.O. Zacate, L. Minervini, D.J. Bradfield, R.W. Grimes and K.E. Sickafus, *Solid State Ionics* **128** 243 (2000).

[273] C.R. Stanek, R.W. Grimes and M. Bradford, *Mat. Res. Symp. Proc.* **654** AA3.32.1 (2001).

[274] P.W. Tasker, *Philos. Mag. A* **39** 119 (1979).

[275] W.C. Mackrodt and P.W. Tasker, *Mat. Res. Symp. Proc.* **60** 291 (1986).

[276] P.R. Kenway, S.C. Parker and W.C. Mackrodt, *Mol. Simulat.* **4** 175 (1989).